INTERNATIONAL DOCTORAL
SCHOOL OF THE USC

Miguel Augusto
Palhinha Castillo

PhD Thesis

Natural photosynthetic nanostructures as a blueprint for bio-inspired organic photonics

Santiago de Compostela, 2023

Doctoral Programme in Laser, Photonics and Vision

USC
UNIVERSIDADE
DE SANTIAGO
DE COMPOSTELA



DOCTORAL THESIS

Natural photosynthetic nanostructures as a blueprint for bio-inspired organic photonics

Miguel Augusto Palhinha Castillo

INTERNATIONAL PHD SCHOOL OF THE UNIVERSITY OF SANTIAGO DE COMPOSTELA

DOCTORAL PROGRAMME IN LASER, PHOTONICS, AND VISION

Thesis Director:
Martín Lopez-García

Thesis Tutor:

Vicente Moreno De Las Cuevas

SANTIAGO DE COMPOSTELA

2023

USC
UNIVERSIDADE
DE SANTIAGO
DE COMPOSTELA

Author Declaration

Author's Name: Miguel Augusto Palhinha Castillo
Thesis Title: Natural photosynthetic nanostructures as a blueprint for bio-inspired organic photonics

I present my thesis following the adequate procedure in the Regulations and I declare that:

- The thesis shows results from my own work.
- When it is the case, the thesis makes reference to the collaborations that happened throughout this work.
- I confirm that the thesis does not have any kind of plagiarism from other authors or from other pieces of work presented for the completion of other titles.
- The thesis is the final version presented in the defence and the printed version coincides with the electronic version.

And I assure that I will present the Compromise Document of Supervision in case the original is not deposited in the school.

Braga, March 15, 2023,

Miguel Augusto Palhinha Castillo
(Thesis Author)

USC
UNIVERSIDADE
DE SANTIAGO
DE COMPOSTELA

Authorisation from the Thesis Director

Natural photosynthetic nanostructures as a blueprint for bio-inspired organic photonics

I, Dr. Martin Lopez-Garcia, group leader at the International Iberian Nanotechnology Laboratory,

DECLARE:

That the thesis presented here, corresponds to the work done by Miguel Augusto Palhinha Castillo, under my supervision, and that I authorise its presentation, considering that it fulfils all the requirements in the Regulation for Doctoral Studies of the USC and that, as director of this thesis, it doesn't incur any causes of abstention established in the Law 40/2015.

According to the aforementioned Regulation for Doctoral Studies, I declare as well that the doctoral thesis presented here is suitable to be defended as a compendium of papers, where the participation of the doctoral student was crucial for the development of these publications and that they fit well within the Research Plan.

Braga, March 15, 2023,

Martin Lopez-Garcia
(Thesis Director)

USC
UNIVERSIDADE
DE SANTIAGO
DE COMPOSTELA

Authorisation from the Thesis Tutor

Natural photosynthetic nanostructures as a blueprint for bio-inspired organic photonics

I, Dr. Vicente Moreno de las Cuevas, professor at the University of Santiago de Compostela,

DECLARE:

That the thesis presented here, corresponds to the work done by Miguel Augusto Palhinha Castillo, under my supervision, and that I authorise its presentation, considering that it fulfils all the requirements in the Regulation for Doctoral Studies of the USC and that, as tutor of this thesis, it doesn't incur any causes of abstention established in the Law 40/2015.

According to the aforementioned Regulation for Doctoral Studies, I declare as well that the doctoral thesis presented here is suitable to be defended as a compendium of papers, where the participation of the doctoral student was crucial for the development of these publications and that they fit well within the Research Plan.

Santiago de Compostela, March 15, 2023,

Vicente Moreno de las Cuevas
(Thesis Tutor)

USC
UNIVERSIDADE
DE SANTIAGO
DE COMPOSTELA

Resumo en Galego

A luz solar foi utilizada como fonte de enerxía polos seres vivos durante miles de millóns de anos. Nas plantas superiores e nas algas, os cloroplastos captan a luz e transfórmana en enerxía química, no proceso coñecido como fotosíntese. Debido á importancia desta actividade para a vida na Terra, as propiedades químicas e morfolóxicas dos cloroplastos teñen sido moi estudadas. No que respecta a este traballo, podemos separar a estrutura dos cloroplastos en dúas partes: a grana, que presenta absorción de luz, e o medio acuoso circundante, con absorción practicamente nula. a grana està composto por membranas coñecidas como tilacoides, onde se atopan os principais complexos fotosintéticos e onde ocorren as reaccións dependentes da luz; o lume tilacoide (no grana), onde se producen reaccións químicas para axudar aos principais procesos fotosintéticos, como a transferencia de electróns e a produción de osíxeno; e o estroma (rodeando a grana), onde ocorren as reaccións de fixación de carbono independentes da luz. As reaccións fotosintéticas dependentes da luz ocorren en complexos especializados dentro das membranas tilacoides coñecidos como centros de reacción. É importante destacar que estes sistemas non son responsables de cantidades significativas de absorción de luz. Pola contra, a maior parte da absorción da luz ocorre nunha serie de combinacions de proteínas e pigmentos, coñecidas como antenas, que tamén se atopa nas membranas dos tilacoides. Unha vez excitados, a enerxía do excitón transfírese entre eles ata que finalmente chegan ao centro de reacción. É importante destacar que a superposición entre os estados de enerxía do doador e o aceptor crese que é responsable da eficiencia de case o 100% do proceso de transferencia de enerxia. Para evitar o dano oxidativo aos complexos fotosintéticos polo exceso de enerxía, os cloroplastos desenvolveron varios mecanismos para protexerse contra o exceso de absorción de luz, que inclúen cambios de morfoloxía para controlar a difusión de proteínas e a transferencia de electróns.

Curiosamente, o comportamento como onda da luz permite a interacción con sistemas con características estruturais en escalas de ordes de magnitude similares, é dicir, a nanoescala. As ecuacións de Maxwell rexen estas interaccións. Os sistemas cun índice de refracción periódico a esta escala poden crear interferencias construtivas e destrutivas pola dispersión interna de ondas luminosas. Estas estruturas coñécense como cristais fotónicos e utilízanse para manipular o fluxo de luz. Para os efectos desteo traballo, centraréime nun sistema que consiste nunha multicapa periódica composta só por dous materiais con índices de refracción distintos, coñecido como Distributed Bragg Reflector (DBR) ou espello de Bragg. É importante destacar que, cando a lonxitude de onda é preto do dobre que o período óptico, a luz reflíctese e non pode propagarse polo sistema; esta rexión coñécese como banda espectral de parada. Debido á dependencia da estrutura do sistema, a lonxitude de onda desta banda espectral dependerá do ángulo de incidencia da luz. Dita dependencia angular pode dar lugar o coñecido como cor estructural. Ademais, para as lonxitudes de onda no bordo vermello desta banda, créase unha onda estacionaria onde a luz se concentra no material co menor índice de refracción e, pola contra, nas lonxitudes de onda do bordo azul, créase unha onda estacionaria pero a luz concéntrase no material co maior refracción. Estas ondas estacionarias reduciron fortemente a velocidade do grupo, aumentando as interaccións luz-materia. Isto coñécese como efecto de luz lenta.

A pesar da precisión nanoscópica necesaria, as estruturas fotónicas foron desenvolvidas pola natureza nunha variedade de especies, desde insectos, animais, algas e froitas. Estas estructuras fotònicas cumpren diversas funcións biolóxicas como atraccion durante o aparea-

USC UNIVERSIDADE DE SANTIAGO

mento, o mimetismo e atraer outros animais. Curiosamente, recentemente observáronse estruturas fotosintéticas fotónicas, coñecidas como iridoplastos (cloroplastos iridiscentes) en certas *Begonias*, unha especie de plantas autoctonas de zonas tropicais. Os iridoplastos son semellantes a un cloroplasto estándar sendo distintivos da súa estrutura un apilamento de 8 tilacoides ordenadamente uns encima dos outros cun espazo estroma consistente entre eles. Esta morfoloxía é análoga a un DBR cun período de 168 nm e produce unha forte reflexión no azul, a lonxitudes de onda $\lambda \sim 450$ nm. Esta estrutura deixou perplexos aos investigadores xa que as plantas con estes orgánulos atópanse en condicións de dispoñibilidade restrinxida á luz. A forte reflectancia, polo tanto, parece agravar este problema.

Debido ao ambiente circundante, a atenuación da luz na superficie das follas destas *Begonias* depende grandemente das lonxitudes de onda. No azul ($\lambda < 500$ nm) o reconto de fotóns redúcese significativamente en comparación co verde ($500 < \lambda < 570$ nm), onde a luz é máis abundante. Por ese motivo, a banda de parada fotónica está simplemente reflectindo as lonxitudes de onda de luz menos dispoñibles. Ademais, os efectos de luz lenta neste sistema aseguran que, no bordo de alta lonxitude de onda da banda fotónica ($\lambda \sim 520$ nm) a luz interactúe con maior forza coa grana, onde se atopan os complexos fotosintéticos de absorción. Descubriuse que isto aumenta a absorción de luz ata un 20% nestas lonxitudes de onda de intensidade luminosa abundante. É importante destacar que esta mellora compárase cun sistema de referencia que presenta a mesma cantidade de material absorbente pero sen estrutura fotónica. Ademais, descubriuse que melloran a eficiencia cuántica (relación entre fotóns útiles e fotóns incidentes) entre un 5% e un 10%. Polo tanto, a vantaxe biolóxica dos iridoplastos parecía ser dobre: aumentar a absorción da luz mediante efectos de luz lenta e ter unha conversión máis eficiente. Este estudo foi publicado recentemente e foi pioneiro na conexión entre a fotónica e a fotosíntese. Curiosamente, observouse que os iridoplastos, a simple vista, cambiaban de forma reversible do azul en condicións de pouca luz ao verde en condicións de moita luz. Aínda que non hai investigacións en profundidade sobre isto, hipótetizouse que isto è causado pola expansión (contracción) da morfoloxía dos cloroplastos en condicións de moita (pouca) luz. Ao mesmo tempo, estaba sendo investigado outro cloroplasto fotónico coñecido como bizonoplasto. Estes bizonoplastos atopanse en condicións de luz similares ás dos iridoplastos. É unha estrutura máis grande que os iridoplastos composta por dúas zonas, unha estruturada (cun período de 194 nm similar ao iridoplasto) e outra non estruturada (similar a un cloroplasto estándar). As súas propiedades fotónicas permaneceron maioritariamente sen explorar.

O papel da fotónica nun dos procesos biolóxicos máis importantes para a vida na Terra, a fotosíntese, segue sendo pouco coñecido. Desde un punto de vista teórico, aínda queda por investigar de forma cuantitativa o seu impacto na mellora da absorción da luz, o papel da desorde e os cambios morfolóxicos dependentes da luz, entre moitos outros. Desde un punto de vista experimental, os cambios estruturais dependentes da luz e as propiedades de absorción das membranas tilacoides seguen sendo pouco comprendidas. Fundamentalmente, é necesario medir a absorción do sistema fotónico para observar directamente unha mellora. Nesta tese, comezamos defendendo a tese de que os cloroplastos fotónicos evolucionaron para mellorar a absorción da luz. En primeiro lugar, desenvolvemos os antecedentes teóricos dos cloroplastos fotónicos (tanto iridoplastos como bizonoplastos) para responder ás preguntas teóricas mencionadas.

USC UNIVERSIDADE DE SANTIAGO DE COMPOSTELA

Para desenvolver o marco teórico escribiuse un modelo computacional baseado no Método da Matriz de Transferencia (TMM), unha técnica utilizada para resolver as ecuacións de

Maxwell de estruturas multicapa 1D. Para usalo requírese só a información estrutural do sistema e as propiedades ópticas dos materiais constituíntes. Debido á súa eficiencia e sinxeleza, proporciona unha técnica extremadamente rápida para calcular as propiedades fotónicas esperadas a partir dun cristal fotónico 1D. A información estrutural dos iridoplastos e bizonoplastos axustados á escuridade obtivose da literatura. Non se explorou a información morfolóxica en condicións de alta luz, pero os cambios pódense extrapolar de estudos previos de cloroplastos estándar e outros iridoplastos. Polo tanto agrdamos que o período do iridoplasto se amplíe de 168 nm, con pouca luz, a 206 nm, con luz alta. Para os bizonoplastos, esperamos que esta expansión sexa de 164 nm a 226 nm.

Para iridoplastos, baixo unha alta expansión estrutural inducida pola luz, a reflectancia desprázase ao vermello de $\lambda \sim 450$ nm a $\lambda \sim 550$ nm (baixo incidencia normal e o valor absoluto vai de 12% a 4%). Conclusións similares tómanse en ángulos máis altos. É importante destacar que a absorción mellorada inducida pola luz lenta tamén se desplaza ao vermello e se atenúa. Para cuantificar o impacto da luz lenta, dividimos a luz total absorbida polo sistema fotónico e a referencia. a absorción total atópase integrando sobre a lonxitude de onda a multiplicación entre a absorción dependente da lonxitude de onda e a radiación luminosa dispoñible no seu medio natural.Obtemos que, en condicións de pouca luz, o sistema fotónico absorbe 4% máis de luz que unha referencia e, baixo de alta luz absorben, os iridoplastos o mesmo que a referencia, o que demostra unhas sorprendentes capacidades de sintonización de absorción de luz.

Para os bizonoplastos, a reflectancia desprázase ao vermello de $\lambda \sim 450$ nm a $\lambda \sim 540$ nm e a reflectancia absoluta cae de 26% a 22% en incidencia normal; obsérvanse cambios semellantes en ángulos máis altos. A absorción mellorada por efectos de luz lenta descubriuse que era menos significativa que nos iridoplastos, cunha mellora máxima de 6% a $\lambda = 520$ nm para condicións de pouca luz. En lonxitudes de onda globais, a absorción total de luz comparada cunha estrutura de referencia foi só 1% máis alta con pouca luz e 1% máis baixa con luz intensa, mostrando efectos insignificantes.

Para considerar un erro bioloxicamente realista, tomamos o erro das medicións estruturais experimentais e usámolo como a incerteza de cada capa individual do modelo, baseándose nunha distribución normal. Debido á natureza aleatoria deste proceso, é necesaria unha simulación de Monte Carlo para obter o resultado esperado. A repetición das simulacións anteriores con estes paràmetros mostrou unha pequena caída na reflectancia absoluta e unha diferenza insignificante na absorción total de luz mellorada para ambos os cloroplastos fotónicos. Isto demostra a resistencia dos cristais fotónicos á desorde.

Como parte final deste estudo teórico, analizamos as capacidades de sintonización de tres cloroplastos (dous fotónicos e outro non estruturado). Para iso, calculamos un factor de mellora da absorción, γ_{total}, onde comparamos a absorción dun cloroplasto baixo pouca luz co mesmo cloroplasto pero axustado para a luz intensa. Calculamos a mellora da absorción total para dous ambientes diferentes: a radiación luminosa dispoñible no medio natural dos cloroplastos fotónicos que conteñen plantas e a radiación dispoñible baixo a luz solar directa (é dicir, por riba do dosel). Respectivamente, atopamos: para os iridoplastos γ_{total} = 1,19 e 1,16; para os cloroplastos, γ_{total} = 1,15 e 1,14; e para os bizonoplastos γ_{total} = 1,10 e 1,04. Polo tanto, todos os tipos de cloroplastos presentan unha grande capacidades de sintonización.

Non obstante, resulta desconcertante que os bizonoplastos non parecen presentar ningunha vantaxe sobre os cloroplastos non estruturados. A razón disto é a existencia de numerosas granas por debaixo da zona estruturada. Isto significa que, independentemente de efectos

de luz lentos, a luz está sendo absorbida maioritariamente na zona non ordeada. Isto tamén é certo nos iridoplastos, onde os cloroplastos se atopan nas celulas mesofilicas debaixo dos iridoplasto situados na epidermis. Polo tanto estes , a diferenza dos bizonoplastos, non forman parte do mesmo orgánulo. Tendo en conta o sistema non illado, atopamos que os iridoplastos vólvense contraproducentes en condicións de pouca luz debido á separación da banda de parada fotónica. Ademais, os iridoplastos cobren unha área relativamente pequena da folla (~ 12 % como máximo), o que suxire que calquera efecto sobre a absorción probablemente sexa insignificante ao considerar a totalidade da estrutura da folla. A pesar diso, demostramos que a estrutura individual presenta propiedades de mellora e sintonización da absorción. Para verificar os efectos inducidos pola luz lenta, necesitamos medir experimentalmente a absorción. Non obstante, debido á complexidade do sistema natural, esta medida non se pode conseguir na estrutura biolóxica. Por ese motivo, fabricamos estruturas biomiméticas para estudar indirectamente máis as propiedades fotónicas.

Para fabricar unha estrutura biomimética de iridoplasto, necesitamos propiedades fotónicas e de absorción similares. Para imitar este último aspecto, usamos moleculas orgànicas tipo agregado J que presentan unha superposición significativa entre os niveis de enerxía doador e aceptor (é dicir, a absorción e a emisión céntranse en lonxitudes de onda similares), permitindo un transporte de enerxía eficiente similar ao sistema natural. En particular, escollemos o colorante molecular coñecido como TDBC. Para a procesabilidade, este colorante utilízase dopando un polímero hóspede, o alcohol polivinílico (PVA). Cando se deposita unha capa desta mestura, TDBC-PVA, presenta o índice de refracción do polímero hóspede (PVA) mais un oscilador lorentziano centrado na resonancia do TDBC. Aquí, a compoñente imaxinaria do índice de refracción (responsable da absorción) presenta un pico de resonancia estreito e forte a $\lambda_r = 590$ nm. En consecuencia, a parte real tamén sufrirá unha forte dispersión segundo as relacións Kramers-Kronig. Por comodidade, chamamos a este intervalo a rexión de dispersión anómala. Coa relaciònde TDBC a PVA usada no noso traballo, a forza deste oscilador é tan alta que a compoñente real da permitividade vólvese negativa dentro dun intervalo pequeno, producindo propiedades ópticas semellantes aos de un metal. As propiedades ópticas do material dopado confirmáronse mediante elipsometría. Estas propiedades inclúen a existencia de polaritóns de excitóns de superficie (SEP), equivalentes ao seu equivalente metálico, o polaritón de plasmóns de superficie.

Para imitar as propiedades fotónicas dos iridoplastos, fabricamos mediante revestimento por *spin coating* 7 DBR totalmente orgánicos con 16 células unitarias. Cada célula unitaria está composta por unha capa de poliestireno (PS), que non presenta dispersión de luz e, polo tanto (corresponderia ao estroma no sistema natural), e unha película TDBC-PVA, que corresponderia ao grana. O grosor da capa absorbente é fixo e variamos a reflexión Bragg do sistema controlando o grosor da capa homoxénea. Isto permite un enfoque máis cómodo para medir a mellora da absorción de luz lenta, xa que só se necesita unha referencia para todas as mostras, e tamén se semella ao sistema natural xa que o principal contribuínte da expansión dos iridoplastos é o medio non dispersivo.

Os resultados mostran que, cun aumento do período, obsérvase un desprazamento ao vermello na lonxitude de onda de reflexión de Bragg, como era de esperar. A forte dispersión do índice de refracción real causada pola resonancia ten como resultado unha dispersión igualmente forte do intervalo de banda fotónica na rexión de dispersión anómala. Por este motivo, obsérvanse tres bandas de parada fotónicas dentro deste intervalo: $\lambda_- < \lambda_r$, $\lambda_* \sim \lambda_r$ e $\lambda_+ > \lambda_r$. Para λ_*, pero debido á forte dispersión do material e á reflexión tipo metal,

USC UNIVERSIDADE DE SANTIAGO

non se pode observar a reflexión de Bragg. Lonxe da rexión de dispersión anómala, o oscilador lorentziano, en comparación co PVA non dopado, crea unha diminución do índice de refracción cando $\lambda < \lambda_r$ e un aumento cando $\lambda > \lambda_r$. Polo tanto, o material de índice de refracción máis alto é PS cando $\lambda < \lambda_r$ e TDBC-PVA cando $\lambda > \lambda_r$. Polo tanto, o bordo da banda fotónica con propiedades de mellora da absorción por luz lenta destes dous espazos será invertido. Ademais, o contraste do índice de refracción (Δn) entre as dúas capas orgánicas constituíntes (PS e TDBC-PVA) aumenta significativamente ($\Delta n \sim 0,1 \rightarrow 0,2$). En consecuencia, a reflectancia pode aumentar de $\sim 40\%$ a $\sim 80\%$ cando se compara un sistema non dopado con outro dopado coa mesma estrutura.

Para investigar as propiedades de luz lenta das estruturas, medimos a absorción e comparámola cunha referencia, similar ao que se fixera para os iridoplastos. Descubrimos que, como consecuencia da inversión do material de alto índice de refracción, existe unha absorción inducida pola luz lenta no bordo azul de λ_- e no bordo vermello de λ_+. Polo tanto, demostramos a mellora da absorción de luz nunha estrutura biomimética. Estes resultados e a reflexión obtivéronse teoricamente (utilizando o mesmo modelo TMM que antes) e confirmáronse experimentalmente. Para estas medicións utilizouse un microscopio de imaxe de Fourier que é capaz de medir a reflectancia enfunción do ángulo mais só a transmisión en incidencia normal. Polo tanto, restrinximos a análise das propiedades da luz lenta á incidencia normal.

O TDBC é un colorante fluorescente. Polo tanto, podemos caracterizar a emisión para investigar indirectamente a absorción do sistema. Para estudar a interacción entre as propiedades fotónicas e a absorción e emisión, realizamos dúas probas. En primeiro lugar, medicións de fotoluminiscencia (PL), onde a enerxía de excitación está fixada nunha enerxía superior ao excitón e medimos a emisión dependente da lonxitude de onda. En segundo lugar, a excitación por fotoluminiscencia (PLE) onde variamos a enerxía de excitación mentres medimos a emisión a unha lonxitude de onda fixa. A partir do primeiro, descubrimos que cando o intervalo de banda fotónica coincide coa lonxitude de onda de emisión, prodúcese a atenuación da fotoemisión de TDBC-PVA, aínda que a luz estea a ser absorbida. A partir deste último, observamos unha emisión reducida cando o intervalo de banda fotónica coincidía coa enerxía de excitación, polo que non permitía a absorción en primeiro lugar.

O sistema mostrado aquí demostra a posibilidade de mellorar a absorción inducida pola luz lenta, aumentar as propiedades fotónicas e a sintonizacón. É importante destacar que isto conseguiuse utilizando materiais totalmente orgánicos. Normalmente, as estruturas fotónicas fanse utilizando materiais inorgánicos que requiren maquinaria económica e ambientalmente cara para producir. As propiedades similares aos metais do TDBC-PVA tamén poderían substituír aos metais para certas aplicacións fotónicas. Os metais presentan inconvenientes similares aos materiais inorgánicos. Ademais, os materiais orgánicos permiten sistemas flexibles e técnicas de fabricación moito máis escalables. Por estes motivos, abrise outra pregunta para futuras investigacións: podemos utilizar as técnicas de fabricación desenvolvidas e os materiais para fabricar estruturas fotónicas totalmente orgánicas que sexan máis respectuosas co medio ambiente, de menor custo e máis escalables que as estruturas tradicionais? No resto desta tese, desenvolvemos outros tres sistemas totalmente orgánicos.

Os estados ópticos de Tamm (OTS) son modos de luz confinados entre dúas estruturas fortemente reflectantes nas que o campo eléctrico decae exponencialmente coa distancia. Normalmente, estas estruturas son un DBR e unha capa metálica. Debido ao confinamento

da luz, unha pegada clara deste modo é unha resonancia cunha profundidade estreita e forte nunha reflectancia doutro xeito forte. Aínda que estudos previos demostraron que a capa metálica pode ser substituída por outra TDBC-PVA debido ás súas propiedades similares ao metal, os DBR utilizados sempre foron inorgánicos. Polo tanto, toda a gama de vantaxes dos materiais orgánicos non se aproveitou completamente. Nos solventamos esto fabricando un DBR totalmente polímerico de PS e PVA, seguido da capa excitónica orgánica, TDBC-PVA.

Debido ao baixo contraste do índice de refracción entre PS e PVA, o intervalo de banda fotónica do DBR ten un pequeno ancho de banda. Combinado coa estreita rexión óptica de tipo metal do TDBC-PVA, isto significa que, debido ao desprazamento azul da banda de parada con ángulos crecentes, un OTS só é posible para un rango estreito de ángulos, xa que o intervalo de banda de parada fotónica e o a rexión tipo metal do TDBC deben solaparse. Fabricamos dúas estruturas con diferente periodicidade: unha coa reflexión central de Bragg (con incidencia normal) a $\lambda = 630$ nm e outra a $\lambda = 608$ nm. Por este motivo, presentan o estado OTS nun rango de ángulos diferente (nótese que ningún cumpre as condicións para OTS en incidencia normal). Por exemplo, só a estrutura de periodicidade máis alta mostra un OTS a $45°$e só a de periodicidade máis baixa mostra un OTS a $35°$. Isto analizouse en primiero lugar teoricamente e despois confirmouse experimentalmente. Utilizáronse medidas de reflectancia dependentes do ángulo para confirmar a existencia deste modo nestas estruturas; observouse unha clara reduccion da reflectancia no intervalo da banda fotónica cando coincidía coa área de tipo metal do TDBC.

A natureza dispersiva do TDBC-PVA significa que a luz confinada na súa interface será maioritariamente absorbida. Utilizando un sistema de medida PLE iluminouse a mostra con luz nun ángulo de $35°$. As medicións de PLE mostran un aumento da emisión de ata un 80% na OTS. Isto demostra unha maior absorción da luz e a existencia de este modo na estructura. Para a estrutura de maior periodicidade, as medicións de PLE foron similares a unha simple película TDBC-PVA de referencia, como se esperaba pola inexistencia de efectos fotónicos nesas condicións.

Nesta tese amosamos outros dous resultados preliminares. No primeiro, demostramos a posibilidade de nanoestruturar lateralmente unha estrutura orgánica fotónica 1D. A diferenza das técnicas comúns de nanoestructuración, un patrón lateral pode créarse unicamente mediante o cambio do índice de refracción, en lugar da eliminación do material. Isto consíguese mediante o fotobranqueamento do colorante supramolecular mediante un láser verde. A destrución das propiedades excitónicas do colorante molecular foi confirmada medindo a resposta reflectante das rexións branqueadas. Con este láser, podemos crear patróns cunha precisión tan pequena como 2 μm. Usando as estruturas biomiméticas dopadas, creamos unha estrutura en forma de micro piares con dimensións laterais similares aos iridoplastos, é dicir, ~ 5 μm. En dimensións laterais suficientemente pequenas, esperamos que as propiedades fotónicas se limiten á incidencia normal. Non obstante, non observamos diferenzas entre este piar multicapa confinado lateralmente e unha multicapa non confinada lateralmente, o que suxire que non hai ningún efecto de confinamento lateral da luz no sistema.

En segundo lugar, creamos engurracions a escalas ópticas para acoplar o SEP de TDBC-PVA a ángulos máis baixos. Para ter unha estrutura totalmente orgánica, utilizamos unha técnica coñecida para crear PDMS engurrado. Consiste en estirar un substrato de PDMS e expoñelo a un tratamento con plasma de osíxeno. Este proceso crea unha capa dura parecida á sílice sobre o substrato. Cando a tensión se libera do substrato brando, volve á súa

USC UNIVERSIDADE

lonxitude inicial e a compresión provoca unha inestabilidade de pandeo na película da parte superior dura, facendo que se engurra. Demostramos que controlando o tempo de exposición ao proceso de plasma de osíxeno, podemos controlar o período das engurras creadas. Ao xirar o revestimento de TDBC-PVA sobre o substrato PDMS estirado, podemos facer que a capa dopada con colorante se engurra co substrato. Demostramos que a difracción óptica causada pola estrutura da reixa traduce o SEP de TDBC-PVA (que, en condicións normais, só existe máis aló da liña de luz) a ángulos baixos.

En resumo, nesta tese comezamos analizando teoricamente cloroplastos fotosintéticos fotónicos. Demostramos que os iridoplastos poden mellorar a absorción da luz e poden afinar a súa cor estrutural. Ademais, demostramos que todos os cloroplastos (fotónicos ou non) poden sintonizar a súa absorción de luz dependendo das condicións de luz. A pesar da capacidade de absorción de luz mellorada dos iridoplastos, esta probablemente non sexa a súa vantaxe biolóxica xa que a súa contribución á absorción global de luz da folla é insignificante. Fabricamos unha estrutura biomimética para iridoplastos onde demostramos unha multicapa totalmente orgánica con propiedades fotónicas melloradas, multipe bandas de parada fotónicas e unha mellora da absorción inducida por efectos de luz lenta. Usamos as técnicas desenvolvidas e os materiais empregados aquí para fabricar estruturas fotónicas totalmente orgánicas. En primeiro lugar, mostramos un sistema que presenta un estado Tamm óptico sensible ao ángulo. En segundo lugar, demostramos a posibilidade da nanoestruturación, sen eliminar material. En terceiro lugar, fabricamos unha rede TDBC-PVA para acoplar o SEP a ángulos máis baixos. Agardamos que esta tese incentive o desenvolvemento de cristais fotónicos totalmente orgánicos que presentan varias vantaxes sobre os inorgánicos tradicionais, como menores custos financeiros e ambientais, máis fácil escalabilidade e flexibilidade.

USC
UNIVERSIDADE
DE SANTIAGO
DE COMPOSTELA

USC
UNIVERSIDADE
DE SANTIAGO
DE COMPOSTELA

Acknowledgements

Academia is no lone work. Teamwork and guidance are always present, no matter the discipline or the project. Throughout the research presented in this thesis, many challenges and difficulties arose. Many of which could not have been overcome without the help of other people. For this reason, I want to dedicate this dissertation to all the people who have supported me, directly or indirectly:

- Martin Lopez-Garcia, my supervisor for the constant guidance and for the terrific support. I could not have asked for a better person to guide me through this journey.
- William Wardley and Johannes Goessling for being excellent role models from the start. My learning curve was extremely steep in great part thanks to them.
- Sara Nuñez-Sanchez, for the collaborations and insight on many important steps.
- Vicente Moreno de las Cuevas, for helping me deal with extensive and tiresome bureaucratic processes.
- Daniel Miranda, for being an exceptional student with remarkable skills and commitment.
- Francisca Guedes, José Gama, Rafael Vilarinho, and Pedro Fernandes for good times within the group and being committed to their research.
- Last, but not least, my partner in life, Micaela, for being present physically and spiritually.

USC
UNIVERSIDADE
DE SANTIAGO
DE COMPOSTELA

USC
UNIVERSIDADE
DE SANTIAGO
DE COMPOSTELA

Research Infrastructures

The research presented hereafter was primarily developed at the International Iberian Nanotechnology Laboratory, in Braga, Portugal, and counted with the extensive use of the following research facilities:

- **CINBIO at the University of Vigo**: Where the theoretical understanding and the fabrication techniques of an important material used were developed.
- **Laser Processing Group at the Consejo Superior de Investigaciones Científicas**: Performed the necessary measurements and analysis to understand the optical properties of an important dye used.

Funding Acknowledgements

I would also like to acknowledge the funding that has made this research possible. In particular, the "Towards Biomimetic Photosynthetic Photonics" Project (POCI-01-0145-FEDER031739) cofunded by FCT and COMPETE2020. A PhD scholarship was also offered by FCT, the IACOBUS program allowed for a two month secondment at the University of Vigo, and a Seed grant offered by the International Iberian Nanotechnology Laboratory which allowed for the development of a side project.

USC
UNIVERSIDADE
DE SANTIAGO
DE COMPOSTELA

USC
UNIVERSIDADE
DE SANTIAGO
DE COMPOSTELA

Contents

Contents xxiii

Acronyms xxv

List of Figures xxvii

List of Publications xxxiii

Preface 1

I Introduction and methods 3

1 Introduction 5
- 1.1 Basic principles of photosynthesis and chloroplasts . . . 5
- 1.2 Photonic Crystals and Slow Light . . . 10
  - 1.2.1 Distributed Bragg Reflectors . . . 11
  - 1.2.2 Slow light in photonic crystals . . . 13
  - 1.2.3 Applications and fabrication . . . 15
- 1.3 Natural photonic crystals . . . 16
  - 1.3.1 Photosynthetic photonic structures . . . 17
  - 1.3.2 Thylakoid dynamics under different light conditions . . . 21
- 1.4 TDBC as a biomimetic pigment . . . 23
  - 1.4.1 Polaritonic properties of TDBC . . . 26
- 1.5 Motivations and objectives . . . 28

2 Methods 31
- 2.1 Transfer Matrix Method . . . 31
- 2.2 Spin coating for consistently high-quality DBRs . . . 34
- 2.3 Fourier image spectroscopy . . . 40
  - 2.3.1 Basic principles . . . 41
  - 2.3.2 Set-up . . . 44
  - 2.3.3 Collecting the Fourier image . . . 46
  - 2.3.4 Data extraction from the Fourier image . . . 48

USC UNIVERSIDADE DE SANTIAGO DE COMPOSTELA

II Publications **51**

3 Light-Dependent Morphological Changes Can Tune Light Absorption in Iridescent Plant Chloroplasts: A Numerical Study Using Biologically Realistic Data *53*

4 Enhanced Light Absorption in All-Polymer Biomimetic Photonic Structures by Near-Zero-Index Organic Matter *55*

***5* Tunable narrowband Excitonic Optical Tamm States enabled by a metal-free all-organic structure** *57*

III Results and discussion **59**

6 Discussion of the publications **61**
6.1 Theoretical analysis of photonic chloroplasts . . . 61
6.1.1 Conclusions and comments . . . 63
6.2 Biomimetic iridoplast . . . 65
6.2.1 Conclusions and comments . . . 68
6.3 All organic Tamm state . . . 70
6.3.1 Conclusions . . . 71

7 Nanostructured photonic crystals **73**
7.1 Laterally confined iridoplast biomimetic . . . 73
7.1.1 Introduction . . . 73
7.1.2 Fabrication and characterisation . . . 74
7.1.3 Laterally confined photonic structure . . . 76
7.2 Wrinkled TDBC-PVA as a grating system to access Surface exciton polaritons 78
7.2.1 Introduction . . . 78
7.2.2 Fabrication methodology and theoretical background . . . 80
7.2.3 Results . . . 82

IV Conclusion **87**

8 Conclusion and future work **89**

Bibliography **91**

A Supplementary **119**

USC
UNIVERSIDADE DE SANTIAGO DE COMPOSTELA

Acronyms

v_g	group velocity
1D	one-dimension
2D	two-dimensions
3D	three-dimensions
BFP	Back Focal Plane
DBR	Distributed Bragg Reflector
FRET	Förster Resonance Energy Transfer
FT	Fourier Transform
FWHM	Full Width at Half Maximum
IR	Infra-Red
NA	Numerical Aperture
NZI	Near-Zero Index
OTS	Optical Tamm States
PAR	Photosynthetic Active Radiation
PhC	Photonic Crystal
PMMA	Poly(methyl methacrylate)
PS	Polystyrene
PVA	Poly(vinyl alcohol)
SEM	Scanning Electron Microscope
SEP	Surface Exciton Polariton
SPP	Surface Plasmon Polariton
TEM	Transmission Electron Microscope
TMM	Transfer Matrix Method
UV	Ultra-Violet
VIS	Visible

USC UNIVERSIDADE DE SANTIAGO COMPOSTELA

USC
UNIVERSIDADE
DE SANTIAGO
DE COMPOSTELA

List of Figures

1.1 **Structure of the photosynthetic organism** (a) Schematic of chloroplasts within the leaves of plants. The insets represent, in order, leaf cells, chloroplast cross-section, granum, and thylakoid membranes. Extracted from reference [2]. (b) Photosynthetic complexes within the thylakoid membranes and main light-dependent chemical reactions in photosynthesis. Extracted from reference [8]. 7

1.2 **Light in photosynthesis** (a) Wavelength dependent light spectrum at sea level available for photosynthesis. The region in rainbow represents the Photosynthetic Active Radiation [29]. (b) Absorption spectrum of three of the most important pigments in photosynthesis [2]. Light intensity distribution in the 2D cross section of a grana (c) and the 3D environment of the chloroplast composed of grana (d). Extracted from reference [6]. 9

1.3 **Photonic crystals**. Schematic of a 1D, 2D, and 3D photonic crystal, extracted from reference [37]. The different colours represent materials with different refractive indices. 11

1.4 **Dispersion relation of 1D photonic crystals**. Each plot corresponds to a similar multilayered structure composed by two materials with refractive indices n_1 and n_2. They have different refractive index contrasts ($\Delta = |n_1 - n_2|$): left plot $\Delta n = 0$, centre plot $\Delta n = 0.14$, and right plot $\Delta n = 2.6$. Extracted from [37]. 12

1.5 **Optical properties of DBRs**. (a) Normal incidence reflectance of an organic (red) and an inorganic (black) 1D photonic structures, both centred at 550 nm. (b) Angle-dependent s-polarised photonic band gap of the same structures. 14

1.6 **Slow light in a DBR**. (a) Optical band structure of a Bragg mirror in Energy and momentum. The red and blue lines correspond to the low and high energy modes respectively. At the photonic band gap edge these modes start bending, creating the standing waves represented to the right. Here the striped red rectangles represent the absorptive material with higher refractive index. (b) Absorption in a dispersive bulk media (solid line) and in the structured system represented in the inset, with the same volume of absorptive material (dashed line). Extracted from reference [55]. 16

USC UNIVERSIDADE DE SANTIAGO DE COMPOSTELA

1.7 **Natural photonic structures**. (a) Feather of an adult peacock (*Pavo cristatus*) and (b) TEM image of the cross-section of the photonic structure; scale bar is 1 μm [101]. (c) *Morphos sulkowskyi* butterfly and (d) the SEM image of the scales of the wing; scale bar is 500 nm [102]. (e) *Chondrus crispus* red algae and (f) TEM of the cross-section of cuticle; scale bar is 2 μm [94]. (g) *Pollia condensata* fruit and (h) TEM of the cellulose of the cell wall; scale bar is 250 nm [95]. 18

1.8 **Photosynthetic photonic structures**. (a) Photograph of a *Begonia pavonina* leaf which looks blue due to the presence of numerous iridoplasts seen in the inset under an Epi-illumination (reflectance) optical microscope. (b) SEM image of a cross-section of an iridoplast; the scale bar is 1 μm. (c) Schematic of the nanostructure of iridoplasts representing the SEM close-up image. (d) The reflectance of an iridoplast under normal light incidence. Extracted from [1]. (e) TEM image of the cross-section of a bizonoplast in *Selaginella erythropus*. The white dashed line separates the structured and non-structured zones of the organism; the scale bar is 5 µm. (f) Close-up of the previous subfigure showing the layered structure. The scale bar is 0.5 µm. Extracted from [111]. . 19

1.9 **Absorption enhancement and Photoluminescence measurements of iridoplasts**. (a) Top: Absorption enhancement factor (γ) of iridoplasts under two different periods (Δ). Bottom: normalised Photosynthetic Active Radiation (PAR) under direct sunlight and under the forest canopy (where *Begonias* are found). (b) Fluorescence images of the chlorophyll in chloroplasts (top) and iridoplasts (bottom). (c) Maximum quantum yield (F_v/F_m), with measurement's standard deviation, of PSII for guard cell chloroplasts, iridoplasts and mesophyll chloroplasts. Extracted from [1]. 21

1.10 **Thylakoid light response**. Low and high light-adapted thylakoids of a standard chloroplast. Extracted from reference [126]. 22

1.11 **Schematic of the J- and H- aggregate main properties**. On top, the optical properties (absorption and fluorescence) of aggregate dyes in their monomer form are shown. On the bottom, the shift of these properties is shown for H- and J-aggregates in red and blue lines. The shaded regions represent the properties of the monomer. Extracted from reference [133] 24

1.12 **TDBC-PVA optical properties**. (a) On top, simulations of the reflectance and absorption of a 50 nm thick TDBC-PVA layer. On the bottom, the real and imaginary permittivity of bulk TDBC-PVA. The shaded region represents the wavelengths at which the real permittivity is negative. Inset shows a photograph of a similar structure over a black background. The dotted vertical line gives the exciton of TDBC-PVA. Lorentzian strength (f_0) dependent (b) imaginary and (c) real components of the permittivity of TDBC-PVA. 26

USC
UNIVERSIDADE DE SANTIAGO DE COMPOSTELA

1.13 **Surface plasmon and exciton polariton**. (a) Plasma in metals interacting with light coupled to the surface along the x-axis, creating a SPP. This coupling exists only for TM (or H) light. Extracted from reference [181]. (b) Anti-crossing between the plasma frequency and the metal/air light line. Extracted from [182]. (c) Simulated momenta-dependent reflectance of a 50 nm layer of gold (top) and TDBC-PVA (bottom) to air for the different polarisations. Metallic-like region of TDBC-PVA caused by the negative permittivity is represented by the orange area. 27

2.1 **Multilayer schematic**. Dielectric structure with N layers. 34

2.2 **Spin coating steps**. (a) Deposition of the polymeric solution. (b) Spin-up by initiating the rotation. (c) Spin-off, turning off the rotation when the polymer has been uniformly spread throughout the substrate thanks to the centrifugal force. (d) Evaporation of the solvent to dry the sample [217]. 35

2.3 **Spin coating calibration curves**. (a), (b), (c): calibration curve of Polystyrene and Poly(vinyl alcohol) polymer solution under different weight percentage concentrations and on different surfaces. (d) and (e): TDBC-PVA and Polystyrene calibration on top of one another. TDBC-PVA solution as explained in the manuscript. (f) Polystyrene calibration curve for a fixed frequency and varying weight percentage concentrations. Error bars represent the standard deviation of all the samples measured at a specific condition. If the number of samples used to calibrate per point is smaller than 5, instead of the standard deviation, the different individual points are shown. 38

2.4 **All polymer DBR**. Normal incidence (a) Bragg wavelength (nm) and (b) absolute reflectance (%). The axes represent the Cartesian coordinates (x and y) of the sample measured. Points closer than 5 mm from the border (i.e. $5 > x, y > 20$) were not measured, explaining the white space. There are, in total, 25 points measured in these plots. (c) S-polarised angle-dependent reflectance (%) measurement of one point of the sample. (d) Cross section of the previous along wavelength plot at normal incidence and at a higher angle. (e) and (f) are photographs of the sample measured at normal incidence and at a high angle. White x and y arrows represent the Cartesian coordinates used in (a) and (b). 40

2.5 **Back Focal Plane of a thin lens**. (a) Incidence of a plane wave onto a lens at an angle θ. (b) The Fourier transform of light reflected from a mirror is induced by a lens 42

2.6 **Ray tracing in objective lenses**. An oil immersion lens where F_1 and F_2 are the real and Fourier image respectively, SS is the spherical surface of the lens, α is the maximum angle of capture, f is the focal length, n is the refractive index of the medium (which matches that of the substrate and lens for the oil), WD is the working distance of the lens, t_g is the thickness of the substrate, PP_1 is the first principal plane, PP_2 is the second principal plane. Adapted from reference [261]. 43

USC
UNIVERSIDADE DE SANTIAGO DE COMPOSTELA

2.7 **Fourier microscope setup**. Schematic of the set-up used to perform angle-resolved reflectance measurements and normal incidence transmission. Note that the microscope cage is simplified since, in reality, it presents a 3D structure where the 50/50 beam splitter sends light upwards. BS stands for beam splitter, L for lens and f for the focal length of that lens. 45
2.8 **Fourier image of a grating**. The inset represents the grating with a period of 555 nm. (a) Unfiltered and filtered light at (b) $\lambda = 480$ nm and (c) $\lambda = 650$ nm. The X and Y axes represent the direction along the grating and the direction of reflection. 46
2.9 **Spectrometer**. Illustration of the light path inside a spectrometer. Extracted from [263]. 47
2.10 **Fourier image reflectance**. (a) Unprocessed and (b) processed reflectance data. In the latter, the grating equations for the exit (solid) and reenter (dashed) of light in the grating are seen for the first two orders of diffraction (black is the first and red is the second). (c) Horizontal cross-section at an increasing wavelength. 49

6.1 **Slow light in the non-isolated system**. (a) Schematic representing the structure considered in these simulations: fixed number of grana in iridoplast and variable non-structured grana below it. (b) Light absorption enhancement factor of system composing of an iridoplast and an increasing number of non-structured grana underneath (x-axis), with morphologies under low light conditions and below the canopy PAR. Note that 100 grana underneath an iridoplast is an underestimate. (c) Cross sections of subfigure (b) for specific number of grana. (d) Total absorption enhancement below the forest canopy, using equation 6.1. The disorder was not considered for any of the plots. . . . 66

7.1 **Schematic 3D biomimetic structure**. Red coloured slabs correspond to the TDBC doped PVA and the dark grey correspond to the PS. The transparent area corresponds to the photobleached area. We aim at structuring x and y in dimensions similar to those of iridoplasts: $1 \rightarrow 10$ μm. 75
7.2 **Photobleaching dye doped DBR**. (a) Sample Δ_2 from chapter 4 is photobleached on a squared area with a size of 50 μm. The same area was photobleached 5, 10, and 15 times to ensure full photobleaching. Red and black circles correspond to the areas measured under s-polarised angle-resolved reflectance, shown in (b). (c) Cross-section at normal incidence of the angle-dependent reflectance measurements. 77
7.3 **Nanostructured dye-doped DBR**. (a) and (b) are Epi illumination images (40x objective lens) of the two 3D nanostructured systems. Insets show a close-up of the system (100x objective lens) and its dimensions; the yellow circumference represents the area measured. (c) and (d) show the angle-resolved reflectance measurements of the spots. 78
7.4 **Dispersion relation**. Folding of an SPP propagation curve on a metallic diffraction grating [175]. The red lines correspond to the SPP of a single film with no grating structure. 79

USC UNIVERSIDADE DE SANTIAGO DE COMPOSTELA

7.5 **TDBC-PVA grating fabrication methodology**. (a) Initial PDMS substrate, (b) straining it by ϵ and clamping, (c) oxygen plasma treatment. We can either release it (d) or spin coat TDBC-PVA (e) and then release it (f). 81
7.6 **Wrinkled PDMS analysis**. (a) Optical microscope image of wrinkled PDMS; inset is the Fast Fourier Transform of that image. (b) AFM measurements of the same sample. Inset represents the cross section. (c) Angle resolved reflectance measurement of the same sample. Exit (solid) and reentry (dashed) of light in the objective lens is seen for the first two orders of diffraction (black is the first and red is the second), according to equations 2.17 and 2.18. (d) Calibration of the periodicity of the wrinkles under different oxygen plasma exposure times. Horizontal line represents the median, white square represents the mean, and boxes contain between the 25 to the 75 percentile. . 83
7.7 **Wrinkled TDBC-PVA analysis**. (a) Optical microscope image of wrinkled PDMS. Yellow circumference represents the area measured. (b) AFM measurements of the same sample. The inset represents the cross-section. (c) Momenta-resolved reflectance measurement of the sample at p- and s- polarisation. The dotted black line corresponds to the first-order polariton diffraction. (d) Cross-section of subfigure (c) at $E = 2.12$ eV. 85

A.1 **Polariton observed in reflectance**. Experimentally measured angle dependent reflectance of a thin film of gold (left) and TDBC-PVA (right) using the oil immersion lens technique described in section 2.3 under the different polarisations. The gold film is 25 nm thick. The organic solution used is a 3:1 mixture of 6.0% wt. of PVA (Aldrich PVA Mw = 85000–124000) with 2% wt. of TDBC. This solution was diluted with water at a 1:1 volume ratio. It was then spin-coated at 2000 RPM onto a thin coverslip. Expected 80 nm thickness. 119
A.2 **Fabrication set-up**. The spin coater used to fabricate all organic multilayered samples. 120
A.3 **Sample damage**. Optical microscope view of a PVA monolayer after being left under the hot plate right after being spin-coated. The star-shaped figures are caused by the fast boiling of the solvent. 120
A.4 **Optical grating**. Light incident on an optical grating gets diffracted into several orders. With the exception of the 0^{th} order, longer wavelengths become diffracted at higher angles. The detected light reflected from this structure will depend on the maximum angle of capture of the lens. 121
A.5 **Random stroma spacing**. Absorption enhancement factor γ of chloroplasts with the same number of grana as iridoplasts but where each stroma spacing is given a random value between 1 and 200 nm. Averaged over 100 different structures. 121
A.6 **Topographical measurement between bleached and non-bleached regions**. They were done using an AFM. The fact that no step is observed in this measurement, shows that no change is observed in the topography between a bleached and a non-bleached region. The non-flat surface is a consequence of the low processability of TDBC. 122

USC UNIVERSIDADE DE SANTIAGO DE COMPOSTELA

A.7 **Low quality gratings**. Example of a PDMS grating sample under a strain of $\epsilon = 0.3$ where the wrinkles present considerable defects. 122
A.8 **TDBC-PVA low quality gratings**. P polarised angle-dependent reflectance and optical microscope image of TDBC-PVA gratings under different oxygen plasma exposure times: (a) 5, (b) 20, and (c) 40 seconds. These are examples where the TDBC-PVA didn't wrinkle as desired. (d) AFM of a sample of TDBC-PVA on a 40 second oxygen plasma exposure. The inset is a cross-section of the measurement. 123
A.9 **AFM of the sample in figure A.8 (d)**. This measurement was done in a part of the sample where TDBC-PVA did not spread. The topography is similar to a sample with no TDBC-PVA. 123

USC
UNIVERSIDADE
DE SANTIAGO
DE COMPOSTELA

List of Publications and Conferences

In this work, the following papers in international scientific journals were published:

Published works

1. "Light-Dependent Morphological Changes Can Tune Light Absorption in Iridescent Plant Chloroplasts: A Numerical Study Using Biologically Realistic Data" in *ACS Photonics*.
2. "Enhanced Light Absorption in All-Polymer Biomimetic Photonic Structures by Near-Zero-Index Organic Matter" in *Advanced Functional Materials*.
3. "Tunable narrowband Excitonic Optical Tamm States enabled by a metal-free all-organic structure" in *Nanophotonics*.

In preparation for publication

1. A Perspective on natural photosynthetic photonic structures in nature
2. A new methodology of depositing TDBC

In addition, the following poster and oral presentations at conferences, seminars, and symposiums were done:

1. **International Nanophotonics School** (17-21/06/2019), Summer School at AMOLF in the Netherlands. Poster presentation entitled "Towards biomimetic photosynthetic photonics: Polymer-based mimicking of natural Bragg reflectors in Begonia leaves".
2. **Bio-inspired Optics and Photonics – From Metamaterials to Applications** (24-27/06/2019), conference in Germany. Contributor to an oral presentation entitled "Photonic structures in photosynthetic organism: what are they and how to inspect them".
3. **VII Encontro da Mocidade Investigadora** (27-29/06/2019), symposium at the University of Santiago de Compostela in Spain. Oral presentation entitled “Towards biomimetic photosynthetic photonics”.
4. **International Conference on Micro and Nano Engineering** (23-26/09/2019), conference in Greece. Contributor to an oral presentation entitled "Biomimetics of photosynthetic photonic structures. How natural light-harvesting could become an inspiration for nanotechnology".
5. **V Workshop do PD** (04/10/2019), virtual workshop organised by the University of Santiago de Compostela, the University of Vigo, and the University of Coruña. Oral presentation entitled "Polymer-based mimicking of natural Bragg reflectors in Begonia leaves".
6. **INL Annual Research Symposium** (27-28/11/2019), symposium at INL in Portugal. Poster presentation entitled "Inspiration from natural photonics".

USC

7. **Photonics Online Meetup 2020** (22/06/2020), virtual conference. Poster presentation entitled "Light-induced adaptation of structural colour and light absorption enhancement in photosynthetic photonic organelles".
8. **Biological and bio-inspired optics Faraday Discussion - Living Light edition** (20-22/07/2020), virtual conference. Poster presentation entitled "Light-induced adaptation of structural colour and light absorption enhancement in photosynthetic photonic organelles".
9. **VI Workshop do PD** (09/10/2020), virtual workshop organised by the University of Santiago de Compostela, the University of Vigo, and the University of Coruña. Oral presentation entitled "Changing light environment induces optical changes of natural photonic photosynthetic organelles".
10. **INL Annual Research Symposium** (24-27/11/2020), virtual symposium. Contributed to an oral talk and presented a short video entitled "Light-induced adaptation of structural colour and light absorption enhancement in photosynthetic photonic organelles".
11. **EuroNanoForum** (5-7/05/2021), virtual conference. Poster presentation entitled "Tuneable light absorption in specialised chloroplasts can inspire new light sensitive nanotechnology".
12. **European Materials Research Society (EMRS)** (31/05-05/06/2021), virtual conference. Oral presentation entitled “Tuneable light absorption in iridescent nanostructured chloroplast”.
13. **Metamaterials**, **Photonic Crystals**, **and Plasmonics (META)** (20-23/07/2021), virtual conference. Oral presentation entitled "Light induced adaptation of structural colour and light absorption enhancement in photosynthetic photonic organelles".
14. **European Optical Society Annual Meeting (EOSAM)** (13-17/09/2021), virtual conference. Oral presentation entitled "Tuneable light absorption in iridescent nanostructured chloroplasts".
15. **Conferencia Española de Nanofotónica (CEN)** (20-22/09/2021), virtual conference. Oral presentation "Light-induced adaptation of structural colour and light absorption enhancement in photosynthetic photonic organelles".
16. **Living Light** (22-/23/2021), virtual conference. Flash talk and poster presentation entitled "Iridescent nanostructured chloroplasts can tune light absorption".
17. **VII Workshop do PD** (08/10/2021), virtual workshop organised by the University of Santiago de Compostela, the University of Vigo, and the University of Coruña. Oral presentation entitled "Near Zero-Index polymer materials can enhance light absorption".
18. **INL Annual Research Symposium** (4-5/04/2022), symposium at INL, in Portugal. Contributor for an oral talk and presented a short video entitled "Photonic applications of an exotic organic material".
19. **Greenfest** (27-30/05/2022), festival to promote sustainability in Portugal. Oral presentation entitled "A Inesperada Nanotecnologia encontrada na Natureza".
20. **META** (19-22/06/2022), conference in Spain. Contributor for a talk entitled "All-organic biomimetic photonic structures tailored by near-zero index organic materials".
21. **VIII Workshop do PD** (07/10/2022), virtual workshop organised by the University of Santiago de Compostela, the University of Vigo, and the University of Coruña. Oral presentation entitled "Natural photosynthetic nanostructures as a blueprint for bioinspired organic photonics".

USC DE COMPOSTELA

Preface

Photonics is the scientific field that studies the interactions of wave-like photons (light) with the environment. Photonic crystals provide the scaffold to manipulate light and create novel technological applications that promise to one day revolutionise much of our world. Alas, to this day, the fabrication process of these structures continues to present significant hurdles for their widespread application. These include financial, technological, and even environmental challenges. Nature, however, seems to have overcome these problems aeons ago. Photonic structures are widespread in nature and their applications are diverse: from mating, mimicry, control light exposure and even communication. Perhaps the most striking implementation, however, is the photosynthetic system known as iridoplast, found within dark dwelling plants. These are believed to use exotic photonic properties to enhance light absorption at the available light wavelengths. Despite this, research remains meagre and no experimental confirmation of this phenomenon has been observed. In this dissertation, we will develop further the theoretical background and an experimental biomimetic structure to use as a playground to indirectly study the biological role of iridoplasts. We use the fabrication techniques developed to produce all-organic photonic crystals. The materials used are unconventional but can overcome some of the hurdles in Man-made photonic structures mentioned previously.

For this dissertation, the reader is expected to understand the basics of Electromagnetism, Photonics and Optics, though some concepts are presented for clarity. Throughout this research, many other diverse topics were required, such as photosynthesis, natural structural colour, and molecular resonators. For these, a brief introduction will be provided.

USC
UNIVERSIDADE
DE SANTIAGO
DE COMPOSTELA

USC
UNIVERSIDADE
DE SANTIAGO
DE COMPOSTELA

Part I

Introduction and methods

USC
UNIVERSIDADE
DE SANTIAGO
DE COMPOSTELA

USC
UNIVERSIDADE
DE SANTIAGO
DE COMPOSTELA

CHAPTER 1

Introduction

Photosynthesis is one of the most crucial chemical reactions for life on Earth and, in higher plants and algae, chloroplasts are the main photosynthetic organelle. Light is required to start these reactions, however, despite this connection, very few studies have focused on the effects of internal light distribution and nanophotonics in chloroplasts. The first link between the two was found in iridoplasts, specialised nanostructured chloroplasts with a well-defined periodicity that produces photonic effects. Theoretical studies suggest that the structure localises green wavelengths of light at the absorptive material, thus increasing overall light absorption [1]. The photonic properties and potential biological advantages of these structures have been reported very recently, about 3 years before the start of the work presented here. For this reason, research on this system is still in its infancy and much is required to understand its photonic properties and biological advantages, both theoretically and experimentally. For example, theoretically, past studies have only considered a disorder-free and infinitely wide structure, ignoring realistic photonic structure quality loss and lateral confinement. Experimentally, due to the complexity of the biological system, absorption has not yet been measured. For this reason, a biomimetic system with similar photonic and absorptive properties can be developed to indirectly study the specialised chloroplast.

To understand and investigate these natural photonic systems, we have several fundamental topics involved that have to be considered. Photosynthesis is the ultimate goal of the structure and the photosynthetic pigments located in the system play a key role in both light absorption and the subsequent energy transport and chemical conversion. Adding to the biology and chemistry of photosynthesis and the pigments involved, we have to understand the photonic properties of periodic nanostructures as well. Finally, we have to bring all of these topics together to create an artificial photosynthetic system. In this chapter, we will present and go through these subjects to create a framework on which this research is based.

1.1 Basic principles of photosynthesis and chloroplasts

It is not an understatement to say that the sun is one of the most important elements for life on Earth. In fact, the majority of living beings on Earth ultimately derive their energy either from the sun or from these organisms which transform solar light energy together with carbon dioxide and water into chemical energy in the form of carbohydrates, such as sugars and starches. This process of energy conversion is called photosynthesis, from the Greek *phōs* (meaning "light") and *sunthesis* (meaning "putting together"). Due to its importance and

USC UNIVERSIDAD DE SANTIAGO DE COMPOSTELA

complexity, this process has been extensively studied [2–4].

The first photosynthetic organisms are thought to have been bacteria, around 3.4 billion years ago. These, however, did not release oxygen as a byproduct of the process and, for that reason, they're known as anoxygenic. It was 700 million years later that the first oxygen-producing beings emerged, the cyanobacteria. It is believed that these later evolved, endosymbiotically with other organisms, to form a more complex structure known as chloroplast, the organelle responsible for photosynthesis in plants and algae [5]. Both chloroplasts and cyanobacteria are known as oxygenic organisms because they release oxygen as a byproduct of photosynthesis. Hence, for oxygenic organisms, photosynthesis is often written in simple terms as:

$$\text{carbon dioxide} + \text{water} + \text{light} \rightarrow \text{organic matter} + \text{oxygen}.$$

Both in oxygenic and anoxygenic beings, photosynthesis relies on lipid bilayer membranes to perform many crucial chemical reactions, known as thylakoids and whose composition can be very diverse [2]. The physical distribution of these thylakoids within many photosynthetic organisms, such as cyanobacteria and diatoms, is extremely disordered. In contrast, for plant and algae cells, the thylakoids present hierarchical structure scales suitable for nanophotonic effects [6]. For this reason, in this thesis, we will focus on chloroplasts. Consequently, we will focus only on the properties and biological functions of chloroplasts hereafter.

Chloroplasts are usually present, though not exclusively, in the mesophyll cells (internal layers) of the leaf, as represented in figure 1.1 (a). They are typically between 5 to 10 μm long and consist of an inner and outer membrane enclosing several grana within a stroma medium, as suggested in the insets. The stroma medium contains enzymes crucial for carbon metabolism reactions. The grana are stacks of, typically, 3 or 4 thylakoids on top of each other. Each thylakoid consists of two stacked lipid bi-layers, known as thylakoid membranes. The bi-layers are separated by the thylakoid lumen, an aqueous medium responsible for oxygen production, electron transfer, and photoprotection regulation [7].

Within the thylakoid membrane, we can find the reaction centres of the photosynthetic complexes, such as the photosystem I and II (PSI and PSII); these execute the primary energy conversion mechanisms in the light-dependent reactions [9]. This membrane and the light-dependent chemical reactions which occur within them are described schematically in figure 1.1 (b). These encompass the absorption of light and water oxidation to oxygen, to produce redox molecules, ATP and NADPH, which are energy carriers and electron donors [10]. The redox molecules are then consumed in the light-independent carbon fixating reactions, of which the Calvin-Benson Cycle is the main pathway. These reactions occur outside the thylakoids, in the stroma, and they fixe carbon by converting carbon dioxide and hydrogen-carrier compounds into carbohydrates. These can then be used to produce other building blocks of plants such as cellulose, lipids, and amino acids or be used as an energy source by cellular respiration [11].

Reaction centres, however, do not cover a significant area of the thylakoid membranes and hence are not the main mechanism for light absorption in photosynthesis. Instead, light is mostly absorbed by the antenna complexes where an exciton is created. Antenna complexes are an array of proteins and chlorophyll and are also found within the thylakoid membranes. Generally, Förster Resonance Energy Transfer (FRET) is used as a semi-classical and nonradioactive mechanism to explain the non-radiative energy hopping between different antenna complexes [12, 13]. In this approach, a donor molecule is optically excited (by absorbing light)

USC UNIVERSIDADE DE COMPOSTELA

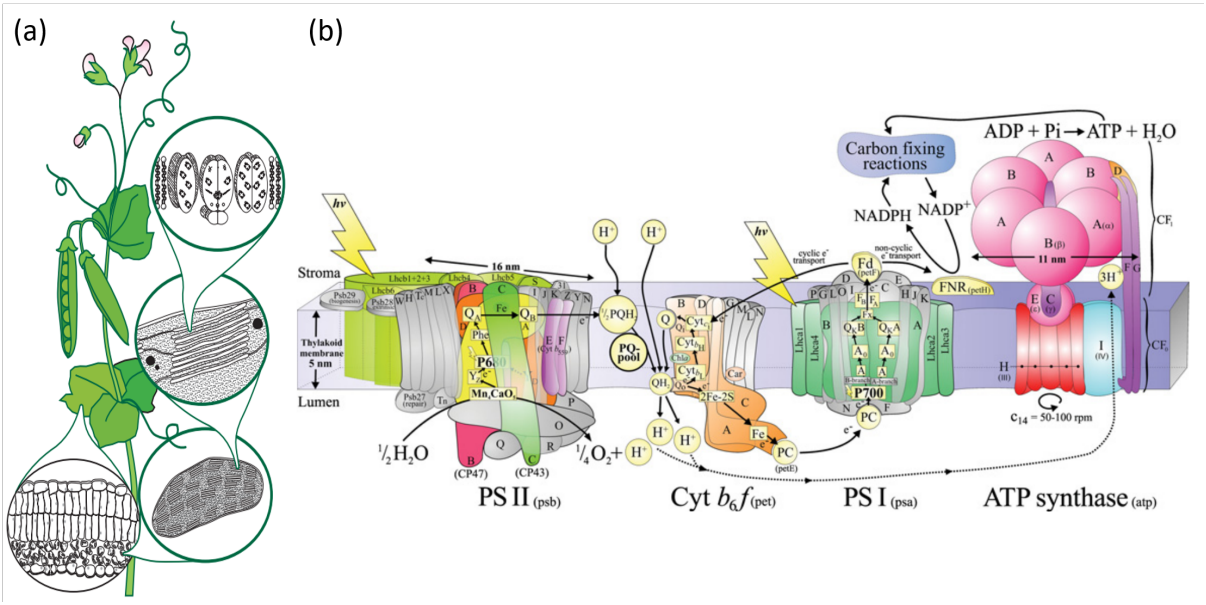


Figure 1.1: **Structure of the photosynthetic organism** (a) Schematic of chloroplasts within the leaves of plants. The insets represent, in order, leaf cells, chloroplast cross-section, granum, and thylakoid membranes. Extracted from reference [2]. (b) Photosynthetic complexes within the thylakoid membranes and main light-dependent chemical reactions in photosynthesis. Extracted from reference [8].

and transfers the excitation energy to an acceptor molecule by the interaction of their optical transition dipoles. For this transfer to take place, the emission by fluorescence spectrum of the donor and the absorption spectrum of the acceptor have to overlap, meaning that donor and acceptor molecules must have common energy states [4, 14]. Note that, this fact often leads to the wrong conclusion that energy is transferred from the emission and absorption of a photon. Energy hopping occurs between antennae until it funnels into a reaction centre.

The efficiency of FRET is inversely proportional to the distance to the sixth power, making the whole process extremely distance sensitive. However, if molecules are too close together in a large aggregate, they will easily quench, releasing the energy as heat and preventing the energy transfer to take place. For this reason, FRET based theoretical studies cannot explain the nearly 100% energy transfer efficiency that is observed during the photosynthetic process [15]. Therefore, a look beyond a semi-classical approach was taken. The quantum coherent wave-like energy transfer from absorbed photons offered a potential explanation [15, 16]. In this view, the photosynthetic pigments no longer act as independent molecules, but they couple to form a collective of excitations, creating excitons, with wave functions extending over several pigments. This observation provided a novel theory of energy transfer and many other observations have followed including in vivo and under physiological conditions [16–21]. However, direct real-space observation of the energy transfer from a donor to an acceptor (by scanning tunnelling microscopy-induced luminescence) was only reported very recently [22]. The need for a quantum coherent perspective of energy transfer in photosynthesis has however been disputed [23, 24]. The lessons learned from the energy transfer process in photosynthesis have provided valuable inspiration to develop new Man-made solar light harvesting [25].

Photosynthesis generally relies on Sunlight to initiate the many chemical reactions; however, much like other stars, the light released by the Sun comes in a spectrum of different wavelengths, each with a different intensity; figure 1.2 (a) represents this solar spectrum after going through the atmosphere. Photons with different energies will interact differently with the photosynthetic complexes [2]. For this reason, plants have developed a diverse range of pigments, such as carotenoids, lycopene, and, most crucial, chlorophyll. This last pigment can further be divided into chlorophyll A and B, both found in PSI and PSII, and, as figure 1.2 (b) suggests, they are responsible for the absorption of mainly blue and red light, thus diffusively reflecting the remaining colour: green. This ultimately gives that colour to leaves [26]. Carotenoids are also one of the most common pigments and they are responsible for the absorption of blue and green wavelengths and the photoprotection of the system [27]. Figure 1.2 (b) represents the normalised absorption spectrum of the aforementioned pigments. Photosynthetic complexes can only process solar radiation between 400 to 700 nm (similar but not equal to the VIS light). This range is known as the Photosynthetic Active Radiation (PAR). We should note, however, that far-red photons (701 to 750 nm wavelength) have recently been suggested to contribute to photosynthesis equally to traditional photons within this range and have, for that reason, been suggested to be included within the definition of PAR [28]. Due to the novelty of this discovery, we will not be including these in our study. Note that we express PAR as the Photosynthetic Photon Flux Density, which is typically expressed in micromoles per square meter per second since this provides the most useful information for this work.

From inspection of figure 1.2 (a), we see that, within the PAR, the light radiation remains roughly flat for different wavelengths. However, we should note that this spectrum occurs under optimal conditions when there are no obstacles between the atmosphere and the photosynthetic organism. Frequently, there are obstacles such as clouds, mountains, and/or even a canopy of trees between the atmosphere and the photosynthetic organelle. These can highly attenuate the wavelengths available for photosynthesis [29]. Moreover, the light conditions can change within minutes, days, and generations. For this reason, photosynthetic organisms have developed light-sensitive techniques to adjust to the ever-changing light conditions. Depending on the time frame, the mechanisms for these light-induced adjustments are known as the response (minutes), acclimation (days or weeks), or adaptation (generations). These include changes both in chemical properties and morphology [30, 31]. Despite the extensive literature, the nanophotonic properties from the induced structural changes are scarce [6]. In chapter 3, we extend this study and investigate their possible function from a nanophotonic point of view. The flexibility to different light conditions is crucial, not only to enhance light absorption when there's little light but also to reduce it when there's too much since an overdose of light can leave the organisms with an excess of redox molecules [32] which are damaging to the system.

Due to the importance of photosynthesis, the chemical properties of the light absorption mechanisms have been thoroughly investigated [2] and biomimetic technology of this process has been used to improve light-driven carbon fixation [33]. However, the impact of the nanoscale light field distribution within chloroplasts and how light is dispersed within the photosynthetic complexes remains, for the most part, unexplored. In 2019, a theoretical study of the nanophotonic effects in chloroplasts looked into the distribution of light intensity inside the grana (figure 1.2 (c) and (d)) and found that their stratified structure could enhance light absorption through internal light scattering [6]. In fact, the link between nanophotonic

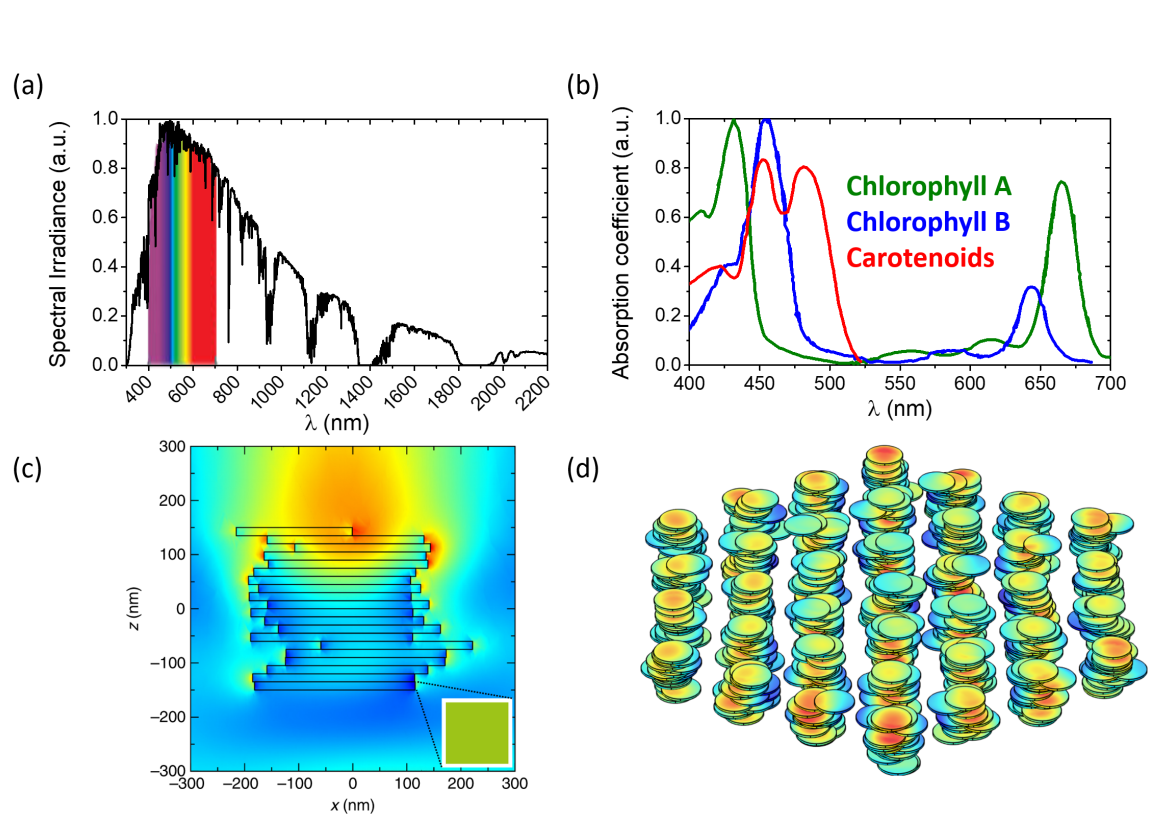


Figure 1.2: **Light in photosynthesis** (a) Wavelength dependent light spectrum at sea level available for photosynthesis. The region in rainbow represents the Photosynthetic Active Radiation [29]. (b) Absorption spectrum of three of the most important pigments in photosynthesis [2]. Light intensity distribution in the 2D cross section of a grana (c) and the 3D environment of the chloroplast composed of grana (d). Extracted from reference [6].

USC UNIVERSIDADE DE SANTIAGO DE COMPOSTELA

effects and photosynthesis was first suggested in 2016 in a study looking at the specialised chloroplast with a periodic distribution of the thylakoids, named iridoplast [1]. The periodic arrangement creates a photonic crystal which produces a strong iridescent blue colour. In the following sections, we develop a background of photonic structures to be able to study iridoplasts.

1.2 Photonic Crystals and Slow Light

A Photonic Crystal (PhC) is a structure with a subwavelength periodic refractive index (n) capable of manipulating the flow of light and producing striking optical effects. This periodicity can be represented by $n(\boldsymbol{r}) = n(\boldsymbol{r} + \boldsymbol{\Lambda})$, where $\boldsymbol{\Lambda}$ is the lattice vector and $\boldsymbol{r}$ is the three-dimensional position vector. They were first proposed in 1987 as a way to control spontaneous emission [34] and to obtain 3D Anderson localisation [35]. A one-dimension (1D), two-dimensions (2D), and three-dimensions (3D) PhC can be constructed, represented in figure 1.3. PhC can control and localise light at the nanoscale, from the Ultra-Violet (UV), to the Visible (VIS), and to the Infra-Red (IR) [36–39]. To explore the mechanism, we use as a starting point the wave equation:

$$\nabla \times \left(\frac{1}{\epsilon'(\boldsymbol{r})} \nabla \times \boldsymbol{H}(\boldsymbol{r}) \right) = \left(\frac{\omega}{c} \right)^2 \boldsymbol{H}(\boldsymbol{r}), \tag{1.1}$$

Where ω is the frequency, c is the speed of light in vacuum, $\boldsymbol{H}$ is the magnetic field, and ϵ' is the dielectric function. This is considered to be the master equation since it is the starting point to understand light propagation within any given material, for both the electric and magnetic fields. This is derived from the macroscopic Maxwell's equations which provide the fundamental basis for studying classical electromagnetism, optics, and electric circuits. The dielectric permittivity ϵ', represents the intrinsic optical properties of a material. For simplicity, the relative permittivity ($\epsilon = \epsilon'/\epsilon_0$) is typically used instead and it is related to the complex refractive index by:

$$n(\lambda) = \bar{n}(\lambda) + i\,\tilde{k}(\lambda) = \sqrt{\epsilon \mu_r} \tag{1.2}$$

In this thesis, we won't be working with magnetic materials, hence we can assume that $\mu_r = 1$ without the loss of generality. We'll mostly work with refractive index, however, when convenient, we will be changing to permittivity since they're equivalent.

Since the magnetic field is Hermitian, this wave equation can be tackled as an Eigenvalue problem, with the magnetic field being the eigenvector and $(\omega/c)^2$ being the eigenvalue. It can be shown that, due to the translational symmetry, we can apply Bloch's theorem to find the solution for PhC to the wave equation:

$$\boldsymbol{H}_k(\boldsymbol{r}) = e^{i\boldsymbol{k}\boldsymbol{r}} u_k(\boldsymbol{r}). \tag{1.3}$$

Here, $\boldsymbol{k}$ is the wave-vector and $u_k(\boldsymbol{r})$ represents a periodic function, i.e. $u_k(\boldsymbol{r}) = u_k(\boldsymbol{r} + (\boldsymbol{\Lambda}))$. For that reason, for PhC, we can restrict the eigenvalue problem to the first Brillouin zone [37].

USC UNIVERSIDADE DE SANTIAGO DE COMPOSTELA

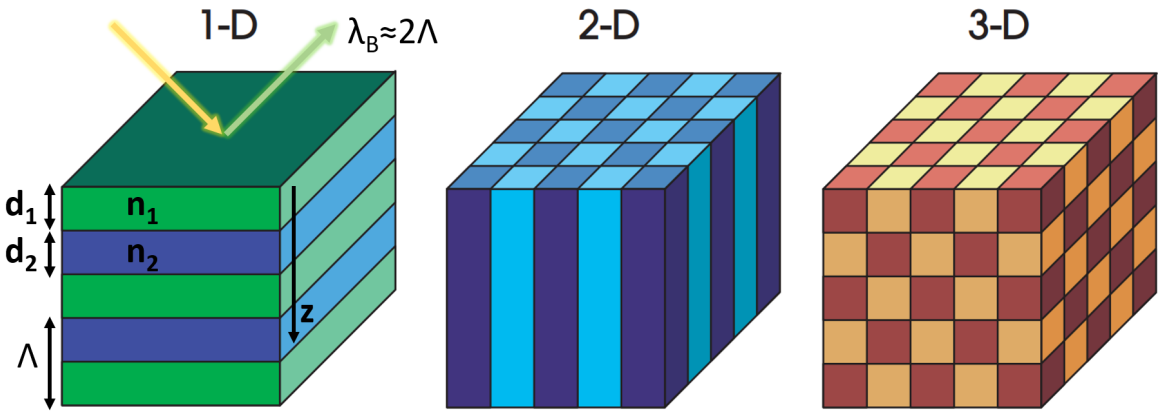


Figure 1.3: **Photonic crystals**. Schematic of a 1D, 2D, and 3D photonic crystal, extracted from reference [37]. The different colours represent materials with different refractive indices.

1.2.1 Distributed Bragg Reflectors

Starting from equation 1.3, we can calculate the photonic modes within a photonic structure. In 1D, the light distribution in the x-y plane is homogeneous and hence $k_x = k_y$ can take any value; we, therefore, represent only k_z. In figure 1.4, the modes in the first Brillouin zone for three non-dispersive 1D multilayered systems are shown in angular frequency (ω). The plot on the left shows the modes for bulk material. Because there are no interfaces, light propagates freely in the structure and modes are restricted to the material/air light line given by:

$$E = \frac{c}{n} k_z. \tag{1.4}$$

This line represents the critical angle at which total internal reflection of light occurs between the material and air. Interestingly, when a periodicity in the refractive index along the propagation direction z is added, a gap opens between the top and lower branches, as suggested in the central subfigure. This range is known as a photonic band gap or stopband. The right subfigure shows that the higher the refractive index contrast between the two constituent materials (Δn), the larger this gap. The gaps appear because electromagnetic radiation is not allowed to propagate through the system along the direction of the periodicity at these energies. This creates two important distinct bands, $m = 1$ and $m = 2$ which correspond to the low and high energy bands respectively. At the edge with the band gap, the modes bend, creating exotic photonic properties as we will see in the next subsection. Photonic band gaps are characteristic of PhC regardless of dimension, however, in this thesis, we are interested only in 1D photonic structures. The properties of these structures can be simplified by the Bragg theory.

In 1913, a father and his son found that X-ray reflected from two parallel crystalline structures separated by a distance d, created a constructive interference pattern of scattered wavefronts when $\lambda = 2d \sin(\theta)/m$. Here λ is the light wavelength, m is the order of diffraction, and θ is the angle of the incidence light [40]. The effect was named after the two scientists' surnames Bragg diffraction. Similarly, if instead of having a crystalline structure, we periodically change the refractive index between n_1 and n_2 in a system, with period $\Lambda = d_1 + d_2$ (with d representing the respective layer thickness), we can create internal con-

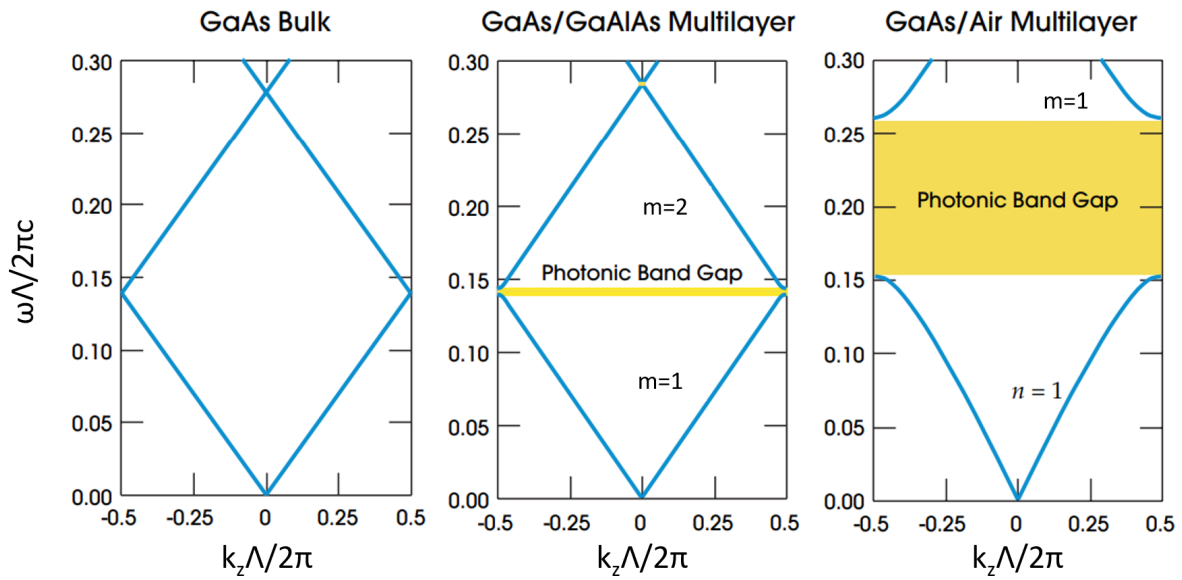


Figure 1.4: **Dispersion relation of 1D photonic crystals**. Each plot corresponds to a similar multilayered structure composed by two materials with refractive indices n_1 and n_2. They have different refractive index contrasts ($\Delta = |n_1 - n_2|$): left plot $\Delta n = 0$, centre plot $\Delta n = 0.14$, and right plot $\Delta n = 2.6$. Extracted from [37].

structive and destructive interference. Analogously, these structures will present constructive interference at the Bragg wavelength (λ_B) when:

$$\lambda_B = 2m\Lambda \cdot \sqrt{n_{eff}^2 - \sin^2\theta}. \tag{1.5}$$

n_{eff} represents the effective refractive index of the structure. At the Bragg wavelength, we obtain maximum structural induced reflection. The colour produced is known as structural colour which contrasts with "standard" colour that originates largely from pigments where light scatters and reflects uniformly in space. The strong angle dependence of these structures makes them particularly distinct even to the naked eye. The conditions necessary to obtain this increased reflection occurs when the phase gained between the two layers, at those wavelengths, corresponds to an integer of π, given by the equations known as the phase-matching condition:

$$k_{z1}d_1 + k_{z2}d_2 = (n_1d_1 + n_2d_2)\omega/c = m\pi, \text{ for m = 0, 1, 2 ...} \tag{1.6}$$

This wavelength selective reflectance is known as Bragg reflection and can be created by the 1D PhC known as Distributed Bragg Reflector (DBR) (also known as Bragg mirrors) where the aforementioned structure is repeated N times. It can be shown that the Bragg reflection is optimised when the thicknesses of the constituting layers, d_1 and d_2, are exactly a quarter of the optical length of the selected wavelength: $\lambda/4 = d_1n_1 = d_2n_2$. Because light gets partially reflected at each interface, the total reflection caused by a single pair of this structure is usually not enough to create a strong reflectance at the Bragg wavelength. However, increasing the number of these pairs (N) will create a higher number of interfaces and hence an increase in the total reflectance. For this system, and noting that the incident and

transmission medium have respectively refractive indices n_0 and n_s, the maximum reflectance at the Bragg wavelength λ_B is given by:

$$R = \left[\frac{n_0(n_2)^{2N} - n_s(n_1)^{2N}}{n_0(n_2)^{2N} + n_s(n_1)^{2N}} \right]^2. \tag{1.7}$$

From here, it's clear that a high refractive index contrast between the two alternating materials ($\Delta n = |n_2 - n_1|$) is desired. Under normal incidence, the bandwidth of the system, in frequency ν, at which light does not propagate is given by:

$$\Delta\nu = \frac{4\nu}{\pi} \arcsin \frac{n_2 - n_1}{n_2 + n_1}. \tag{1.8}$$

This range corresponds to the photonic band gap of the system where light is not allowed to propagate in the structure [41]. As demonstrated in figure 1.4, a higher contrast will increase the photonic band gap width. These solutions however, work only for this ideal quarter-wavelength stack; for more generic structures, a numerical approach, based on, for example, the Bloch theorem, is required to obtain the solutions [41]. Nonetheless, for any photonic structure, increased refractive index and number of layers will increase the photonic band gap width and strength.

To visualise these two equations, we simulate the total reflectance and photonic band gaps of two DBR. These structures have the same number of unit cells ($N = 10$) and are both centred at $\lambda_B = 550$ nm. Their distinction lies in their material composition. One DBR is made of organic material (polyvinyl alcohol (PVA) and polystyrene (PS) with $\Delta n \sim 0.1$) and the other of inorganic materials (Silicon Dioxide (SiO_2) and Silicon Nitride (Si_3N_4) with $\Delta n \sim 0.5$). Figure 1.5 (a) shows the simulated normal incidence reflectance for both systems. Since the refractive index contrast, Δn, is greater in the latter case, both the maximum total reflectance at the Bragg wavelength and the bandwidth are larger. In figure 1.5 (b), the simulated angle-dependent photonic stopband of these structures is shown where the inorganic system, again, has a much larger bandwidth. Both systems show a bending towards higher energies for higher angles of incidence, as expected from the $sin\theta$ term in equation 1.5. This is a distinctive feature of structural colour and serves as an indication of structural effects. DBRs are of particular interest in this work since we will extensively use these structures throughout.

1.2.2 Slow light in photonic crystals

Slow light refers to the phenomena by which the group velocity (v_g) of light propagating inside a system is strongly reduced: $v_g \ll c$. This represents the velocity of the overall envelope of the light wave and is defined as:

$$v_g = \frac{d\omega}{dk_z}, \tag{1.9}$$

where ω is the angular frequency. This contrasts with the phase velocity ($v_p = \omega/k$) which represents the velocity of a wave inside the medium. Similarly to the refractive index, we can define a group refractive index representing the group slow-down factor:

$$n_g = \frac{c}{v_g}. \tag{1.10}$$

USC UNIVERSIDADE DE SANTIAGO DE COMPOSTELA

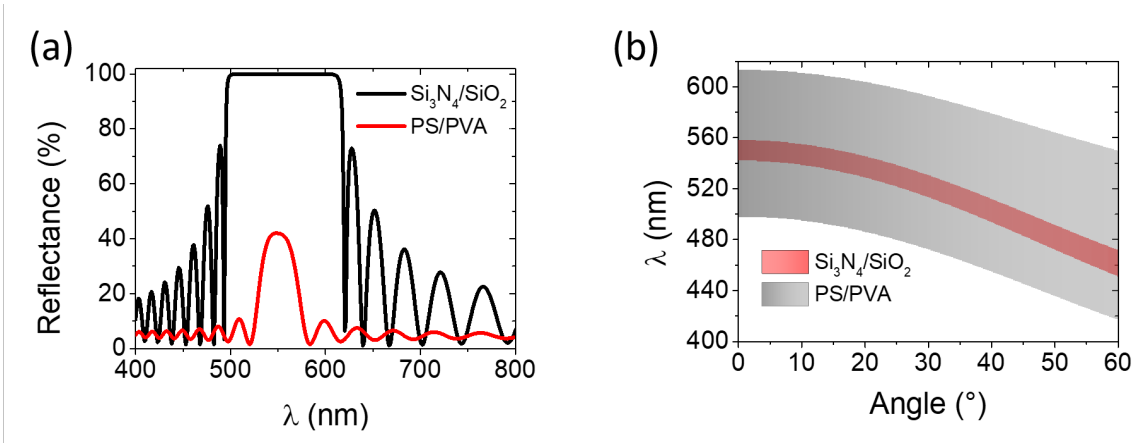


Figure 1.5: **Optical properties of DBRs**. (a) Normal incidence reflectance of an organic (red) and an inorganic (black) 1D photonic structures, both centred at 550 nm. (b) Angle-dependent s-polarised photonic band gap of the same structures.

Combining equations 1.9 and 1.10, we can write:

$$n_g = c\frac{dk}{d\omega} = n + \frac{dn}{d\omega}. \tag{1.11}$$

Considering that the first term is inherent to the material, the second term becomes key to dominate group index; therefore a material with a rapidly changing refractive index over frequency can create a strong reduction in group velocity at that particular frequency. Slow light has attracted interest for several applications, such as telecommunications [42, 43], interferometry [44], and sensing [45]. We note that when $n_g < 1$ (including negative values), we are under fast light [46, 47], though this is beyond the scope of this thesis.

The simplest way of obtaining high values for the group indices is to use materials with sharp absorption peaks. That's because, associated with this peak are rapid changes in refractive index, as required from the Kramers-Kroning relations [46], increasing the second term of equation 1.11. Brillouin scattering [43] and non-linear optical methods to control group velocity can also be used to induce slow group velocities; some examples of the latter include electromagnetically induced transparency [48] and coherent population oscillations [49].

Even though large changes in the group velocities can be achieved with bulk materials, the biggest are achieved at the edges of photonic band gaps of PhC [50]. Here the modes start bending, as seen in figure 1.4, creating a quasi-flat energy dispersion, i.e. $dE/dk_z \sim 0$, making $n_g \to \infty$, according to equation 1.10. This results in the formation of a quasi-standing light wave inside the photonic crystal, where vanishing velocities are achieved, $v_g \sim 0$, for ideal cases. Crucially, the electric field maxima of this standing wave are highly localised. At the blue edge of the photonic band gap, light is concentrated at the medium with a low refractive index whilst, in contrast, at the red edge, light concentrates at the high refractive index medium of the PhC, as suggested in figure 1.6 (a). The strong slow-down of light ensures a long lifetime for photons within the photonic crystal, resulting in stronger light-matter interactions. If the PhC is structured such that light concentrates in a dispersive material with refractive index n_d, light absorption can be enhanced when comparing a structured to a non-structured system with the same volume of absorptive material [51].

USC

To quantify photonic crystal-induced light absorption changes, we look at the transmitted light intensity (I) from a finite medium given by the Beer-Lambert:

$$I = I_0 \exp(-\alpha L), \tag{1.12}$$

where α is the absorption coefficient of the dispersive material, I_0 is the initial light intensity, and L is the path length of the absorptive material. Because the photonic crystal affects the light distribution, it fundamentally changes the absorption coefficient (α) by a dimensionless factor commonly called γ when compared to the absorption of the same volume of the same absorptive material outside a structured system (i.e. in bulk) [52]:

$$\gamma = \frac{\text{Absorption}_{\text{structured}}}{\text{Absorption}_{\text{non-structured}}} = f_{\text{over}} \frac{c/n_d}{v_g}. \tag{1.13}$$

In this equation, we have two parts. The right term expresses the ratio of the group velocity in the bulk material (c/n_d) with the group velocity in the photonic crystal (v_g), representing the slow-down effect. Importantly, the left term f_{over} quantifies the overlap of light with the dispersive material. Looking at the previous example, in figure 1.6 (a), this fraction will be maximised on the red edge, since the field concentrates in the dispersive medium, and minimised at the blue edge of the photonic band since the field concentrates in the homogeneous medium.

Figure 1.6 (b) shows the typical absorbance comparison between structured and bulk systems. At the red edge, enhancement is observed and hence $\gamma > 1$. We should note that, at the photonic band gap, light absorption is reduced since it cannot propagate in the system and hence $\gamma < 1$. Absorption enhancement can reach values $\gamma \gg 1$ if the non-structure system presents very low absorption. It is therefore not surprising that this 1D PhC induced slow light effect has attracted much research to areas such as bio-sensing [53] to light harvesting in solar cells [54–56].

1.2.3 Applications and fabrication

The fabrication of 1D PhC typically requires techniques such as sputtering [57] or PECVD (Plasma-enhanced chemical vapour deposition) [58]. For higher dimensions, Electron Beam Lithography or Focused Ion Beam microscopy are typically used [59]. Despite the high quality of the structures produced, structural disorder is found within the dimensions of the system. For example, the disorder in 1D is given by the variation from the ideal thickness for each individual layer. Yet, photonic structures have been found to be resilient to disorder in the structure by preserving their photonic properties, such as structural colour, slow-light effects, and wave-guiding, albeit attenuated [60, 61]. Together with their simplicity, this makes DBRs ideal for real-life applications. For these reasons, Bragg mirrors have been subject to a tremendous amount of research and applications, such as a touchless fingerprint motion tracking screen [62], plasmon-based sensing [63], bacterial contaminants sensor [64], creation of single photons [65], vapour sensors [66], humidity sensors [67], or strain sensors [68]. For higher dimensional structures, waveguides have been extensively studied for their potential to produce next-generation photonic circuits [69].

USC UNIVERSIDADE DE SANTIAGO DE COMPOSTELA

In addition, defects can also be added to DBRs to break the symmetry of the structure and create a $\lambda/2$ Fabry-Pérot nanocavity where light is concentrated [37]. Under a large

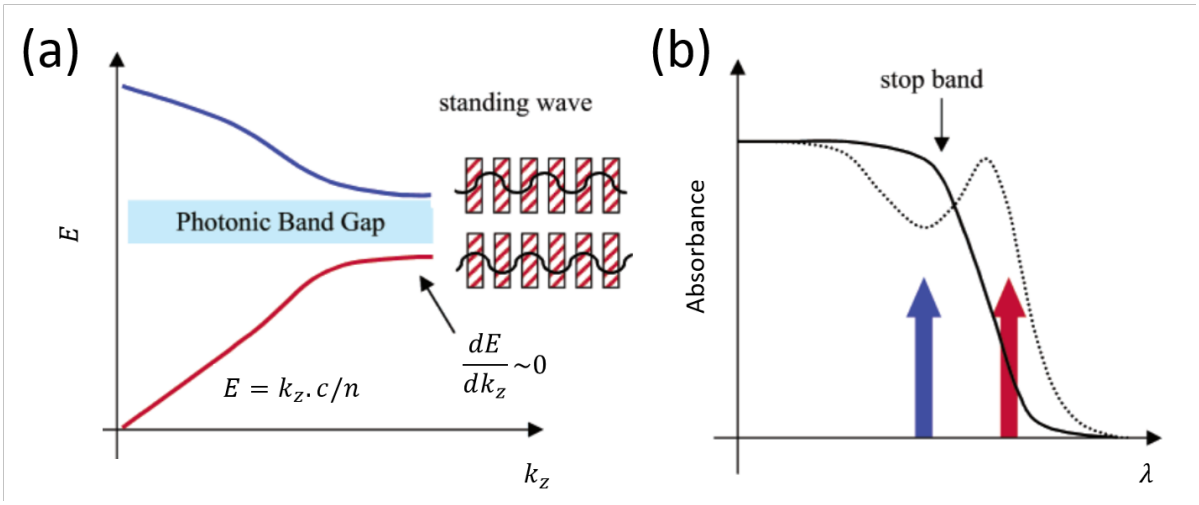


Figure 1.6: **Slow light in a DBR**. (a) Optical band structure of a Bragg mirror in Energy and momentum. The red and blue lines correspond to the low and high energy modes respectively. At the photonic band gap edge these modes start bending, creating the standing waves represented to the right. Here the striped red rectangles represent the absorptive material with higher refractive index. (b) Absorption in a dispersive bulk media (solid line) and in the structured system represented in the inset, with the same volume of absorptive material (dashed line). Extracted from reference [55].

enough confinement, strong coupling between two states, typically one light and another matter, can be reached; this regime is discussed further in chapter 1.4, though not in cavities. A similar light confinement mode can also be found at the interface between two highly reflective mirrors such as a DBR and a metallic layer. This mode is called Tamm state [70, 71] and its properties will be studied in depth in chapter 5.

Despite the many advantages and potential technological applications of PhC, the fabrication of these structures presents major hurdles. The manufacturing techniques used require high up-front costs to acquire the tools needed (hundreds of thousands of euro), which then require consistent maintenance, are slow, have a large energy consumption, and produce small areas. Solutions such as nanoimprinting [72, 73] and self-assembly [74–76] fabrication techniques have been developed; these, however, do not solve all these hurdles entirely and come with other disadvantages. For these reasons, researchers have been focusing on natural photonic structures to use as scaffolds to develop bio-inspired and biomimetic structures [77–84].

1.3 Natural photonic crystals

In 1665, Robert Hooke published a book, titled *Micrographia*, where he studied, with the aid of one of the first microscopes, several insects, animals and plants. Here, Hooke documented, for the first time, the existence of iridescent colouration caused by the refraction within microscopic structures in the feathers of peacocks [85]. Though he could not explain the formation process, he had unknowingly uncovered, for the first time, a photonic crystal. In the following century, in 1704, Newton explored this further [86]. However, it was only in

1803 that Thomas Young was finally able to explain the wave interference process causing the bright reflections [87]. At the end of the same century, in 1892, structural colour was distinguished from standard colouration and an extensive study on many animal species was performed [88]. Despite understanding that this colour was the result of interference between reflected light waves, the observation of the PhC creating this effect was not possible due to the lack of advanced microscope techniques. It was only after the development of the Scanning Electron Microscope (SEM) and Transmission Electron Microscope (TEM), in the 1940s, that the photonic structure responsible was observed and studied accurately [89], though the theory had not been fully developed yet.

Structural colour can appear all over nature, from animals to insects, to algae, to fruits and even plants [90, 91]. Some common examples of structural colour and their photonic structures are found in figure 1.7: peacock feathers, *Morphos* genus butterfly wings, *Chondrus* red algae, and *Pollia* genus berries. The biological advantages of the photonic structures are diverse. Peacocks use their structural colour to attract mating partners [92]; *Morphos* butterflies for mating, mimicry and alert [93]; *Chondrus* red algae are thought to use PhC to reduce UV light exposure [94]; and the *Pollia* berry are thought to use their bright colour to attract birds which might use them for matting displays, thus acting as seed dispersers [95].

Photonic structures playing a role in photosynthesis can also be found in many other species. Giant clams have 3D PhC to spatially distribute light to their photosynthetic complexes [96] and brown algae of the genus *Cystoseira* have developed opal-like structures with a similar role [97]. Interestingly, in the latter example, the photonic properties are also seen turning off under high light conditions [98]. At a smaller scale, a species of diatoms, microalgae found in (almost) every natural body of water, have an exoskeleton with nanophotonic properties, though their biological advantage remains unknown [99, 100]. Finally, the structural colour in certain photosynthetic organisms found in the leaves of particular dark-dwelling plants is thought to be responsible for enhanced light absorption by slow light, having a direct impact on the photosynthetic activity of the system [1]. These are known as iridoplasts and, in contrast to the structures mentioned in this paragraph, iridoplasts are simultaneously photonic and photosynthetic.

1.3.1 Photosynthetic photonic structures

Structural colour in leaves was first investigated in the late 1890s, however, it was only in the 1970s that light interference on specialised chloroplasts was found to be the cause of this colouration [103]. Structural colour in plant leaves was found to be widespread in tropical forests in tropical regions such as Africa, South America, and Southeast Asia. These peculiar plants were extensively studied, particularly with the aid of the SEM and the TEM to observe their structure, in species such as the vascular plants of the genus *Selaginella* [104, 105], the ferns of the genus *Teratophyllum* [106], *Danaea*, and *Trichomanes* [107], and the flowering plants of the genus *Begonia* and *Phyllagathis* [108]. Even though in all of these examples the bright colouration comes from structured chloroplasts, they present distinct arrangements and sizes. For flowering plants, the specialised iridescent chloroplasts are circular with 5 to 10 μm in diameter and the term iridoplast was coined for their strong iridescent colour. Figure 1.8 (a) shows the blue leaf of a *Begonia pavonina* caused by the presence of numerous blue iridoplasts, seen in the inset. Subfigures (b) and (c) present the structure of this specialised chloroplast and show that the periodicity is created by a consistent separation of the grana

USC UNIVERSIDADE

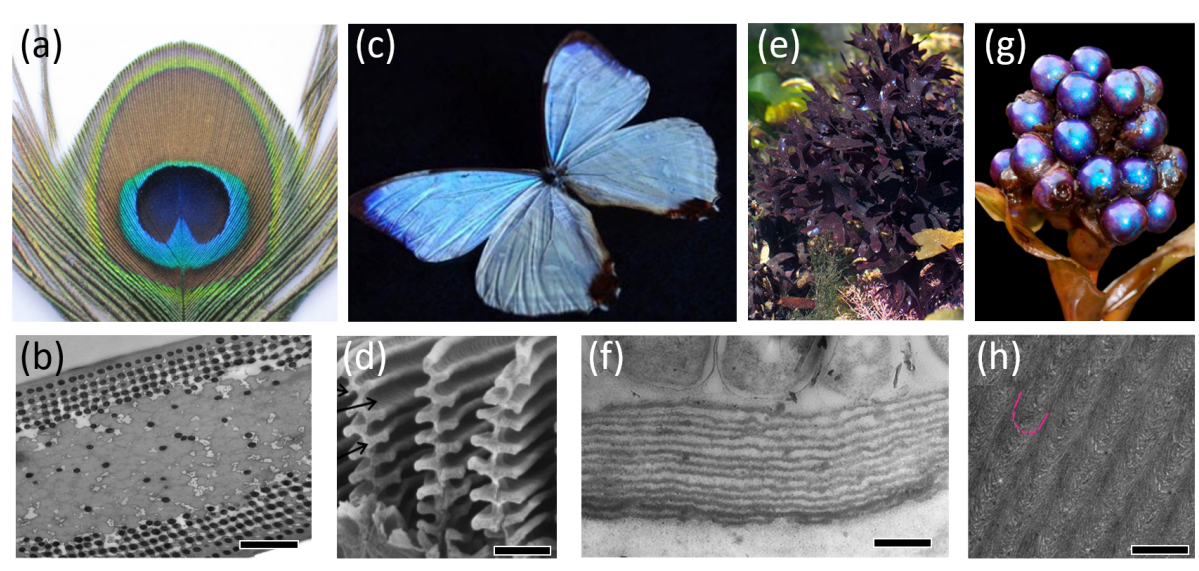


Figure 1.7: **Natural photonic structures**. (a) Feather of an adult peacock (*Pavo cristatus*) and (b) TEM image of the cross-section of the photonic structure; scale bar is 1 μm [101]. (c) *Morphos sulkowskyi* butterfly and (d) the SEM image of the scales of the wing; scale bar is 500 nm [102]. (e) *Chondrus crispus* red algae and (f) TEM of the cross-section of cuticle; scale bar is 2 μm [94]. (g) *Pollia condensata* fruit and (h) TEM of the cellulose of the cell wall; scale bar is 250 nm [95].

stacks, yielding a structure analogous to a DBR. To study the photonic properties of this system, the refractive index of the different materials is fundamental.

Similar to the standard chloroplasts, there are three main components in iridoplasts: lumen, stroma, and thylakoid membranes. The first two components are aqueous solutions with low concentrations of proteins dispersed. For this reason, the homogeneous refractive index of water (fixed at 1.33 for all wavelengths) is typically used for a theoretical description [1]. It is, however, in the thylakoid membranes where the absorptive pigments are found and hence a more complex approach is required. They can be approximated as dielectric transparent materials with strongly absorbing pigments, resulting in an effective medium approximation. To date, no study has extracted the refractive index from the thylakoid membranes of iridoplasts. However, this has been calculated indirectly from measurements of the thylakoid membranes in standard chloroplasts [109]. For this reason, this same refractive index is used in theoretical studies of iridoplasts throughout this dissertation as was used in previous research [1, 110]. Taking the period and the refractive index into account, we find that the iridoplast structure is analogous to a DBR with a period $\Delta = 168$ nm and with a Bragg reflection in the blue, around $\lambda = 480$ nm, reflecting up to 10%, as shown in figure 1.8 (d).

For the *Selaginella*, the specialised chloroplasts are much larger, around $13\mu m \times 20\mu m$, and consist of two distinct parts: a structured one, similar to the iridoplast, and a non-structured one, similar to a standard chloroplast. The term bizonoplast was coined due to the presence of these two distinct zones [112], shown in figures 1.8 (e) and (f). Because of the distinct structures, bizonoplasts are also much deeper than iridoplasts [113, 114]. As a consequence of the well-ordered multilayered top structure, bizonoplasts present similar

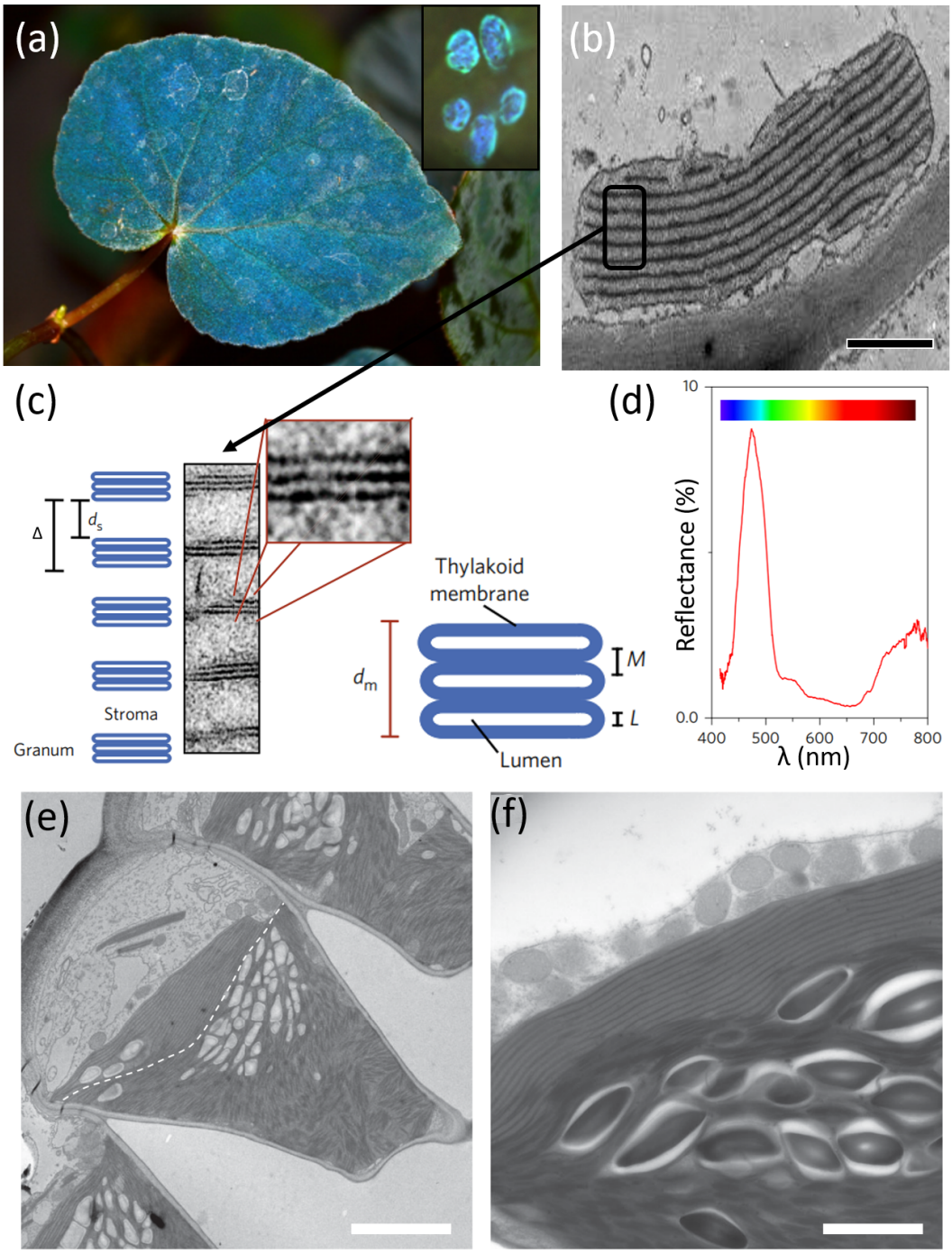


Figure 1.8: **Photosynthetic photonic structures**. (a) Photograph of a *Begonia pavonina* leaf which looks blue due to the presence of numerous iridoplasts seen in the inset under an Epi-illumination (reflectance) optical microscope. (b) SEM image of a cross-section of an iridoplast; the scale bar is 1 μm. (c) Schematic of the nanostructure of iridoplasts representing the SEM close-up image. (d) The reflectance of an iridoplast under normal light incidence. Extracted from [1]. (e) TEM image of the cross-section of a bizonoplast in *Selaginella erythropus*. The white dashed line separates the structured and non-structured zones of the organism; the scale bar is 5 µm. (f) Close-up of the previous subfigure showing the layered structure. The scale bar is 0.5 µm. Extracted from [111].

USC UNIVERSIDADE DE SANTIAGO

optical properties to the iridoplast [111]. We note that, unlike non-structured chloroplasts, iridoplasts and bizonoplasts are found in the epidermal cells of the leaves, i.e. on the surface, which makes them easily observable by the naked eye.

The presence of iridoplasts is widespread among different *Begonia* species. Many present blue iridescence [1, 115] but there are other species where the Bragg reflection is centred around the green wavelengths and, for that reason, they might have a different biological function [115, 116]. In fact, the species with green iridoplasts tend to grow in sub-Saharan Africa where the light conditions could be different [117]. Because of their green colour, their iridescence is not clear under the naked eye. For that reason the authors in reference [116] erroneously claim that green iridoplasts do not present iridescence, suggesting therefore a new name. However, naked eye observations cannot be used to extract decisive conclusions since the angular dependence can't be precisely observed. In fact, Hugh Perryman, using suitable equipment, demonstrated that these green iridoplasts presented structural iridescence [117]. However, green iridoplasts are beyond the scope of this work and we'll focus only on the blue ones.

Despite much research on the optical properties and arrangement, the biological advantage of structured chloroplasts has remained unknown, though it had been speculated that it could serve as a cue for pollinators [118–120], have a photo-protective role, an anti-herbivory effect, or it could play a direct part in photosynthesis [121]. Perplexingly, the plant species that present these structured chloroplasts are all found under the forest canopy where light intensity is much lower and, importantly, the quality of light (i.e. the wavelengths) is highly variable [29]. Because of the low intensity of photons, this state, is known as low light or dark conditions; expectedly, we call high light conditions the state with abundant light. This means that these photosynthetic organisms are reflecting part of what little light reaches them which seemingly looks like a big downside. For this reason, a thorough look into the photonic properties of the structure was needed.

The slow light properties of iridoplasts were theoretically investigated by Jacobs et al. in 2016 [1]. Iridoplasts were shown to enhance light absorption in the green ($\lambda \sim 520$ nm), up to $\gamma \sim 1,25$, whilst reducing absorption in the blue ($\lambda \sim 470$ nm), $\gamma \sim 0.7$, due to the presence of the photonic band gap, as shown at the top of figure 1.9 (a). Note that the non-structured system used to calculate this factor from equation 1.13, was created by setting the stromal distance between grana to zero, whilst maintaining everything else constant. The enhancement or decrease of the light absorption can also be viewed as a consequence of the enhancement or reduction of the local density of states within the structure at the mentioned wavelengths [122]. Looking at figure 1.2 (b), it might still seem that iridoplasts are counter-productive since the strongly absorbed wavelengths are being reflected away whilst enhancing the capture of wavelengths with very little absorbance. However, light under the forest canopy, where *Begonias* are found, is highly attenuated and the intensity of blue light is strongly reduced. On the other hand, green wavelengths are relatively more abundant than blue ones (roughly 5 times) since leaves tend to reflect and scatter these away as a consequence of the very small absorption coefficient within this range for the major photosynthetic pigments. The availability of light wavelength matches the absorption enhancement, as is shown in figure 1.9 (a). Therefore, it is expected that iridoplasts can enhance light capture under the natural environment that *Begonias* are found [1]. This has recently served as an inspiration to create artificial PhC to enhance light absorption by slow light and increase photosynthetic activity in algae [123].

USC UNIVERSIDADE

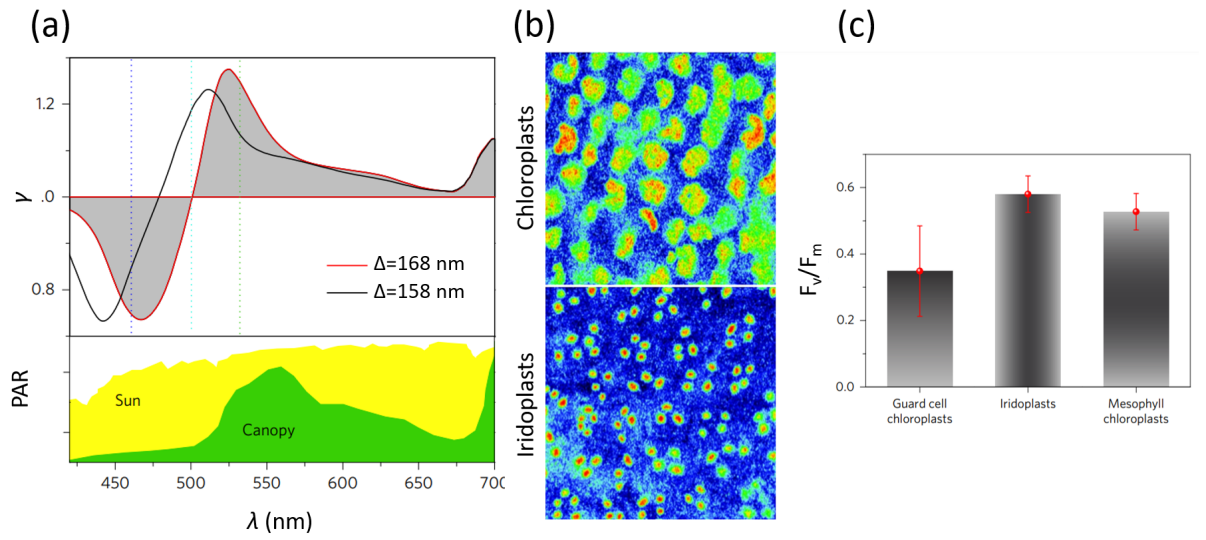


Figure 1.9: **Absorption enhancement and Photoluminescence measurements of iridoplasts**. (a) Top: Absorption enhancement factor (γ) of iridoplasts under two different periods (Δ). Bottom: normalised Photosynthetic Active Radiation (PAR) under direct sunlight and under the forest canopy (where *Begonias* are found). (b) Fluorescence images of the chlorophyll in chloroplasts (top) and iridoplasts (bottom). (c) Maximum quantum yield (F_v/F_m), with measurement's standard deviation, of PSII for guard cell chloroplasts, iridoplasts and mesophyll chloroplasts. Extracted from [1].

In addition to the slow light effects, the maximum potential quantum efficiency of the PSII (F_v/F_m) in the structured and non-structured chloroplasts was experimentally compared. Quantum efficiency is defined as the ratio between converted photons and absorbed photons. This is found by measuring the fluorescence of the PSII in the chlorophyll under a variable light condition (F_v), observed in figure 1.9 (b). This is then compared to the maximum potential fluorescence of these systems (F_m) which occurs when they're saturated by light. Therefore, F_v/F_m measures the post-absorptive efficiency of a photosynthetic system under a particular light condition [124, 125]. Figure 1.9 (c) shows that iridoplasts have a 5-10 % higher quantum efficiency than non-structured mesophyll chloroplasts (those in the inner tissue of the leaf) and 60-70% higher quantum efficiency than the chloroplasts in guard cells (cells used to control gas exchange) [1]. However, we must stress that the results and conclusions presented in this section are valid only under low-light conditions. The effect of the dynamic morphological changes observed in the thylakoids of chloroplasts remains unexplored.

1.3.2 Thylakoid dynamics under different light conditions

The photonic properties of iridoplasts have been observed to be highly dependent on the light intensity state. Under low light conditions, iridoplasts present the photonic properties that have been discussed above. However, within minutes of high light exposure, iridoplasts respond by switching off these properties, losing their characteristic blue reflectance. The mechanism underlying these changes and their biological advantages remains unknown and unexplored. Nevertheless, it is hypothesised that light-dependent structural changes of iri-

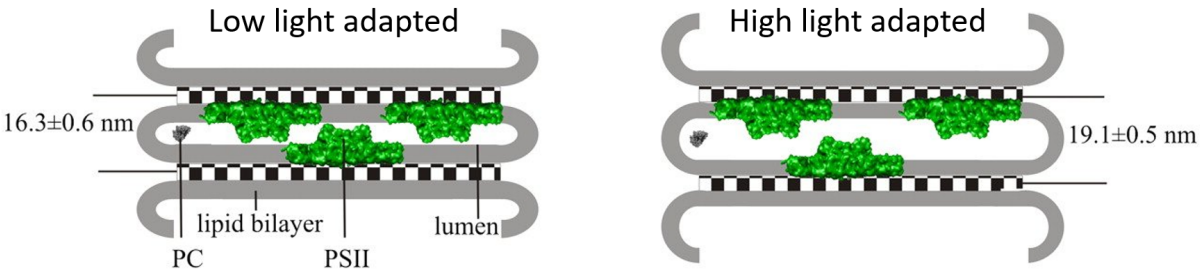


Figure 1.10: **Thylakoid light response**. Low and high light-adapted thylakoids of a standard chloroplast. Extracted from reference [126].

doplasts might be responsible for this [1]. However, there haven't been extensive studies to date on these changes for iridoplast. Detailed studies on the morphological response of non-structured chloroplasts to different light conditions were first investigated recently by Kirchhoff who found that the thylakoids, and hence the whole grana, expand from low to high light [126], demonstrated in figure 1.10. In addition, the stroma of blue iridoplasts is known to also expand under high light conditions [116]. We note that the mechanism responsible for these expansions remains unknown.

The biological advantage of the thylakoid expansion in standard chloroplasts is hypothesised to be the increase in protein diffusion [126] and cyclic electron transfer [127]. In addition, it has been speculated that the expansion results in the physical detachment of clusters of antennae and reaction centres. The light captured by the detached antenna clusters cannot be transported to PSII and PSI and gets quenched away [128, 129]. If we consider that, in addition to the observed stroma expansion, this grana expansion occurs for iridoplasts, the potential biological advantages of an expanded photonic system would be, in addition to the previously mentioned ones for standard chloroplasts, the ability to respond to the light environment by absorbing less under high light conditions by switching off slow light effects.

Compared to non-structured chloroplasts, iridoplasts seem to be biologically advantageous in two ways: they enhance the overall absorption of the available light and they enhance quantum efficiency by 5-10%. This work suggested that iridoplasts have adapted their structure to attenuated light conditions in order to take better advantage of the available wavelengths. Additionally, iridoplasts seem to be responsive to light-intensity conditions to control light absorption. Despite this, research on these structures remains meagre: slow light effects have only been briefly theoretically investigated, with many aspects still lacking scrutiny. Moreover, due to the complexity of the biological system, absorption has not yet been directly measured. For this reason, a biomimetic system can be used as a playground to investigate indirectly iridoplasts. Crucially, to create both the mimetic system and a theoretical framework to study iridoplasts, an accurate representation of the refractive index of the constituents of the biological system is required. Importantly, this representation has to include not only the real component of the refractive index ($\bar{n}$) but also the imaginary component ($\tilde{k}$) to take into account the absorption of the photosynthetic pigments. Theoretically, one can use the refractive index calculated indirectly from the literature for chloroplasts [109]. Experimentally however, there are no materials with the same refractive index as the biological system, so a dye with similar optical properties has to be used.

1.4 TDBC as a biomimetic pigment

Molecular aggregates are chains of molecules bound together by intermolecular non-covalent interactions. The aggregation creates distinct optical properties from the non-aggregated molecules called monomers. As monomers, these molecules present the standard dye behaviour: they absorb a wide spectrum of light, centred at a particular wavelength, and then re-emit this light as fluorescence at longer wavelengths (top of figure 1.11). The difference between the absorption wavelength peak and the fluorescence wavelength peak is known as the Stokes' shift. Aggregates are typically divided into two main categories, depending on how they aggregate and consequently how their optical properties change: J-aggregates and H-aggregates. In the former, the aggregation of the molecules proceeds via $\pi - \pi$ interactions of the orbitals, demonstrating properties of molecular ensembles, acting as a single unit with an increased dipole moment. Consequently, when excited, the electron-hole pair of the aggregate becomes delocalised. Despite this, the distance between the electron and the hole remains small compared to the ones found in, for example, crystals; they are, therefore, still considered Frenkel excitons. This is shown in the redshift and the narrowing of the molecular excitation of the energy levels, corresponding to its absorption peak, creating a resonance. Throughout this thesis, we will interchangeably name this absorption narrow peak as exciton or resonance.

J-aggregates were first observed in 1936 by Jelley [130] (where the name is derived from) and Scheibe [131] independently. In contrast, in H-aggregates the aggregation is formed by the side-by-side sandwich association with crossed dipoles and causes a hypsochromically (which gives it the name) shift, i.e. a blueshift. Nonetheless, the corresponding fluorescence spectrum is redshifted relative to its absorption [132]. These optical properties are summarised schematically in figure 1.11. This is however a simplification, and there are some intermediate scenarios where H- and J-bands or several J-bands can be observed in the same molecule [133].

A particular property of J-aggregates is their small Stokes' shift (< 5 nm), a consequence of the localisation of their energy levels. This means that the absorption and subsequent emission spectra will be centred around similar wavelengths. Consequently, a considerable overlap between the emission and absorption energy levels is observed. Moreover, the small dipole moment of the exciton means that it interacts very little with the medium. Consequently, the excitonic wave packet is highly coherent allowing for efficient and fast exciton energy transfer between molecules. Being able to collect and transfer energy, they can be useful as models to study photosynthesis [134]. For this reason, J-aggregates are considered to be biomimetic to the natural photosynthetic pigments responsible for the exciton energy transfer [135–139] and hence we'll focus only on this aggregate to mimic the biological system.

J-aggregates are usually found in chromophores such porphyrins [140], perylene bisimides [141], chlorins [142], and, importantly for this work, cyanine dyes [134] (systems conjugated by two nitrogen atoms). Cyanine dyes have been known to exist before J-aggregates were studied [143] and they present several advantages over other possibilities: they can self-assemble in water, allowing for better processability, they have stronger structural stability, stronger intermolecular coupling [144], and can present their narrow absorption peak within a broad spectrum range [133, 145]. Efficient energy transfer has also been shown to occur between different cyanine dyes [146]. Out of the many cyanine dyes, to create an experimental

USC UNIVERSIDAD DE SANTIAGO

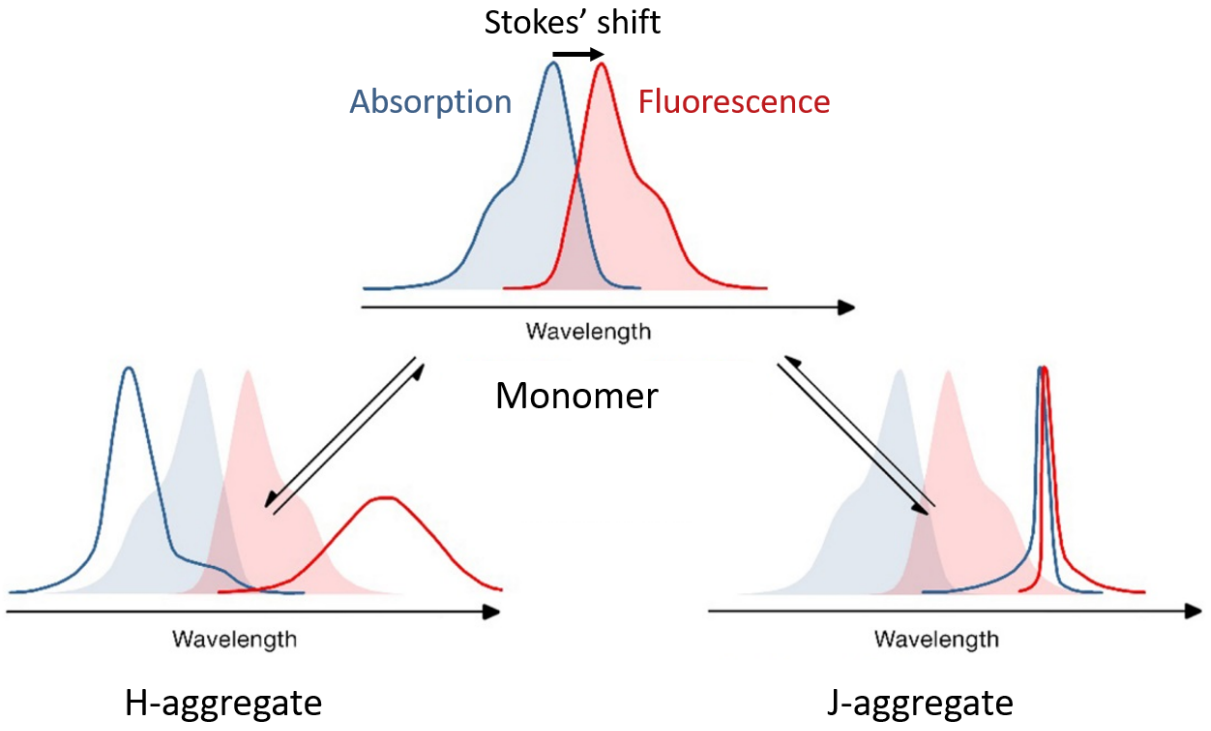


Figure 1.11: **Schematic of the J- and H- aggregate main properties**. On top, the optical properties (absorption and fluorescence) of aggregate dyes in their monomer form are shown. On the bottom, the shift of these properties is shown for H- and J-aggregates in red and blue lines. The shaded regions represent the properties of the monomer. Extracted from reference [133]

biomimetic structure of the iridoplast, we use a dye known as TDBC[1], due to its extraordinary processability, good optical characterisation in the literature, exciton energy in the VIS, and particularly strong dipole moment [147], yielding exotic photonic and optical properties described later, opening the door to further research and applications [148]. We note that, other artificial strategies have been used to mimic the photosynthetic light capture and energy transfer [149], such as supramolecular nanotubes [150], boron dipyrromethene dyes [151], and engineered DNA-protein supramolecular complexes [152]

As a monomer, TDBC presents the characteristics of a standard dye, with a wide absorption peak centred at $\lambda = 518$ nm. Despite it possessing better processability than other alternatives, to achieve high-quality layers with TDBC, a host polymer is still required. Typically, Poly(vinyl alcohol) (PVA) is used because, just like this dye, it dissolves in water and it is well-characterised in the literature [148]; to the combination of these two molecules, we call TDBC-PVA. The host polymer is a homogeneous material, meaning it has no absorption (and hence $\tilde{k} = 0$) within the VIS; it also has a quasi-constant real refractive index in the same range ($\tilde{n} = 1.51$). When an aqueous solution is created, under high enough concentrations, TDBC forms J-aggregates redshifting, narrowing, and strengthening the absorption peak to $\lambda = 590$ nm. In optics, the absorption of a material is described by the imaginary component

[1]TDBC: 5,6-dichloro-2-[[5,6-dichloro-1-ethyl-3-(4-sulphobutyl)-benzimidazol-2-ylidene]-propenyl]-1-ethyl-3-(4-sulphobutyl)-benzimidazolium hydroxide, sodium salt, inner salt.

of the refractive index ($\tilde{k}$). Changes in the imaginary part are accompanied by changes in the real part, according to the Kramers–Kronig relations [153, 154]. For the TDBC-PVA bulk material, the changes in the dielectric permittivity ($\epsilon = n^2$) caused by the strong resonance of the aggregate dye can be described by the Lorentz model:

$$\epsilon = \epsilon_\infty + \frac{f_0 \omega_r^2}{\omega_r^2 - \omega^2 - i\gamma_0 \omega}. \tag{1.14}$$

The left term of the equation, ϵ_∞ represents the permittivity of the host material (in our case PVA); at wavelengths far away from the exciton energy, the right term becomes negligible and hence $\epsilon \sim \epsilon_\infty$. The right term represents a strong resonance effect on our host polymer. ω is the working angular frequency, $\omega_r = 2.1$ eV gives the resonant frequency of the exciton (or alternatively $\lambda_r = 590$ nm for wavelength) where the absorption peak is centred, γ_0 is the damping rate, and f_0 is the Lorentz oscillator strength. This last term depends on the interaction between the electron-hole pair of the exciton. Note that, for convenience and simplicity, we wrote this equation in terms of permittivity and angular frequency, instead of refractive index and wavelength ($\lambda \propto \omega^{-1}$) such as in previous sections. Throughout this section, for the same reason, we'll continue using permittivity and frequency instead of refractive index and wavelength as before. Moreover, we'll also start using the linear momentum parallel to the surface (k) instead of angle.

In this thesis, we will follow the well-established fabrication method developed in reference [148], where the aqueous solution of TDBC-PVA is composed of equal parts of each, meaning that when deposited and dried we end up with a layer with 50% PVA and 50% TDBC. This results in $\epsilon_\infty = 2.37$, $\gamma_o = 10^{14}$ rad/s, and $f_0 = 0.4$. Plugging these numbers into equation 1.14, we obtain the refractive index shown in figure 1.12 (a) (bottom), where the effect of the increased absorption on the real part of the refractive index becomes clear. Under these excitonic strengths, the real permittivity gets so strongly attenuated that it becomes negative between $556\,nm < \lambda < 586\,nm$, as shown in the shaded region. The high oscillator strength and consequent negative permittivity are a result of the strong electron-hole pair interaction of the exciton. For this reason, under these conditions, TDBC-PVA presents metal-like optical properties within this range [155], providing strong reflectance (top plot) and a metallic look to the naked eye (inset). This creates a situation where strong absorption and strong reflectance are observed within the same range (top plot) caused by the imaginary and the real component of the permittivity, respectively.

The oscillator strength (f_0) depends on how strongly the dye aggregates and is key to the optical properties of the absorptive material because the intensity of the imaginary component is proportional to it, as suggested by figure 1.12 (b). As a consequence, the absorptive material will only start having metal-like properties for $f_0 > 0.15$, figure 1.12 (c). This region then continues to expand to lower energies as the strength increases. To control the Lorentzian strength, the ratio between the host polymer and dye can be manipulated. For example, a higher ratio of PVA would reduce this strength, though the relationship between the ratio and the Lorentz strength f_0 is not trivial.

The processability and the efficient energy transfer of excitonic materials make them ideal materials to create dye-based solar cells since efficient exciton transfer has been the major hurdle for the development of these cells [156, 157]. Moreover, the metal-like properties of TDBC have been shown to produce optical nanoantennas [158] and Optical Tamm states [159], making the organic dye a potential substitute for metals under certain circumstances.

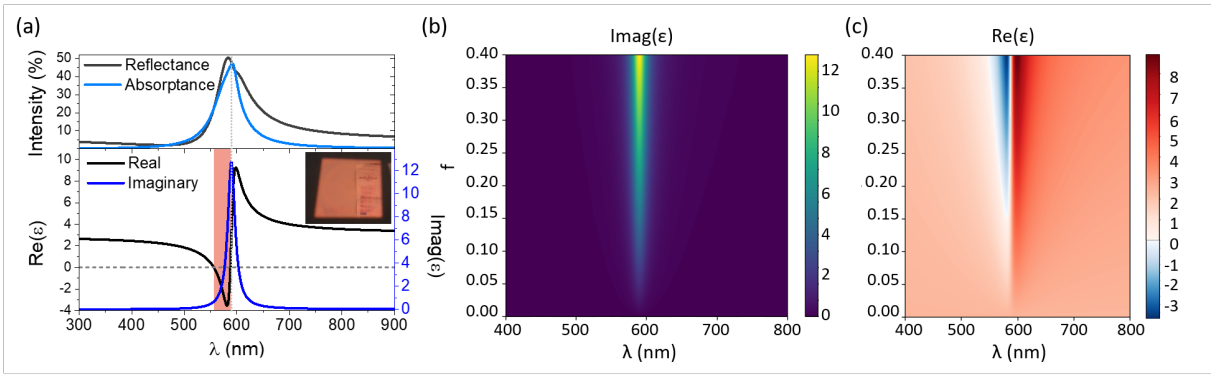


Figure 1.12: **TDBC-PVA optical properties**. (a) On top, simulations of the reflectance and absorption of a 50 nm thick TDBC-PVA layer. On the bottom, the real and imaginary permittivity of bulk TDBC-PVA. The shaded region represents the wavelengths at which the real permittivity is negative. Inset shows a photograph of a similar structure over a black background. The dotted vertical line gives the exciton of TDBC-PVA. Lorentzian strength (f_0) dependent (b) imaginary and (c) real components of the permittivity of TDBC-PVA.

1.4.1 Polaritonic properties of TDBC

In noble metals, the optical properties are caused by the free charge carriers. These carriers are typically electron plasma which does not allow light to propagate within the bulk material, thus reflecting it away. This property is demonstrated in the negative real permittivity of the materials. Assuming optically thick structures, this reflectivity occurs close to unity with negligible absorption by the metal for frequencies below the plasma frequency, ω_P. At higher frequencies, metals become transparent (up to several millimetres) and near this frequency, a strong absorption is observed. The plasma frequency gives the frequency of the plasma oscillations if thermal effects are ignored and it is typically found in the UV, meaning that metals, such as aluminium and silver, reflect almost all VIS light, making them excellent mirrors. Some metals, however, such as gold and copper, have this frequency in the visible, meaning they absorb part of VIS light, giving them their yellowish and pinkish colours respectively. Due to unmatched stability, gold is a particularly excellent candidate to study light-matter interactions [160].

The interaction between the surface plasma of noble metals and light has given rise to the field of Plasmonics due to the control and confinement of light at the subwavelength scale [63, 161]. Their sensitivity to the surrounding environment allows for numerous technological applications [162, 163], such as on-chip plasmonic circuits [164], optical devices [165, 166], light emission from nanoantennae [167], photodetectors [168], biosensing [169–171], and biomedical devices [172–174]. These applications rely on the strong coupling between the plasma of the metal and the incident light mode to originate a new quasi-state known as a Plasmon Polariton. This is achieved by light propagating along a metal/air surface, represented in figure 1.13 (a). Importantly, the interaction between the two modes can only exist in p-polarised light as suggested by the figure. Under strong coupling, anti-crossing is observed when both states are in resonance, forming an upper and a lower plasmon polariton, as represented in figure 1.13 (b). The difference in energy between the two is known as the Rabi splitting [175]. The upper polariton propagates in the bulk material whilst and the lower propagates along the metal/air interface, corresponding to the Surface Plasmon Polariton

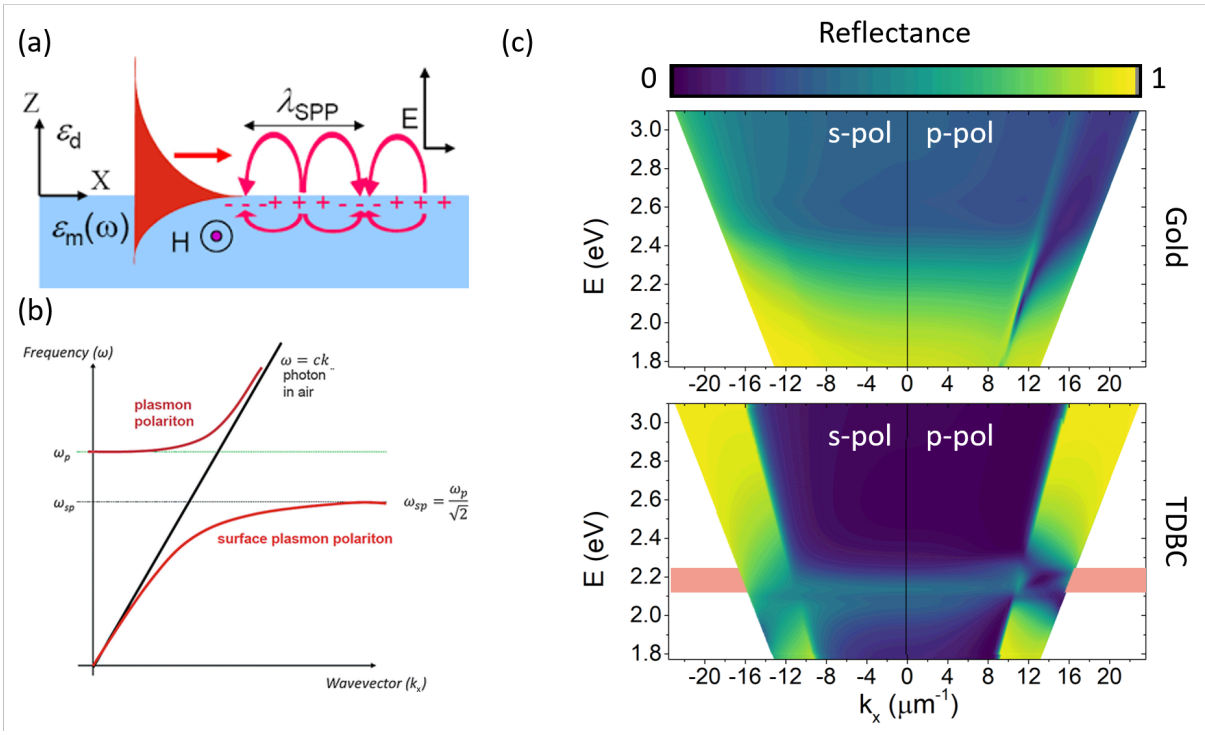


Figure 1.13: **Surface plasmon and exciton polariton**. (a) Plasma in metals interacting with light coupled to the surface along the x-axis, creating a SPP. This coupling exists only for TM (or H) light. Extracted from reference [181]. (b) Anti-crossing between the plasma frequency and the metal/air light line. Extracted from [182]. (c) Simulated momenta-dependent reflectance of a 50 nm layer of gold (top) and TDBC-PVA (bottom) to air for the different polarisations. Metallic-like region of TDBC-PVA caused by the negative permittivity is represented by the orange area.

(SPP) [176]. The upper branch bends towards the plasma frequency and the lower branch towards the surface plasma polariton frequency (ω_{SP}). It can be shown that, for the gold/air interface case, $\omega_{SP} = \omega_P/\sqrt{2}$. The inherent absorption of noble metals presents a major hurdle since it limits the length the mode can propagate. For that reason, alternative materials have been investigated for the production of plasmonic states, such as doped semiconductors [177], graphene [178, 179], and chalcogenides [180].

The dispersion relation of SPP can be obtained from solving Maxwell's equations and applying the right boundary conditions [176, 183]:

$$k = \frac{\omega}{c}\sqrt{\frac{\epsilon_1 + \epsilon_2}{\epsilon_1 \cdot \epsilon_2}}, \tag{1.15}$$

where ϵ_1 and ϵ_2 are the permittivity of dielectric material and the metal. This solution is observed in figure 1.13 (b). Experimentally, SPP are clearly observed in the momenta and energy-dependent reflectance because the coupling-induced light confinement creates a strong dip. Note that, to be able to strongly couple, the noble metal has to be thin enough, around 30 to 60 nm, to allow light to reach the metal/dielectric interface. The angle-dependent reflectance is observed in figure 1.13 (c) top, where both polarisations are shown for comparison. Below the plasma frequency (around 2.5 eV), we can see that gold

reflects most light for all momenta. This reflectance gets strongly reduced for higher energies since the metal becomes transparent. These effects make the light line unclear to distinguish when no photonic effect is observed in s-polarisation. However, for p-polarised light, the dip in reflectance caused by fulfilling the coupling conditions is quite evident beyond the air light line. Because this mode occurs only beyond this line, its observation requires techniques to couple to higher momenta, such as using a prism [184, 185], gratings [183, 186], or using oil immersion in reflection [187, 188]. The last technique is discussed in detail in section 2.3 and it will be often used throughout this work. For comparison, figure A.1 shows an angle reflectance measurement of a thin film using this technique, yielding a similar plot to the one at (c). Crucially, aside from the need for p-polarised light, the condition to satisfy this equation is that the real permittivity has to be negative. For that reason, surface polaritons may occur with alternative materials which do not have plasmons but satisfy this condition. Therefore, there is an entire zoo of different polaritons using many different states to achieve strong coupling with light [189].

Under the appropriate frequency range, TDBC has Frenkel electron-hole pairs which provide the negative permittivity condition necessary to obtain surface polaritons. In 2016, Gentile et al. theoretically and experimentally showed that, thanks to these properties, TDBC-PVA provides analogous hybrid states to the SPP for the optical metal-like range [148]. Instead of a plasma resonance, this material has an excitonic resonance, therefore the strongly coupled hybrid state is known as Surface Exciton Polariton (SEP). Figure 1.13 (c) shows the momenta and energy-dependent reflectance of the interface between a thin layer of TDBC-PVA and air. Far from the exciton, very low reflectance is observed ($\sim$ 5 to 10%) since we have a low contrast dielectric interface. The dye/air light line is easily identified at high momenta because reflectance goes to nearly 100% due to the total internal reflectance. In the resonant range, reflectance becomes much stronger because of the metal-like optical behaviour (at higher energies, orange region) and the higher refractive index contrast (at energies lower than the exciton). At the exciton (E = 2.10 eV) a dip in reflectance is observed, caused by the strong and narrow absorption. Absorption is responsible for the slightly lower reflectance beyond the light line, even outside the excitonic area. Under p-polarised light, the SEP is observed in a strong dip beyond the light line within the metal-like region.

The observation of this state showed that organic excitonic materials could present similar photonic properties and hence applications as metals, providing a substitute with better processability and lower financial and environmental costs. Interestingly, hybrid plasmon and exciton states (plexcitons) are also of great interest due to their promise to open up new possibilities for room-temperature quantum devices among other biomedical applications [190–201]. Very recently, a SPP and SEP hybrid has been theoretically studied, though its experimental observation remains to be shown [202].

1.5 Motivations and objectives

Above, we have introduced the background theory necessary to develop and understand the work presented in this dissertation. We've covered diverse topics within biology, physics, chemistry, and a mix between them, all of which are required to study iridoplasts. The research of these systems and their photonic properties in particular remain, to this day, extremely scarce. As mentioned above, theoretical and experimental studies remain super-

USC UNIVERSIDADE DE COMPOSTELA

ficial and their biological role continues to be an unproven hypothesis despite the direct connection between photosynthesis with the fundamental science of photonics.

Theoretically, two main research questions remain elusive regarding the effect of slow light and structural colour: the role of light-dependent morphological changes and the influence of natural disorder of the photonic crystal. Iridoplasts are known to reversibly switch on and off their structural colour under low and high light conditions [1], so one can reasonably hypothesise that this serves as a mechanism to control light absorption: absorbing more light under dark conditions and absorbing less when light is in excess. Note that, because excess light absorption creates an excess of redox molecules which damage the cells [32, 126, 127, 203], the light intensity adjustments provide biological advantages under both conditions. Even though natural PhC present highly periodic structures, the thickness and spacing between the layers aren't perfectly constant and hence their value has a degree of uncertainty [204, 205]. This makes the natural structures disordered which degrades their quality and hence their properties [60, 206, 207]. Therefore, it is expected that the lower quality of iridoplasts will present negative effects on slow light-induced light absorption enhancement. In addition, there are no theoretical studies of the slow light properties of bizonoplasts, despite the characterisation of their optical properties showing they potentially present similar biological roles to iridoplasts [111]. Other structural factors, such as the different number of grana and different periodicity, require consideration.

Experimentally, many biological points require further research to perform the theoretical analysis and understand the photonics properties of iridoplasts. In equation 1.5 for the Bragg reflection, there are two key components: the refractive index and the period of the structure. The refractive index of the thylakoid membranes, which is highly influenced by their chemical properties, remains unexplored. Even though the thylakoids in iridoplasts appear to have the same properties as the thylakoids in chloroplasts [1], a thorough study of these should be done to investigate any potential critical differences. Regarding the period of the PhC, short-term (minutes) light-dependent structural responses are known to expand the grana of standard chloroplasts [126]. However, for iridoplasts, few studies on the morphological light-dependent changes exist, despite the knowledge that they tune their structural colour. Reference [116] performed the structural analysis changes for a selected few *begonia* species iridoplasts, but here only the acclimation (1 week) changes of the stroma spacing are investigated. Interestingly, the long-term effect of growing *Begonias* under different quantities (i.e. intensity) and qualities (i.e. wavelengths) of light on the structure and the number of iridoplasts has been extensively studied, though its subsequent effect on slow light remains to be investigated [115].

Biological topics, however, are out of the scope of this thesis. Here we are concerned with answering the fundamental photonic question of iridoplasts. In particular, we want to make a direct observation of slow light-induced absorption enhancement. Due to the complexity of the biological system, a biomimetic structure is fabricated using the chemically relevant J-aggregate dyes discussed above, since these present similar excitonic properties. For processability reasons, structures containing TDBC cannot be made using typical inorganic techniques for two reasons. First, the UV radiation released from the sputtering and PECVD machines would destroy the chemical properties. Second, TDBC cannot be processed on its own and hence it is mixed with a polymer. To make polymer multilayered structures similar to iridoplasts, spin coating techniques are required (discussed in detail section 2.2) since they yield the most controllable and reliable polymer films [208]. We will

USC UNIVERSIDADE

use the biomimetic structure and the fabrication techniques developed to go beyond the initial biological questions and develop all-organic and high-quality photonic structures which could replace inorganic and metallic photonic systems that currently dominate the field of photonics but have a high financial and environmental cost.

So far we have been focusing on 1D PhC, meaning that we're assuming they're infinitely large in the plane perpendicular to the periodicity. This approximation is valid when this length is many times larger than the working wavelengths. Iridoplasts are roughly circular with a diameter of ~ 5 μm. Whether or not these dimensions are small enough such that iridoplasts present lateral light confinement within the structure remains unknown. This would make the photonic properties of the structure less dependent on the angle of the incident light [209, 210]. To study this, we can create 3D simulations of the optical properties or we can directly study the optical properties of the biomimetic structure with similar lateral dimensions.

In this work, we explore the thesis that dark-dwelling plants, such as *Begonias*, have developed highly specialised periodic chloroplasts to enhance light absorption through slow light properties. From here, we extend the techniques and materials developed to demonstrate that all-organic high-quality photonic structures with metal-like properties can be created. In particular, this dissertation is outlined:

- In chapter 2, we introduce the theoretical and experimental methods that serve as a base for the work presented here. They provide the tools to simulate the photonic properties of 1D PhC, the fabrication techniques of all-organic 1D PhC, and the experimental optical characterisation of the photonic structures.

- In chapter 3 we introduce a full theoretical paper where the effects of light-sensitive changes and the realistic disorder are investigated for iridoplasts and bizonoplasts.

- In chapter 4, we present a publication where an iridoplast biomimetic DBR with TDBC doped layers is developed.

- In chapter 5 we present the final paper where we use the spin coating techniques developed for the previous paper to fabricate the first all-organic structure showing an optical Tamm state.

- In chapter 6, we discuss the papers published as a part of this dissertation and comment on future work directions.

- In chapter 7 we present preliminary results of two 2D nanostructures containing TDBC.

- Finally, in the chapter 8, we conclude and summarise our findings. We also discuss future work.

USC UNIVERSIDADE DE SANTIAGO DE COMPOSTELA

CHAPTER 2

Methods

This chapter is divided into three sections. Section 2.1 develops the theoretical framework upon which numerical simulations were performed. These simulations are used throughout this work. In section 2.2, we demonstrate in detail the experimental technique used to fabricate high-quality all-organic 1D DBR by spin coating. Finally, in section 2.3 we present the Fourier image microscope set-up used throughout this work to measure the optical properties of photonic structures. We briefly explain the theory behind the oil immersion lens which is used to measure higher momenta than standard lens.

2.1 Transfer Matrix Method

In order to theoretically study the iridoplasts and to guide us through the fabrication of PhCs, a robust model capable of numerically calculating the photonic properties of a given structure is needed. Since for most of this work a 1D approach is taken, we can use the well-known and highly computationally efficient Transfer Matrix Method (TMM). Despite its popularity to simulate the optical response of structures, the TMM was first developed to model efficiently wave propagation for seismological applications [211]. In simple terms, the TMM takes into account the fact that, according to Maxwell's equations, light at one point can be related to another point through a matrix that considers each layer and interface of the 1D PhC [212]. In this section, we'll briefly describe the theory underlying this method used to build a *Python* model to simulate the photonic properties of multilayered structures.

Consider the multilayer dielectric system with N stacks given in figure 2.1. Here, we assume the initial medium and the final medium to be infinite and lossless. We can write the electric field for the different layers based on the Bloch solution to the wave equation mentioned above [41]:

$$E(x) = \begin{cases} A_0 e^{-ik_{0z}(z-z_0)} + B_0 e^{ik_{0z}(z-z_0)} \text{ if } z < z_0 \\ A_l e^{-ik_{lz}(z-z_l)} + B_l e^{ik_{lz}(z-z_l)} \text{ if } z_{l-1} < z < z_l \\ A_f e^{-ik_{fz}(z-z_f)} + B_f e^{ik_{fz}(z-z_f)} \text{ if } z > z_N \end{cases} \tag{2.1}$$

USC

A and B correspond to the amplitude of the outgoing (left to right) and incoming (right to left) propagating waves respectively. The subscript 0, l and f represent the initial, intermediate and final media. This model assumes an isotropic and homogeneous medium. Anisotropy can be included in the TMM, however, we will not be working with such media. Here, we

follow the generally accepted coordinate convention where the optical path, that is perpendicular to the layered system, is represented by z. Therefore, k_z is the wave vector in this axis given by:

$$k_{lz} = \sqrt{\left(\frac{2\pi n_l}{\lambda}\right)^2 - k^2} = \frac{2\pi n_l}{\lambda}\cos\theta_l, \;\; l = 0, 1, 2, 3..., N, f \tag{2.2}$$

where n_l and $\cos\theta_l$ are respectively the refractive indices and the angle of light with the normal at layer l. Taking into account the interaction at each interface of the system, we can describe the electric field amplitudes as:

$$\begin{pmatrix} A_0 \\ B_0 \end{pmatrix} = \mathscr{M}\begin{pmatrix} A_f \\ B_f \end{pmatrix}, \tag{2.3}$$

where $\mathscr{M}$ is the Transfer Matrix and it describes the propagation of the electric field from the initial to the final media. It is defined as:

$$\mathscr{M} = \begin{pmatrix} M_{11} & M_{12} \\ M_{12} & M_{22} \end{pmatrix} = D_0^{-1}\prod_{l=1}^{N}[D_l P_l D_l^{-1}]D_f. \tag{2.4}$$

D is known as the dynamic matrix and it describes the electric field transitioning from one medium to the next. P is the propagation matrix and it takes into account the propagation through the bulk media of each layer. We can see that the product operator takes into account the effect of all N layers on the electric field. These matrices are defined as:

$$D_l = \begin{cases} \begin{pmatrix} 1 & 1 \\ n_l\cos\theta_l & -n_l\cos\theta_l \end{pmatrix} & \text{for s waves} \\ \begin{pmatrix} \cos\theta_l & \cos\theta_l \\ n_l & -n_l \end{pmatrix} & \text{for p waves} \end{cases} \tag{2.5}$$

and

$$P_l = \begin{pmatrix} e^{ik_{lz}(z_l - z_{l-1})} & 0 \\ 0 & e^{-ik_{lz}(z_l - z_{l-1})} \end{pmatrix}$$

Note that the propagation matrix is independent of the polarisation of light, whilst the dynamic matrix depends on wave polarisation. It is worth noting the physical meaning of the exponent in the propagation matrix. Ignoring the imaginary number, it can be written as:

$$\phi = k_{lz}d_l = \frac{2\pi n_l}{\lambda}\cos\theta_l d_l, \tag{2.6}$$

where we have written $d_l = z_l - z_{l-1}$ for simplicity and it represents the thickness of the layer l. ϕ represents the phase gained by each layer and it is a key parameter to understanding the constructive and destructive wave interference in photonic structures.

From equation 2.3, it is straightforward to see that the reflectance (r) and transmission (t) coefficients are given by:

$$\begin{aligned} r &= \left(\frac{B_0}{A_0}\right)_{Bf=0} = \frac{M_{21}}{M_{11}} \\ t &= \left(\frac{A_f}{A_0}\right)_{Bf=0} = \frac{1}{M_{11}} \end{aligned} \tag{2.7}$$

USC UNIVERSIDADE DE SANTIAGO DE COMPOSTELA

From here, reflectance ($R(\lambda)$) and transmittance ($T(\lambda)$) are given by:

$$\begin{aligned} R &= |r|^2 = \left|\frac{M_{21}}{M_{11}}\right|^2 \\ T &= \frac{n_f \cos\theta_f}{n_0 \cos\theta_0}|t|^2 = \frac{n_f \cos\theta_f}{n_0 \cos\theta_0}\left|\frac{1}{M_{11}}\right|^2 \end{aligned} \tag{2.8}$$

Note that, for transmittance, a term is added to take into account the different momenta between the initial and final media. These equations can be solved numerically by simply computing $\mathscr{M}$ from equation 2.4. Analytically, these could be further simplified under specific conditions. For example, for a single interface layer, the Fresnel equations could be derived. Importantly, when at each layer of the system the phase gain is a quarter ($\phi = \pi/4$), we have a quarter wave-plate (the simplest design of a DBR) and equation 1.7 can be derived.

From the conservation of energy, we must have:

$$A(\lambda) + S(\lambda) + R(\lambda) + T(\lambda) = 1, \tag{2.9}$$

where A and S correspond to the absorption and the scattering, Absorption will only be non-zero when there are one or more layers in the structure with a non-zero imaginary component of the refractive index ($\tilde{k}$). We will assume negligible scattering throughout this work.

We can find that for a periodic multilayer where the unit cell is composed of layers 1 and 2 with period Λ, the Bloch wave number (K) of the Bloch wave is given by [41]:

$$K(k,\lambda) = 1\frac{1}{\Lambda}\arccos\frac{1}{2}(A+D), \tag{2.10}$$

where the coefficients are give by:

$$\begin{aligned} A_{TE} &= e^{i\phi_1}\left(\cos\phi_2 + \tfrac{1}{2}i\left(\tfrac{k_{2z}}{k_{1z}} + \tfrac{k_{1z}}{k_{2z}}\right)\sin\phi_2\right) \\ D_{TE} &= e^{-i\phi_1}\left(\cos\phi_2 - \tfrac{1}{2}i\left(\tfrac{k_{2z}}{k_{1z}} + \tfrac{k_{1z}}{k_{2z}}\right)\sin\phi_2\right) \\ A_{TM} &= e^{i\phi_1}\left(\cos\phi_2 + \tfrac{1}{2}i\left(\tfrac{n_1^2 k_{2z}}{n_2^2 k_{1z}} + \tfrac{n_2^2 k_{1z}}{n_1^2 k_{2z}}\right)\sin\phi_2\right) \\ D_{TM} &= e^{-i\phi_1}\left(\cos\phi_2 - \tfrac{1}{2}i\left(\tfrac{n_1^2 k_{2z}}{n_2^2 k_{1z}} + \tfrac{n_2^2 k_{1z}}{n_1^2 k_{2z}}\right)\sin\phi_2\right). \end{aligned} \tag{2.11}$$

Equation 2.10 presents an important result because it provides us with the behaviour of the wave function. When $|\frac{1}{2}(A+D)| < 1$, K is real and hence we have propagating Bloch waves. For $|\frac{1}{2}(A+D)| > 1$, K becomes imaginary and hence the Bloch waves become evanescent. These waves are, therefore, "forbidden" from propagating and this regime is known as the photonic band gap or stopband of the PhC. Predictably, $|\frac{1}{2}(A+D)| = 1$ corresponds to the edge of this regime where slow light effects are strongest.

For this thesis, a *Python* script was developed to calculate the reflectance, transmittance, and photonic band gaps of any 1D PhC for any wavelength-dependent complex refractive indices. It can calculate this for different angles of incidence at s- and p-polarised light. Additionally, it finds the electric and magnetic fields. The model was fully based on solving the method presented in this section.

USC UNIVERSIDADE DE SANTIAGO DE COMPOSTELA

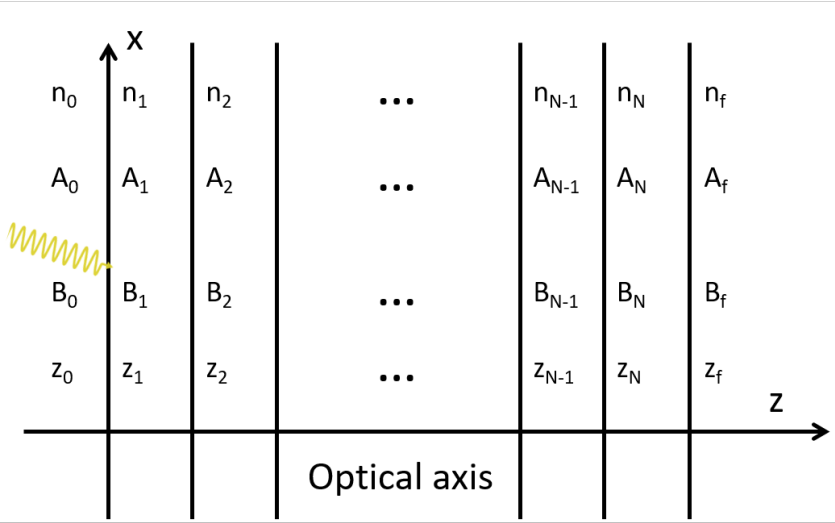


Figure 2.1: **Multilayer schematic**. Dielectric structure with N layers.

2.2 Spin coating for consistently high-quality DBRs

The deposition of thin layers of soft matter, such as polymers, on a substrate is widely used in a variety of topics. Depending on the objective, many coating techniques have been developed, such as spray [213], flow [214], and dip [215] coating. However, for nanometer-sized, the most uniform, and controllable layers, spin coating presents the most reliable technique [208]. In this section, we'll explain how spin coating was used to fabricate all-polymer DBRs with up to 100 layers.

Pioneered in reference [216], the technique uses the centrifugal force of a rotating disk to uniformly spread polymer diluted in a Newtonian fluid. The process typically consists of four steps, represented in figure 2.2:

- Deposition
- Spin-up
- Spin-off
- Evaporation

The apparatus used is known as a spin coater and it consists of a stage, where the substrate of the sample is on, typically attached by vacuum, see figure A.2. The process begins with the deposition of an excessive amount of polymeric solution onto the motionless stage. This is followed by the spin-up where the rotation of the stage starts to gradually increase up to $\sim 1000 - 8000$ RPM (Rotations per minute). Here, centrifugal force starts spreading the solution, whilst some evaporation occurs. When the solution is uniformly distributed along the substrate, the rotation is slowed down until it stops. Finally, we let the remaining solvent evaporate. An example of a spin-coated single-layer sample of TDBC-PVA is seen in the inset of figure 1.12.

The distribution of the polymer solution is a result of two main forces: the outwards centrifugal force caused by the rotation and the inwards friction strongly dependent on the

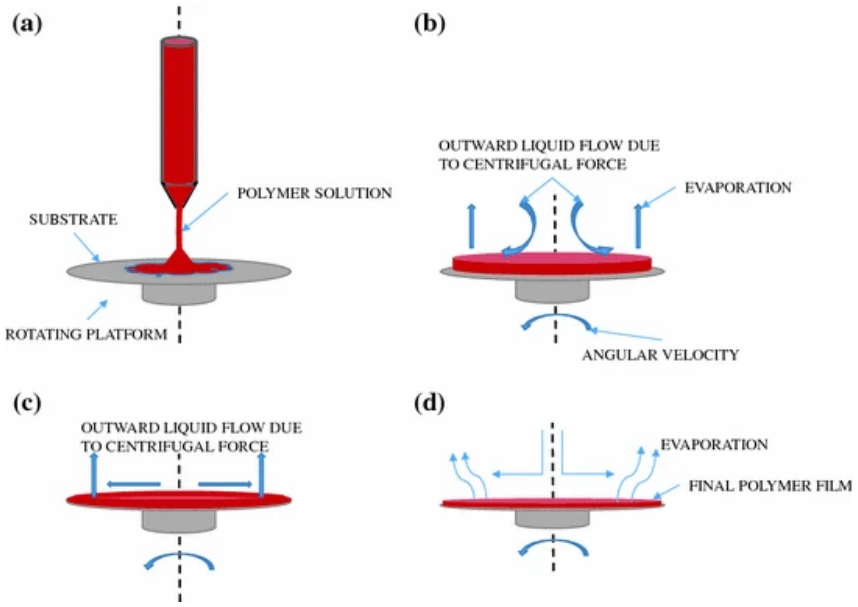


Figure 2.2: **Spin coating steps**. (a) Deposition of the polymeric solution. (b) Spin-up by initiating the rotation. (c) Spin-off, turning off the rotation when the polymer has been uniformly spread throughout the substrate thanks to the centrifugal force. (d) Evaporation of the solvent to dry the sample [217].

viscosity of the solution. For this reason, the two main parameters to control the thickness (h_{final}) of the final polymer layer are the RPM of the spin coater and the viscosity of the polymeric solution (directly affected by the concentration). An equation for this was derived by Meyerhofer [218], by assuming uniform evaporation of the solvent and using only the centrifugal force and linear shear force:

$$h_{final} = \left(1 - \frac{\rho_{A0}}{\rho_A}\right)\left(\frac{3\mu e}{2\rho_{A0}\omega^2}\right)^{1/3}, \tag{2.12}$$

where ω is the angular frequency, μ is the viscosity, e is the evaporation rate, ρ_A is the variable density of the volatile part of the solvent and ρ_{A0} is the initial density. Despite a large number of theoretical studies on the mechanics of spin coating [219–222], in practice, there are many unpredictable and uncontrollable parameters and hurdles which result both in the loss of accuracy and precision. For example, if we were to spin coat several samples under the same conditions, we would have an average final thickness significantly far from the value predicted from equation 2.12 (not accurate) and there would be a considerable standard deviation between them (not precise).

The substantial standard deviation results in the loss of quality of the PhC due to the disorder in the thicknesses of the individual layer, similar to what happens in natural photonic crystals. A particularly strong reason for this has to do with the dust impurities present on the underlying surface, causing the friction to vary and creating accumulation spots, if they're big enough. For this reason, a thoroughly clean substrate is required. In our case, the substrate is a microscope coverslip (for reasons which will become evident in chapter 2.3) and each was cleaned with a cotton bud soaked in, sequentially: water with soap, acetone and isopropanol. This was followed by 15 minutes of sonication in acetone followed by isopropanol. Despite

this treatment, the unpredictability of numerous factors in spin coating ultimately makes this an empirical technique where the thicknesses of the layers have to be calibrated, depending on concentration and frequency, by trial and error, and equation 2.12 is used only as a guide [218, 223, 224]. The unpredictability discussed here is distinctively harmful when making photonic structures since they are highly sensitive to very small thickness variations of the films.

To fabricate high-quality PhC, it is therefore critical to maintain every condition as stable as possible to decrease the standard deviation between the thickness of the layers and create consistent results. Typically, for the very thin layers required to produce photonic crystals (~ 100 nm), to achieve uniform films, deposition of the solution on a rotating stage is actually preferred to the conventional method [225]. Moreover, highly diluted solutions (since these present the least viscosity) and high RPM ($4000 - 8000$) are required. These two factors make it so that the evaporation process finishes before the rotation stops. This simplifies the spin coating to three steps only: spin-up, deposition, and spin-off, after waiting < 1 minute.

The two polymers used in this dissertation to make the multilayer stacks are Poly(vinyl alcohol) (PVA) and Polystyrene (PS) and we deposit them alternatingly to produce a photonic structure. As mentioned previously, PVA is the polymer used as a host for TDBC. We have therefore three materials to calibrate. These polymers were chosen for their processability, previous levels of characterisation, and because their solvents are of different polarisations. We dissolve PVA and TDBC in water, a polar solvent, and PS in toluene, an apolar solvent. This means neither solvent will significantly affect the underlying layer. Other important factors include the volume of the solution and the location of the deposition. During this work, due to the higher viscosity of PVA solutions and the hydrophobicity of the underlying layer, PVA and TDBC-PVA layers were registered to have worse uniformity than those of PS. The uniformity can be improved by increasing the volume of deposition. This is particularly important when PVA is doped with TDBC since it has a particularly low processability (compared to polymers). The volume of deposition used was 300 µL and 400 µL for PS and PVA containing solutions respectively. The location of deposition is important because the films produced are not perfectly uniform. In fact, the centre is the thickest and it then radially thins away. This is particularly obvious in all polymer DBR as we will see later. Moreover, in multilayers, this detail becomes crucial because the point of deposition becomes damaged after multiple layers. It is therefore desired to contain this damaged area to the smallest region by consistently depositing on the same spot.

To measure the thicknesses of the fabricated polymer layers, we use ellipsometry [226] which requires knowing the refractive index of the material [1], shown in part III of this dissertation. However, ellipsometry models with strongly dispersive materials were not providing accurate results. For this reason, for TDBC-PVA films, the thickness was calibrated using a profilometer. In fact, the refractive index of these layers had to be measured by an outside collaborator, professor Rosalia Serna (IO-CSIC, Madrid), with strong expertise in this field, see chapter 4. As mentioned previously, one of the most important factors is the friction caused by the viscous solution and the surface. Because we are fabricating multilayers, the underlying surface of PS will be PVA or TDBC-PVA and vice-versa, the calibration has to be

[1] Note that, we measured the refractive index in-house. To measure the refractive index of a polymer, the thickness of the film is needed. To break this chicken and the egg problem, we first measured the thickness of a sample with an Atomic Force Microscope to obtain accurate values and then input them into the ellipsometry models to derive the refractive index.

USC DE SANTIAGO

done accordingly. The only exception is the very first layer which is PS, since the refractive index of PVA and glass is very similar.

Using several solution concentrations, we found the ideal conditions to work with. PS (Aldrich PS $M_w = 192$ kDa) and PVA (Aldrich PVA $M_w = 33$ kDa) thin films were deposited under a varying wt% concentration depending on the desired thickness. Figure 2.3 (a) to (c) shows the calibration curves for these polymers. For PS single films on glass, an outstanding curve is obtained with an extremely small error (~ 3 nm for many points) and a consistent decrease with higher RPM. For PVA on top of PS, the points become more dispersed and the curves more irregular. PS on PVA shows small errors and consistent results, suggesting that PS provides more predictable results.

For TDBC-PVA films, a water solution of TDBC and PVA was produced by mixing at a ratio of, respectively, 3:1 a 2% wt TDBC water solution and a 6.0% wt PVA (Aldrich PVA $M_w = 85$ to 124 kDa) water solution, following the protocol in reference [148]. Further dilution of this solution was done with water in a 3:1 ratio (3 parts solution and 1 part water) to provide thinner layers. The final solution was mixed thoroughly to ensure homogeneity. For TDBC-PVA, the dye presents poor processing properties which makes the surface highly irregular. Compounded with the fact that the ellipsometry couldn't be used for calibration, means that controlling the thickness was much less precise. Consequently, since calibrating the PS thickness on top of TDBC-PVA required knowing the underlying thickness of TDBC-PVA and the use of a profilometer, the PS on TDBC-PVA calibration also presented poor precision. This is suggested in (d) and (e) by the significant value of the error bars. To overcome these hurdles, we deposit TDBC-PVA solutions under constant conditions to yield consistent thickness. We then vary the conditions of PS to control the period of the PhC. Moreover, we use the calibration of PS on PVA when making multilayers of PS and TDBC-PVA.

To study the slow light properties of the biomimetic structure, a reference system is needed, according to equation 1.13. This corresponds to a slab of TDBC-PVA with a well-defined thickness equal to the total absorptive material in the PhC being studied. However, it is not possible to spin coat TDBC-PVA on top of itself because the polymeric solution will interact with the underlying film and damage it. For that reason, to achieve the same thickness, we use a buffer layer of PS between each TDBC-PVA film to not have to deposit TDBC-PVA directly on top of another layer of the same material. This buffer has to be thin enough that it creates negligible photonic properties on the final structure. Subfigure (f) shows a calibration curve of PS at 6000 RPM under different weight percentage concentrations. Ideally, we would want this thickness to be as thin as possible. However, in practice, when this buffer layer had a thickness lower than ~ 25 nm, the samples presented clear signs of damage, even by the naked eye. We believe this is caused by small areas where the PS buffer layer was not covering the underlying layer.

Calibration curves were performed on samples with 1 to 3 layers: PS, PVA, PS. In this work, we are interested in producing photonic multilayers with up to 100 layers. Under the increased number of layers, new uncertainties are introduced to the process which creates a significant variation in the thickness of the different individual layers compared to the calibration. For that reason, even though indispensable, these plots end up being used only as a guide for the fabrication of 1D polymeric PhC. That is why many points do not present more than 4 measurements. Nonetheless, the desired photonic structure can be achieved if we follow this calibration curve because the thickness radially decreases from the centre.

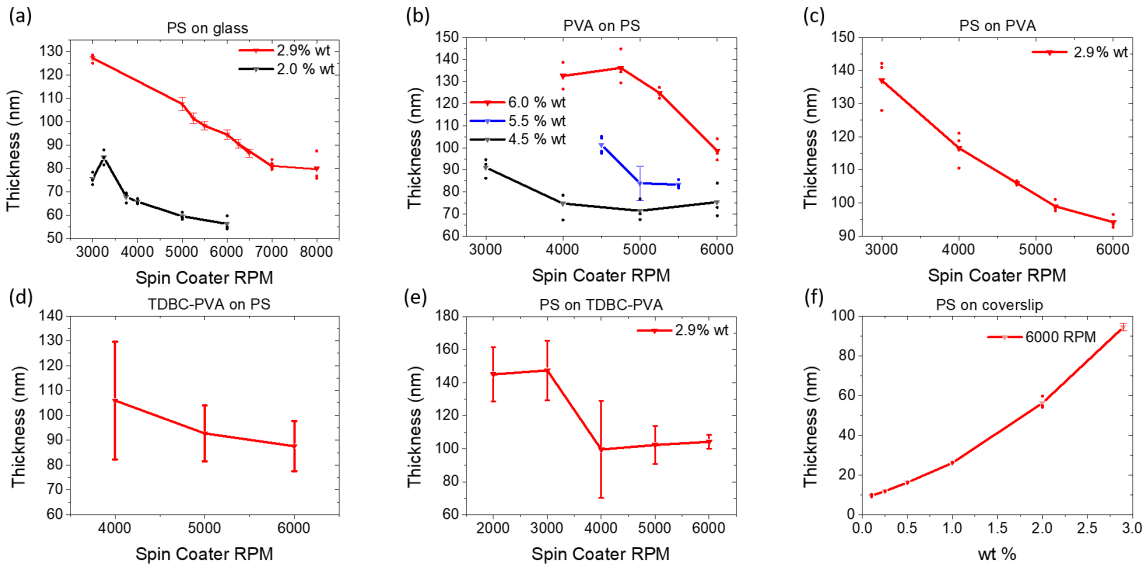


Figure 2.3: **Spin coating calibration curves**. (a), (b), (c): calibration curve of Polystyrene and Poly(vinyl alcohol) polymer solution under different weight percentage concentrations and on different surfaces. (d) and (e): TDBC-PVA and Polystyrene calibration on top of one another. TDBC-PVA solution as explained in the manuscript. (f) Polystyrene calibration curve for a fixed frequency and varying weight percentage concentrations. Error bars represent the standard deviation of all the samples measured at a specific condition. If the number of samples used to calibrate per point is smaller than 5, instead of the standard deviation, the different individual points are shown.

USC UNIVERSIDADE DE SANTIAGO DE COMPOSTELA

This means that, in each sample, we have a relatively large Bragg wavelength range (from 30 to 40 nm) that likely includes our desired goal if we follow the calibration curves. To demonstrate this and the whole spin coating process, we fabricated a 100-layer DBR with the following conditions: 6500 RPM of 2.9% wt PS solution on the substrate, followed by 5000 RPM 5.5% wt of PVA solution, followed by 6000 RPM of 2.9% wt PS solution. The last two steps are repeated until 100 layers are reached. Between layers, we do not leave the sample in a hot plate to dry faster, as is commonly done in the literature. We let it dry under ambient temperature to avoid damage to the surface caused by boiling the solvent, demonstrated in figure A.3.

Figure 2.4 shows the analysis of this sample. In subfigure (a), the normal incidence Bragg wavelength of this sample is shown at different Cartesian points. The red area around $x = y = 10$ mm represents the spot where the polymer solution was deposited. From there, reflectance radially becomes bluer. From subfigure (b), this region shows as well lower absolute reflectance (< 60%) due to the damage caused by the deposition process. Away from this deposition point, we obtain consistently a reflectance above 85%, reaching values up to 96%, which shows the extremely good quality of these structures outside the deposition area. Note, however, that the silver mirror reference doesn't yield a 100% reflectance. In spin-coated samples, the edges accumulate polymer that is pushed by centrifugal force. Moreover, when picking up the samples with tweezers, the edges are usually damaged. For these reasons, the reflectance measurements were done only at 5 mm away from the edges, which is why much of the measurements remain blank. Subfigure (c) shows the angle-resolved measurement of a point of the sample. This shows the typical blue shift in reflection with angle, similar to what was shown in figure 1.3. For clarity, the cross sections at normal incidence and at 45°represented by the vertical dashed red and blue lines respectively, are plotted in subfigure (d). Subfigures (e) and (f) show a photograph of the fabricated sample under a dark background at different angles.

This is only one of the many Bragg mirrors produced throughout this work. It shows that spin coating can be used for the fabrication of high-quality 1D PhC with strong photonic properties and hence it can potentially replace the financially and environmentally costly inorganic structures under some circumstances. The first instance of an all-polymer DBR is from 1979, where the authors used the same polymers as in this thesis: PVA and PS [227]. Here, despite having 200 layers, the authors did not reach stronger photonic effects than the ones shown in figure 2.4. By compressing the structure, a change in the Bragg wavelength could be measured, effectively acting as a pressure sensor. Further studies on all-polymer structures continued only a long time after [228–230], though their photonic strength remained low. In reference [230], the authors used two polymers that both diluted in apolar solvents. To avoid damaging the underlying surface, they crosslinked every layer before the following deposition. Though effective, this is extremely time-consuming and impractical. Recently spin-coated multilayered structures with strong photonic properties were fabricated onto flexible substrates made of PDMS [231–233]. This flexibility is suitable for applications where this is desired, such as for wearables [234] or flexible lasers [235], and to tune the colour by simply stretching the sample, which causes the layers to become thinner and hence to blueshift reflection [236, 237]. The tunability by stretching opens the doors to many other applications such as controlling λ cavity modes [236] and the Q-switching of an organic laser [238].

All-organic spin-coated samples are examples of soft photonics [239–241], where (mostly)

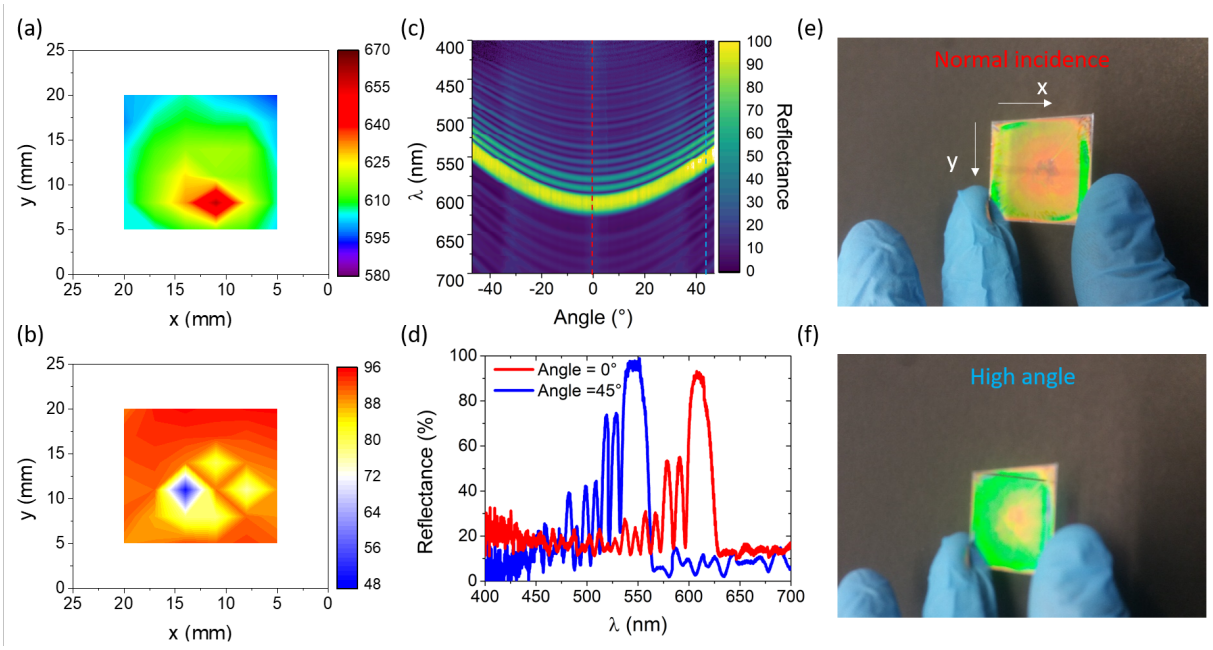


Figure 2.4: **All polymer DBR**. Normal incidence (a) Bragg wavelength (nm) and (b) absolute reflectance (%). The axes represent the Cartesian coordinates (x and y) of the sample measured. Points closer than 5 mm from the border (i.e. $5 > x, y > 20$) were not measured, explaining the white space. There are, in total, 25 points measured in these plots. (c) S-polarised angle-dependent reflectance (%) measurement of one point of the sample. (d) Cross section of the previous along wavelength plot at normal incidence and at a higher angle. (e) and (f) are photographs of the sample measured at normal incidence and at a high angle. White x and y arrows represent the Cartesian coordinates used in (a) and (b).

polymers are used to fabricate PhC. One major hurdle in this field is that large refractive index ($\Delta > 0.2$) contrasts between two different polymers are not possible to achieve. For that reason, doping the polymers has been done to increase the refractive index and consequently enhance the contrast. TiO_2 has successfully increased the refractive index of PDMS by ~ 0.4, albeit at the cost of processability of the polymeric layer [242]. Alternatively, porous inorganic multilayers have been infiltrated with a polymer to obtain a Bragg mirror with both flexibility and strong refractive index contrasts. However, this technique still relies on vapour deposition for the inorganic layers [243–246]. More recently, doping polymers with dyes has been suggested since, according to Kramers-Kronig relations, the increase in the imaginary component ($\bar{k}$) of the refractive index will increase the real component [247, 248]. However, the dyes used present a broad absorption band, causing absorption to attenuate the photonic properties of the structures. In this work, a similar approach is taken, though using J-aggregates, which confines the absorption to a much more narrow range.

2.3 Fourier image spectroscopy

USC UNIVERSIDADE DE SANTIAGO DE COMPOSTELA

The optical characterisation of photonic structures is key to studying their properties and structural quality. For systems with negligible scattering, measuring transmittance alongside

reflectance will allow one to infer the absorption of the system. Typically, the reflected/-transmitted light is coupled to a fibre connected to a spectrometer which reads the light wavelength spectrum (i.e. the number of photons for a certain energy range). Importantly, the angle-dependent features are required to obtain a complete characterisation. To achieve this, it is common to mount the samples on a rotating stage that allows the selection of the angle of incidence of light. This has been particularly the case for biological PhC [249, 250]. There are several limitations to this technique. Rotating the sample will physically move it away from the light spot, making it impractical to measure exactly on the same spot again. Moreover, the size of the spot measured has to be considerably large ($\sim$ 1 mm in diameter) to have the objective lens far enough to allow the rotation of the sample [251], despite creative approaches to reduce it [252]. This is particularly important for samples, such as iridoplasts or diatoms, which require extremely small areas to measure ($<$ 5 μm) [1, 99]. For these reasons, a system which does not rely on the movement of the sample or the lens is necessary. Therefore, for an accurate momentum space resolved investigation, more complex substitutes have been proposed, such as the phase-sensitive near-field optical microscopy [253, 254], the momentum-space imaging spectroscopy[2] [255], or, more commonly, the optical Fourier Transform (FT) imaging method [1, 99, 167, 256–258]. In this work, we will be using this last method to analyse photonic structures. In this section, we will use geometric ray tracing, due to its simplicity, to describe the propagation of light in the Fourier microscope spectroscopy technique.

2.3.1 Basic principles

Light propagating in free space can be described by a propagating wavefront decomposable by the 3D spatial vectorial fields. Assuming an isotropic medium, each direction can be treated independently: X, Y, and Z. By convention, X and Y are lateral and Z corresponds to the direction along the optical axis. When this wavefront goes through on a thin lens with focal length f, it will focus at this distance f from the lens, ignoring light aberrations. Depending on the angle of incidence with the perpendicular of the lens (θ), this point will be along the focal plane, as represented in figure 2.5 (a). This means that, depending on the location in the focal plane, we can determine the angle of incidence. For the complex wavefront system, an intensity pattern throughout this plane will be formed which encodes the information about the momentum (or equivalently the angles) of the incident light. Our goal is to use this principle in reflection to extract the photonic properties of PhC.

Equivalently, in reflection, instead of the focal plane, we extract the information of the Back Focal Plane (BFP) where the image is formed on the side of the lens. Consider the simple schematic in figure 2.5 (b) where an incoming collimated beam (solid black lines) goes through an objective lens and is reflected by a mirror at the focal distance. The reflected light (dashed grey lines) makes the same angle with the optical axis that's perpendicular to the lens (θ). This means that normal incident light goes back through the same axis. Once the light "reenters" the lens, it becomes again collimated. We can describe mathematically the transformation from the point on the mirror to the BFP as a Fourier transform [259], where the point-like real image, in real space, is transformed into the Fourier image plane, in k-space. In this plane, each angle of incidence (θ_1 and θ_2) will correspond to a specific distance

USC UNIVERSIDADE DE SANTIAGO DE COMPOSTELA

[2] The momentum-space imaging spectroscopy is based on the FT imaging method. One of the advantages is the capture of the phase response.

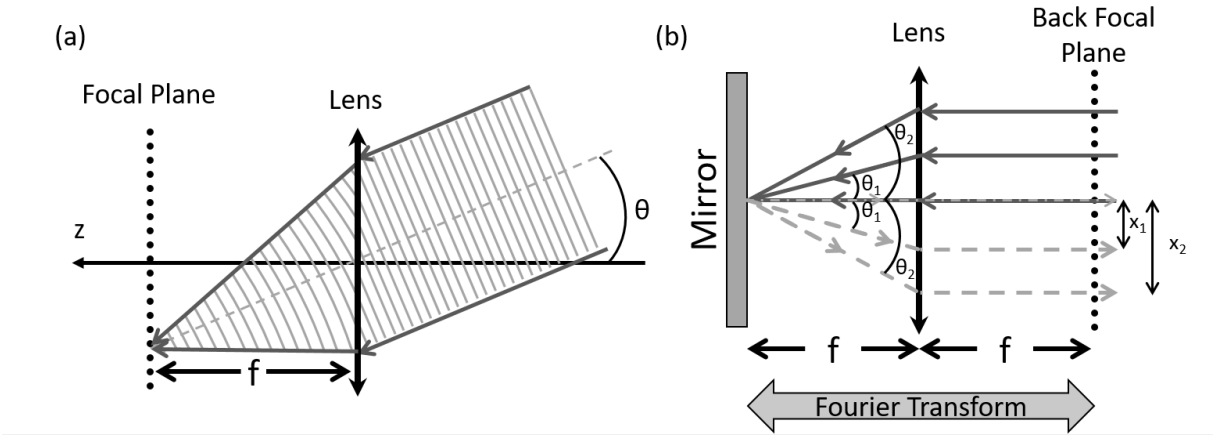


Figure 2.5: **Back Focal Plane of a thin lens**. (a) Incidence of a plane wave onto a lens at an angle θ. (b) The Fourier transform of light reflected from a mirror is induced by a lens .

from the optical axis (x_1 and x_2) and we can therefore read the BFP to extract information on the angle-dependent reflection. Crucially, the orientation of the features of the sample will be manifested in the orientation of the features in the BFP, which will become evident later. Therefore, this technique can measure very small areas, reveal the angular dispersion, and it can easily scan through wavelengths allowing for fast speed.

The previous schematic, however, is valid only for a lens with a negligible thickness compared to the radius of curvature, i.e. a thin lens [260]. To focus light on samples, objective lenses are used under two configurations: with air and with oil between the lens and the sample; the latter is schematised in figure 2.6, the advantage of which will become evident. The Numerical Aperture (NA) of a lens is defined from the maximum angle (θ_{max}) that the lens can direct onto the sample when a collimated beam fills the aperture. It is given by:

$$NA = n_{medium} \sin(\theta_{max}), \tag{2.13}$$

where n_{medium} is the refractive index of the medium between the lens and the sample. For air, $n_{medium} = 1$ and $n_{medium} = 1.515$, matching the refractive index of the substrate and the lens. The NA presents the major limitation with this technique because it determines the maximum momenta that can be accessed. To visualise the reason, we focus our attention on the ray tracing inside an oil immersion objective lens.

In figure 2.6, we present this for an oil immersion lens. F_1 represents the real image which is then projected onto the back focal plane at F_2. Because objective lenses can't be treated as thin lenses, the distance along the optical axis from the start of the lens to the focal point and the BFP is not as trivial as before. The real image is at the focal length (adjusting for the refractive index of the media) from the plane tangent (principal plane or PP_1) to the spherical surface (SS) of the lens. The Fourier image is at the focal length from the second principal plane (PP_2). The latter plane corresponds to the intersection plane between the reflected parallel beams and the rays emerging from the second focal point of the lens. Importantly, the size of the back aperture (D) is key to determining the NA of the lens. From this schematic, it becomes evident that:

$$D = 2nf \sin\theta_{max} = 2f \cdot NA. \tag{2.14}$$

USC DE SANTIAGO DE COMPOSTELA

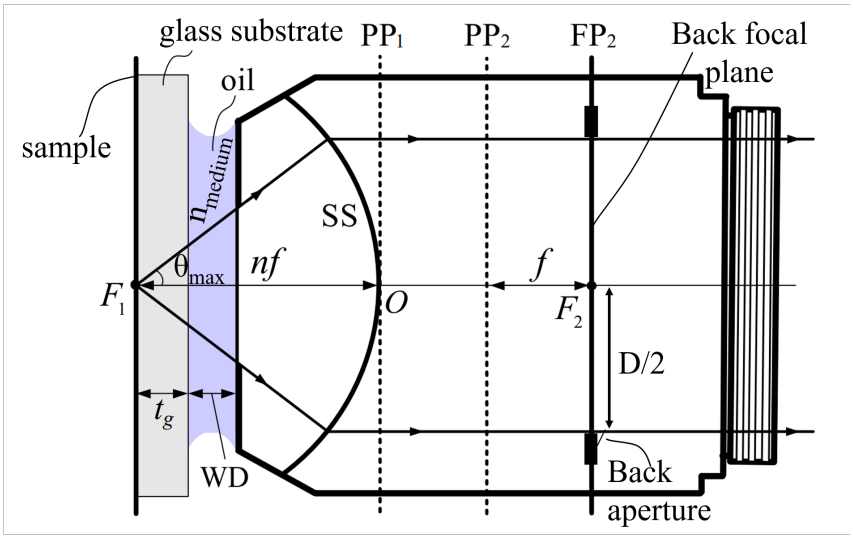


Figure 2.6: **Ray tracing in objective lenses**. An oil immersion lens where F_1 and F_2 are the real and Fourier image respectively, SS is the spherical surface of the lens, α is the maximum angle of capture, f is the focal length, n is the refractive index of the medium (which matches that of the substrate and lens for the oil), WD is the working distance of the lens, t_g is the thickness of the substrate, PP_1 is the first principal plane, PP_2 is the second principal plane. Adapted from reference [261].

Therefore, to couple to high momenta, we require a high refractive index but also a large aperture and a small focal point.

Throughout our work, three different lenses are used: two with air and one oil immersion lens. The smallest magnitude lens is the Olympus Plan N 4× which has $NA = 0.10$, giving $\theta_{max} = 5.7°$. This provides negligible information on the angle-dependent response of the sample and hence, this is used only for normal incidence transmission and reflection measurements. For higher magnifications and NA, the lens Nikon Plan Fluor 40× OFN25 DIC M/N2 with $NA = 0.75$ is used. This lens is designed to provide high-quality images within the visible wavelengths and it gives a maximum angular aperture of 48.6°, thus showing a significant angular response. Thanks to this, important photonic information can be extracted, such as the blueshift at higher angles of photonic crystals, seen in figure 2.4 (c), for example. Note that, with these lenses, the sample is typically facing the lens, whilst the substrate is facing it away (in contrast to what happens with the oil immersion lens).

To allow light beyond the air/light line to reach the lens, we must make it so that there is no total internal reflection on the side of the sample where light is captured by the objective lens. For that, we match the refractive index of the medium, with the refractive index of the lens and the substrate of the sample. This is done by adding oil between these two media which has the same refractive index ($n_{oil} = 1.515$), effectively creating a single medium between the lens and the sample, pushing the numerical aperture higher, beyond the air light line [261, 262]. This is why the substrate has to be facing towards the lens. For this technique, we use the lens Nikon plan APO 100x with $NA = 1.45$, giving it $\theta_{max} = 73.8°$. This technique was first proposed by Bouhelier and Wiederrecht in 2005 [187, 188] and it presented an alternative to the commonly used prism coupling technique, bringing many advantages such as measuring a large momenta range at the same time, measuring very

Table 2.1: Summary of the characteristics of the lenses.

Code	Magnification	f (mm)	NA	θ_{max} (°)	WD (mm)	n_m
Olympus Plan N	4x	45	0.1	5.7	18.5	1
Nikon Plan Fluor	40x	5	0.75	48.6	0.66	1
Nikon Plan Apo	100x	2	1.45	73.8	0.13	1.515

small areas (~ 1 μm^2 in our set up), and easy implementation. Despite these, it continues to be less frequently used in the literature.

Due to the small working distance (WD) of this lens[3], a thin substrate is needed to be able to focus beyond this substrate on the sample. In our work, we consistently use a square microscope glass slide, with a side of 25 mm and thickness $t_g = 0.17$ mm. In the next subsections, we'll briefly explain how we extract the information in the BFP of a reflection measurement with a sensor and how we then convert that to obtain the angle-dependent reflection response. The aforementioned characteristics of the lenses and other relevant ones are given in the table. Note that all objective lenses are infinity-corrected.

2.3.2 Set-up

The full Fourier microscope set-up used throughout this thesis is shown in figure 2.7. We note that every piece of optics in this set-up is designed to work within the VIS since this is the region of interest in this dissertation. The focal distances for every lens are represented with the exception of objective lenses since they can't be treated as thin lenses.

The source of light is a tungsten-halogen white light lamp coupled to an optical fibre with a variable diameter: 400, 105, 50, or 25 μm. The size of the diameter will then influence the size of the focused spot on the sample. This fibre directs light to an objective lens that collimates the light which is directed to the microscope cage, a Nikon Eclipse Ti2. Note that the cage is simplified in this picture, since in reality, the light goes upwards, creating a 3D system. Two consecutive mirrors are used to ensure that the light beam is well-aligned and parallel to the surface. The laser path is used to shine a fluorescent sample with a strong illumination source to then measure the photoluminescence. In the microscope cage, the light goes through the reflection and the transmission paths, where, in the latter, lenses and focal lengths are represented with a prime superscript. In the transmission path, the collection objective lens used has the smallest magnification (4x Olympus) which can only collect angles up to 5.7° and this path, therefore, captures only at normal incidence. To ensure the most accurate measurements, the fibre connecting to the spectrometer is at the centre of the Fourier image which, as shown in the previous section, corresponds to the normal incidence of the reflectance.

As suggested in the schematic, both the transmission and the reflection paths are in the 4f configuration system where lenses L_3 (L_3') and L_4 (L_4') are used to translate the back focal plane of the reflection (transmission) path. Two irises are found in the reflection path. The first serves to reduce the size of the real image to focus on a specific region of the spot and the second iris serves the same purpose but for the Fourier image. The polariser is used to select between s- or p-polarised. After the second iris, light can be directed up to four different detectors: Three CCD cameras (A, B, and C) and a spectrometer. Cameras A

[3]Defined as the distance between the focal point and the outermost part of the lens.

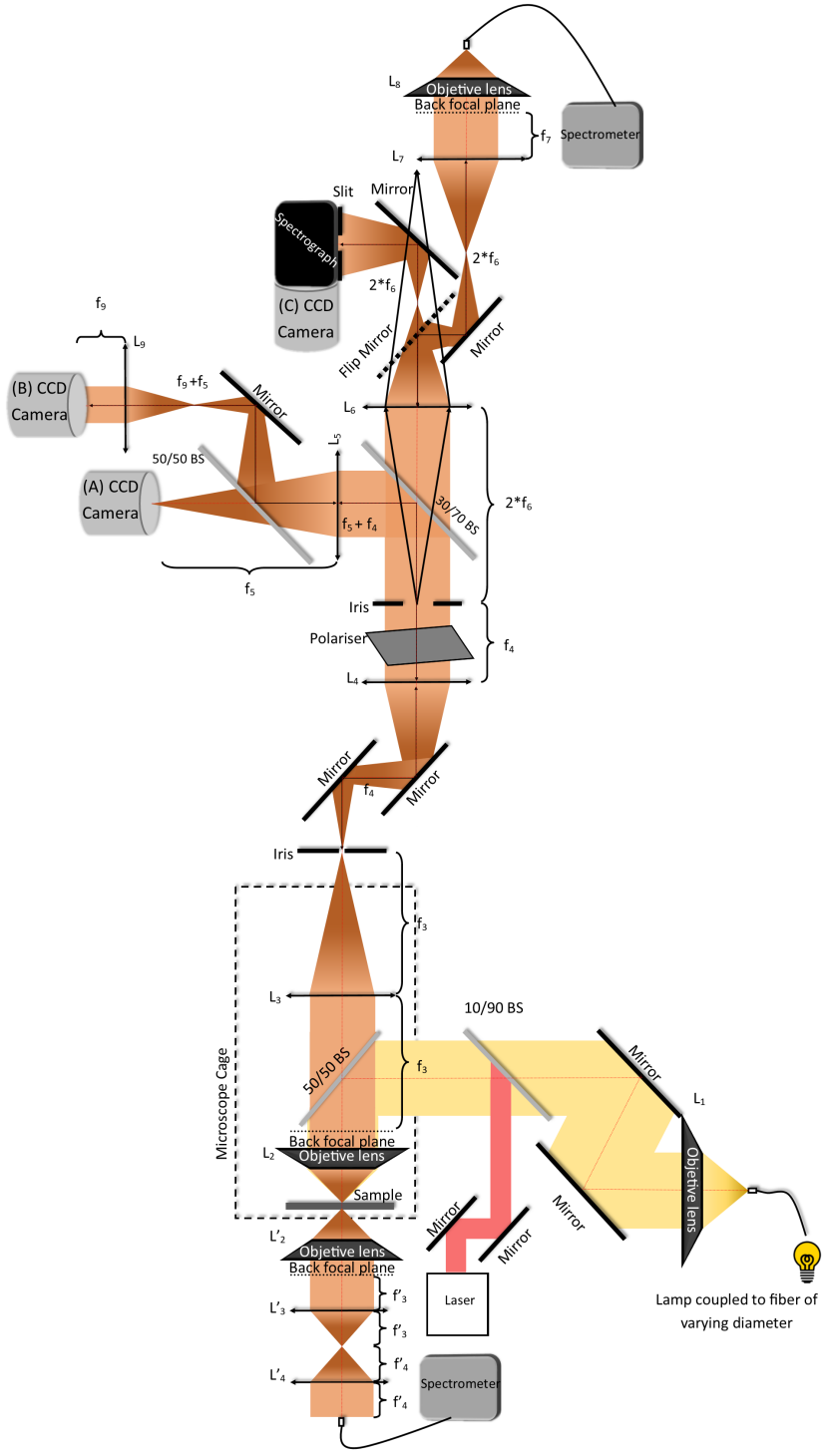


Figure 2.7: **Fourier microscope setup**. Schematic of the set-up used to perform angle-resolved reflectance measurements and normal incidence transmission. Note that the microscope cage is simplified since, in reality, it presents a 3D structure where the 50/50 beam splitter sends light upwards. BS stands for beam splitter, L for lens and f for the focal length of that lens.

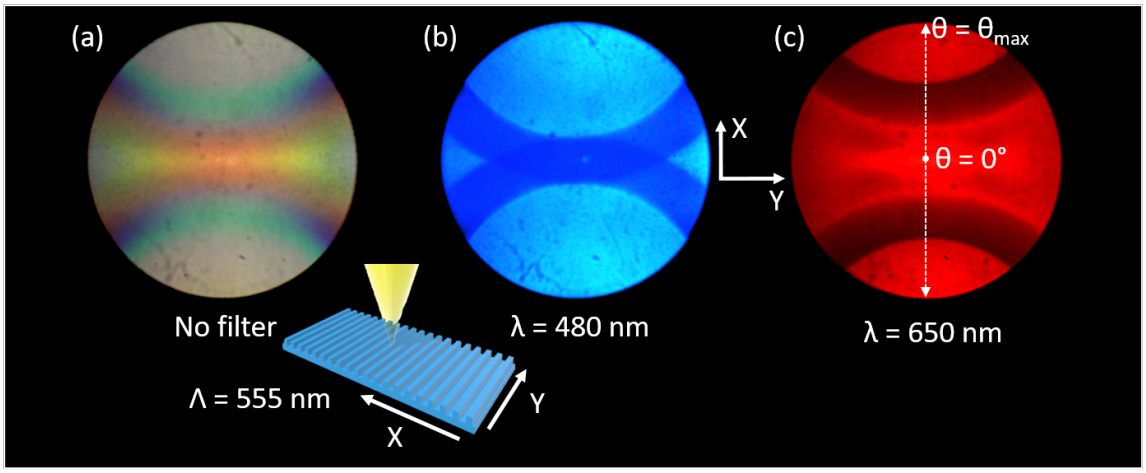


Figure 2.8: **Fourier image of a grating**. The inset represents the grating with a period of 555 nm. (a) Unfiltered and filtered light at (b) $\lambda = 480$ nm and (c) $\lambda = 650$ nm. The X and Y axes represent the direction along the grating and the direction of reflection.

and B capture, respectively, the Fourier image and the real image of the measurement. An example of a reflective grating with a period of $\Delta = 555$ nm is seen in figure 2.8, filtered at different wavelengths. Gratings diffract light into different directions, creating angles where diffracted light no longer reenters the measurement and we obtain no reflection; this is highly dependent on the incident wavelength yielding the rainbow-like distribution seen in subfigure (a). Filtering light at particular wavelengths reveals dark rings which represent the first order of diffraction of the grating. These rings occur at longer momenta for longer wavelengths (subfigures (b) and (c)). Importantly, the orientation of the Fourier space image, depends on the direction of the periodicity of the sample, as demonstrated in the inset of the figure. In the next subsection, we'll see how to use this image to extract the angular reflectance information. To measure reflectance a relay lens, L_6, is used to translate the Fourier image to a 2f distance away to be detected in either one of the two spectrometers shown.

2.3.3 Collecting the Fourier image

With the flip mirror on, light is focused onto the fibre connected to the spectrometer, meaning that we integrate over all angles. Even though this removes any angular information, this integration allows for extremely small exposure times in the measurements and hence good time resolution. A different configuration can also be used here where the fibre connecting to the spectrometer is moved to the location of L_7 to measure normal incidence, similar to the transmission path. This provides accurate normal incidence measurements, though the exposure time has to be made longer. The fibre used has a diameter of 200 µm, big enough to let in sufficient light for practical exposure times while small enough to allow only quasi-normal incidence light from the Fourier plane. Inside the spectrometer, two converging mirrors are used to focus the light from the entrance on a 1D CCD photodetector, as shown in figure 2.9. The grating between the two mirrors splits the light into different wavelengths. The system is calibrated such that each pixel of the detector corresponds to a specific wavelength.

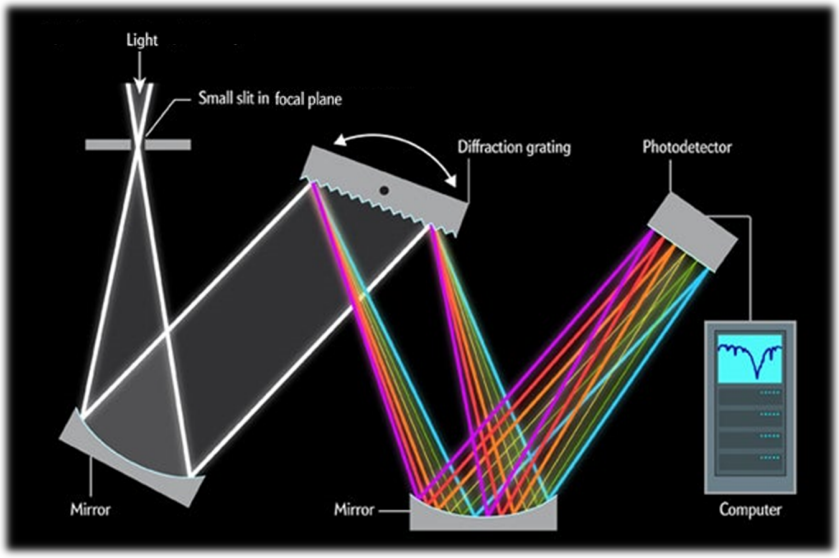


Figure 2.9: **Spectrometer**. Illustration of the light path inside a spectrometer. Extracted from [263].

Lowering the flip mirror will take the light to the spectrograph. At the entrance, a slit is found to allow only the angular information along a specific direction through the system. For that reason, it is crucial that this direction matches the direction of the features of interest in the sample. For example, the slit in figure 2.8 has to include the dark rings, i.e. along X. The angular information will be given by the distance to the centre, which corresponds to normal incidence. If we were to measure along Y, we would be measuring a spectrum similar to a standard mirror.

Whilst in the previous spectrometer, we have an array of semiconducting photodetectors which counts the number of incoming photons, discriminating different wavelengths but not the different angles. For angle-resolved measurements, we need a 2D matrix sensor ((C) CCD camera) to discriminate both simultaneously. The spectrograph performs a similar function to the spectrometer where an optical grating distributes light such that a specific dimension of the matrix collects wavelength information whilst the other dimension captures spatial information. Unlike wavelength, the spatial information cannot be directly given by the device and the collected data has to be analysed to extrapolate from pixel number to angle. The spectrometer used is a fibre-coupled 2000+ Ocean Optics (Dunedin, USA), the spectrograph is from Princeton Instruments, Acton SpectraPro SP-2150, and the (C) CCD camera is a QImaging Retiga R6 USB3.0 Colour. The details of these devices are beyond the scope of this work. A hurdle presented from this measurement technique is the fact that the (C) CCD camera can only capture a $\sim$ 35 nm wavelength range at once and, for that reason, several measurements have to be taken to capture the desired range. This requires further data processing to stitch individual measurements together. This means that, after measuring, two data processing steps have to be done: stitching the data and extrapolating angular information.

Note that the reflection measured by either sensor (R'_{sample}) has to be normalised against a reference ($R'_{reference}$) to obtain reflectance of the sample (R), since the sensor counts only the number of incident photons. A silver mirror is used as a reference in here due to its

unmatched reflective properties in the VIS. Moreover, we have to subtract dark noise on each of these measurements (D_{sample} and $D_{reference}$). Consequently, four measurements are needed to obtain the reflectance of a sample:

$$R = \frac{R'_{sample} - D_{sample}}{R'_{reference} - D_{reference}}. \tag{2.15}$$

To maximise the signal-to-noise ratio of the measurements, the exposure times of the samples and references should be individually maximised up to the point where they start to saturate.

2.3.4 Data extraction from the Fourier image

To explain the data extraction and processing of the data obtained from the set-up, we will use the same optical grating with a period of $\Lambda = 555$ nm due to its well-defined optical features within the wavelengths of interest. Light incident from the air on an optical grating with an angle θ_{in} gets scattered to a different direction according to the grating equation [259]:

$$\sin(\theta_{out}) = \sin(\theta_{in}) \pm m\frac{\lambda}{\Lambda}, \tag{2.16}$$

where m is the order of diffraction of the grating. This effect is shown in figure A.4. The Wood anomaly occurs when the scattered light cannot be "captured" by the lens because the incident angle goes along the in-plane direction, i.e. $\theta_{out} = 90°$:

$$\theta_{exit} = \arcsin\left(1 - m\frac{\lambda}{\Lambda}\right). \tag{2.17}$$

Note that, for simplicity, we are looking only at the positive orders of the grating equation. Therefore, when $\theta_{in} < \theta_{exit}$, the grating behaves like a standard mirror and when $\theta_{in} > \theta_{exit}$, the diffraction condition is satisfied and the beam is diffracted. One of two situations can now occur: $\theta_{out} > \theta_{max}$ or $\theta_{out} < \theta_{max}$. Remember that, θ_{max} is the maximum angle that the objective lens being used can capture and is intrinsically connected to the NA. Therefore, when $\theta_{out} < \theta_{max}$, the diffracted order is collected. If however, $\theta_{out} > \theta_{max}$, then the diffracted order can't be collected and the sensor reads zero reflectance (under ideal conditions). The dark rings observed in figure 2.8 correspond to the situation when $\theta_{out} > \theta_{max}$. Therefore, reflectance will "re-enter" the sensors when $\theta_{out} < \theta_{max}$. It is trivial to show that this occurs when:

$$\theta_{reenter} = \arcsin\left(\frac{NA}{n_{medium}} - m\frac{\lambda}{\Lambda}\right), \tag{2.18}$$

where the working medium is air, hence $n_{medium} = 1$.

The aforementioned grating was measured in reflection using the 40x lens ($NA = 0.75$) for wavelengths $370 < \lambda < 840$ nm. To obtain this range, 14 measurements centred at different wavelengths were stitched together using a MATLAB program. Figure 2.10 (a) shows the reflectance measurement over these ranges where the dark regions correspond to the first and second order of diffraction. On the y-axis, we see the wavelength extrapolated directly by the sensor. For low wavelengths, $\lambda < 390$ nm, absorption by the optical components makes the measurements become noisy due to the signal-to-noise ratio reduction. In contrast,

USC UNIVERSIDADE DE SANTIAGO DE COMPOSTELA

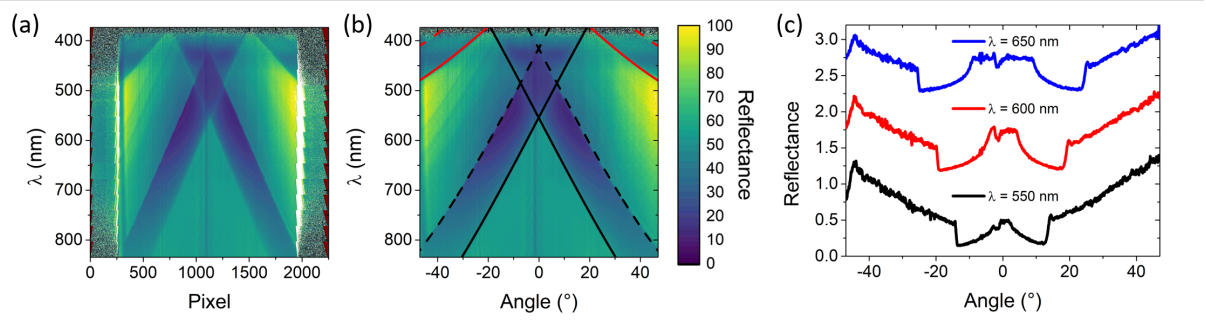


Figure 2.10: **Fourier image reflectance**. (a) Unprocessed and (b) processed reflectance data. In the latter, the grating equations for the exit (solid) and reenter (dashed) of light in the grating are seen for the first two orders of diffraction (black is the first and red is the second). (c) Horizontal cross-section at an increasing wavelength.

on the x-axis, we see the pixel number of the camera. We need to perform further data processing to extrapolate angular information. For pixels away from the centre, we observe noise which corresponds to the region where no light was incident. Note that the reflectance isn't zero because we're dividing by a reference with equally low values. In fact, the limit between this noisy region and the non-noisy region corresponds to the maximum angle of collection.

To extrapolate the angular information from pixel number, we match two pixel values to two angle values ($\pm\theta_{max}$) and the normal incidence corresponds to the pixel between these. From here, we can induce for each pixel the corresponding angle value. Because the initial selection of the pixel corresponding to θ_{max} is not perfect, a multiplication factor is given by trial and error until we obtain the best fit possible. The calibration grating becomes convenient for this step since it presents clear features over all wavelengths. Figure 2.10 (b) shows the post-process data from subfigure (a) with the grating equations showing phenomenal matching. The black and red lines correspond to the first and second diffraction order respectively and the solid and dashed lines correspond to the exit (equation 2.18) and reentry of light (equation 2.17). The dark line near normal incidence corresponds to noise caused by back reflections within this objective lens. In subfigure (c), the cross-sections of this plot show the redshift of the wood anomaly as the wavelength is increased.

USC UNIVERSIDADE DE SANTIAGO DE COMPOSTELA

USC
UNIVERSIDADE
DE SANTIAGO
DE COMPOSTELA

Part II

Publications

USC
UNIVERSIDADE
DE SANTIAGO
DE COMPOSTELA

USC
UNIVERSIDADE
DE SANTIAGO
DE COMPOSTELA

CHAPTER 3

Light-Dependent Morphological Changes Can Tune Light Absorption in Iridescent Plant Chloroplasts: A Numerical Study Using Biologically Realistic Data

- Journal: ACS Photonics
  - Publisher: American Chemical Society
  - Impact factor: 7.15 (2021)
  - Relative position: Q1 in all categories
  - h-index: 99
  - SCImago Journal Rank: 2.273
- Thesis author's contribution: As written in the paper, designed and ran the optical models and was the main contributor in conceiving the experiments, analysing the data, and writing the manuscript.
- CASTILLO, Miguel A.; WARDLEY, William P.; LOPEZ-GARCIA, Martin. Light-Dependent Morphological Changes Can Tune Light Absorption in Iridescent Plant Chloroplasts: A Numerical Study Using Biologically Realistic Data. ACS Photonics, v. 8, n. 4, p. 1058-1068, 2021. ISSN: 2330-4022
- Note: In the paper the affiliation to the University of Santiago is not shown. A correction to the article was added to amend this.
- https://doi.org/10.1021/acsphotonics.0c01600

USC
UNIVERSIDADE DE SANTIAGO DE COMPOSTELA

RightsLink

Home | Help | Live Chat | Sign in | Create Account

ACS Publications
Most Trusted. Most Cited. Most Read.

Light-Dependent Morphological Changes Can Tune Light Absorption in Iridescent Plant Chloroplasts: A Numerical Study Using Biologically Realistic Data

Author: Miguel A. Castillo, William P. Wardley, Martin Lopez-Garcia
Publication: ACS Photonics
Publisher: American Chemical Society
Date: Apr 1, 2021

Copyright © 2021, American Chemical Society

PERMISSION/LICENSE IS GRANTED FOR YOUR ORDER AT NO CHARGE

This type of permission/license, instead of the standard Terms and Conditions, is sent to you because no fee is being charged for your order. Please note the following:

- Permission is granted for your request in both print and electronic formats, and translations.
- If figures and/or tables were requested, they may be adapted or used in part.
- Please print this page for your records and send a copy of it to your publisher/graduate school.
- Appropriate credit for the requested material should be given as follows: "Reprinted (adapted) with permission from {COMPLETE REFERENCE CITATION}. Copyright {YEAR} American Chemical Society." Insert appropriate information in place of the capitalized words.
- One-time permission is granted only for the use specified in your RightsLink request. No additional uses are granted (such as derivative works or other editions). For any uses, please submit a new request.

If credit is given to another source for the material you requested from RightsLink, permission must be obtained from that source.

BACK CLOSE WINDOW

© 2022 Copyright - All Rights Reserved | Copyright Clearance Center, Inc. | Privacy statement | Data Security and Privacy | For California Residents | Terms and ConditionsComments? We would like to hear from you. E-mail us at customercare@copyright.com

USC UNIVERSIDADE DE SANTIAGO DE COMPOSTELA

CHAPTER 4

Enhanced Light Absorption in All-Polymer Biomimetic Photonic Structures by Near-Zero-Index Organic Matter

- Journal: Advanced Functional Materials
  - Publisher: Wiley
  - Impact factor: 19.92 (2021)
  - Relative position: Q1 in all categories
  - h-index: 349
  - SCImago Journal Rank: 5
- Thesis author's contribution: As stated in the paper, helped conceive the work and analyse the optical data. Fabricated the samples and performed their optical measurements. Designed and ran the optical models. Contributed to the writing.
- CASTILLO, Miguel A. et al. Enhanced Light Absorption in All-Polymer Biomimetic Photonic Structures by Near-Zero-Index Organic Matter. Advanced Functional Materials, v. 32, n. 21, p. 2113039, 2022. ISSN: 1616-3028
- https://doi.org/10.1002/adfm.202113039

USC
UNIVERSIDADE DE SANTIAGO DE COMPOSTELA

Miguel Castillo

From: Rights DE <RIGHTS-and-LICENCES@wiley-vch.de>
Sent: 30 August 2022 10:24
To: Miguel Castillo
Subject: WG: Publication as a part of the thesis - adfm.202113039

Não costuma receber e-mails de rights-and-licences@wiley-vch.de. Saiba por que motivo isto é importante

CAUTION: This email originated from a source outside INL. **DO NOT** click links, open attachments, or reply unless you recognize the sender and know the content is safe. **REPORT** any suspicious message to ICS Support.

Dear Miguel Castillo,

We hereby grant permission for the requested use expected that due credit is given to the original source.

If material appears within our work with credit to another source, authorisation from that source must be obtained.

Credit must include the following components:

- Journals: Author(s) Name(s): Title of the Article. Name of the Journal. Publication year. Volume. Page(s). Copyright Wiley-VCH GmbH. Reproduced with permission.

If you also wish to publish your thesis in electronic format, you may use the article according to the Copyright transfer agreement:

3. Final Published Version.
Wiley-VCH hereby licenses back to the Contributor the following rights with respect to the final published version of the Contribution:
a. […]
b. Re-use in other publications. The right to re-use the final Contribution or parts thereof for any publication authored or edited by the Contributor (excluding journal articles) where such re-used material constitutes less than half of the total material in such publication. In such case, any modifications should be accurately noted.

Kind regards

Bettina Loycke
Senior Rights Manager
Rights & Licenses

Wiley-VCH GmbH
Boschstraße 12
69469 Weinheim
Germany
www.wiley-vch.de

T +(49) 6201 606-280
F +(49) 6201 606-332
rightsDE@wiley.com

WILEY

Celebrate ***100 Years of Growing Knowledge*** with us:
2021 marks our anniversary year: VCH was founded in 1921, Wiley-VCH in 1996. Please join us in celebrating this success and have a look at our anniversary website.

CHAPTER 5

Tunable narrowband Excitonic Optical Tamm States enabled by a metal-free all-organic structure

- Journal: Nanophotonics
  - Publisher: Walter de Gruyter
  - Impact factor: 7.92 (2022)
  - Relative position: Q1 in all categories
  - h-index: 72
  - SCImago Journal Rank: 2.124
- Thesis author's contribution: As stated in the paper, helped conceive the work and analyse the optical data. Fabricated the samples and performed their optical measurements. Major contribution to the design of optical simulations and to the writing.
- CASTILLO, Miguel A. et al. Tunable narrowband Excitonic Optical Tamm States enabled by a metal-free all-organic structure. Nanophotonics, v. 11, n. 21, p. 4879–4888, 2022. ISSN: 2192-8606
- https://doi.org/10.1515/nanoph-2022-0419

USC
UNIVERSIDADE DE SANTIAGO DE COMPOSTELA

Miguel Castillo

From: Editorial Nanophotonics <nanophotonics.editorial@degruyter.com>
Sent: 15 November 2022 21:49
To: Miguel Castillo
Subject: RE: Paper as part of a PhD thesis
Attachments: License_to_Publish_signed.pdf

CAUTION: This email originated from a source outside INL. **DO NOT** click links, open attachments, or reply unless you recognize the sender and know the content is safe. **REPORT** any suspicious message to ICS Support.

Dear Author,

thank you for the email.

The article "Tunable narrowband Excitonic Optical Tamm States enabled by a metal-free all-organic structure," co-authored by you was published under the **CC-BY** license.

Under the terms of this license, from our side (the publishing house) there is no problem that you re-use the material, only a proper citation is needed (e.g., that the chapter was published as an article – citation, incl. DOI link).

Castillo, Miguel, Cunha, Diogo, Estévez-Varela, Carla, Miranda, Daniel, Pastoriza-Santos, Isabel, Núñez-Sánchez, Sara, Vasilevskiy, Mikhail and Lopez-Garcia, Martin. "Tunable narrowband excitonic Optical Tamm states enabled by a metal-free all-organic structure," *Nanophotonics*, vol. 11, no. 21, pp. XX-XX, 2022. https://doi.org/10.1515/nanoph-2022-0419

The article will be published as part of Issue 21 scheduled for the end of the month. Page numbers will then be assigned.

Best regards,
Justyna Zuk

***
Dr. Justyna Żuk
Justyna.Zuk@degruyter.com

Journal Coordinator
Nanophotonics
degruyter.com/nanoph

DE GRUYTER
degruyter.com

De Gruyter Poland Ltd. Ul. Bogumila Zuga 32a. 01-811 Warsaw, Poland
Domicile Warsaw, Poland. Legal Form: Limited Company
Managing Director: Jacek Ciesielski

***



Editorial contact:
nanophotonics.editorial@degruyter.com

Part III

Results and discussion

USC
UNIVERSIDADE
DE SANTIAGO
DE COMPOSTELA

USC
UNIVERSIDADE
DE SANTIAGO
DE COMPOSTELA

CHAPTER 6

Discussion of the publications

So far, we have addressed several diverse topics. We started by connecting photosynthesis and photonics, leading us to study the photonic photosynthetic organism known as iridoplast. Our initial thesis is that these structures have as their primary function light absorption enhancement via slow light effects and light absorption tunability by responding to different light intensities. To prove our hypothesis, we theoretically studied the optical properties of structured chloroplasts by taking data available from the literature. The results were published in ACS Photonics. To experimentally validate the slow light-induced absorption enhancement, we fabricated a biomimetic structure with similar photonic and chemical properties, resulting in the second publication of this dissertation.

However, the polaritonic properties of the material and the fabrication techniques used here open the door to further work by creating new research questions: can we create low-cost, environmentally friendly, and scalable photonic structures by replacing inorganic and metallic materials with fully organic ones? Throughout the rest of this dissertation, we show different photonic structures with properties equivalent to those extensively studied in plasmonics. Particularly, the metal-like optical properties of TDBC-PVA were used to demonstrate light confinement in an optical Tamm state and a grating structure is shown to allow the coupling of a polariton state towards lower momenta. This resulted in the publication of a third paper and in the preparation of a fourth one. The preliminary results from the latter are discussed in the next chapter.

In the following sections, we discuss and connect the publications shown in the previous part. We briefly expand on some results which were not presented in the publications. Note that, unless stated otherwise, the figures, equations, and tables referred to throughout the sections of this chapter will be referring to the paper corresponding to that section.

6.1 Theoretical analysis of photonic chloroplasts

For this dissertation, we begin by expanding the work of Jacobs et al. from 2016 [1] which set the roots for this work. The authors analysed numerous TEM images taken of iridoplasts of a particular blue *Begonia* cross-breed to get an accurate representation of their structure, particularly the thicknesses of the layers represented in figure 1.8 of this dissertation. To simulate the photonic properties of this structure and compare the results to the experimentally observed optical response, the refractive index of the layers is needed. The authors take the refractive index of the lumen and stroma to be the same as that of water ($n = 1.33$) and

USC UNIVERSIDADE DE SANTIAGO

extract the refractive index of the thylakoid membranes from the reference [109]. The latter is critical as it is responsible for the absorption in the system, however, the work used methods to calculate the refractive index that might not provide accurate results. Nonetheless, as there have been no further studies looking at the refractive index of thylakoid membranes[1], neither for structured nor non-structured chloroplasts, we have taken the same results in this dissertation. From the structural and refractive index information, the authors were able to study the photonic properties of this system by performing 1D simulations. A good agreement between the theoretically predicted and the experimentally measured reflectivity response was found by the authors. In addition, the slow light properties were investigated, where the induced light absorption enhancement at the edge of the photonic band gap was shown to occur in the green region of the visible spectrum, where light availability is most abundant, and the absorption reduction, due to the photonic band gap, occurred in the blue, where the light had mostly been attenuated. In addition to these results, three main points required further expansion:

- Light-dependent morphological changes
- 1D disorder of the thickness of layers
- Quantitative impact of the slow light

In the paper entitled: "Light-Dependent Morphological Changes Can Tune Light Absorption in Iridescent Plant Chloroplasts: A Numerical Study Using Biologically Realistic Data", we have addressed these three points. We have also extended the analysis to another photonic photosynthetic system, the bizonoplast.

Detailed morphological studies of photonic chloroplasts, i.e. including the thickness of single thylakoid membrane and lumen layers, have only been done under low-light adjusted structures, both for iridoplasts [1] and bizonoplasts [111]. To extrapolate the structure under high-light induced expansion, we apply to these low-light adjusted systems the same proportional thickness variation observed by Kirchhoff et al. [126] and Pao et al. [116]. The results are summarised in tables 1 and 2. The structure of non-iridescent chloroplasts and iridoplasts are given in figure 1 (a) and (b) respectively with (c) showing the detailed composition of the grana, which we assume to be same in both systems. Both chloroplasts are composed by 8 stacked grana with the difference being the spacing between each: whilst in non-structured chloroplasts, the stromal spacing between each grana is considered to be zero, in the iridoplasts it is 125 nm (under low light). This crucially provides the chloroplasts with the same volume of absorptive material as the iridoplast, such that it can then be used as a reference to calculate the absorption enhancement factor γ, in equation 1.13 of the dissertation. For bizonoplasts, figure 4 (a) shows similar structural information. Similar to iridoplasts, the reference for bizonoplasts will be obtained by setting the stromal spacing between grana in the structured zone to zero, whilst keeping everything else unchanged. Because the dimensions of the thylakoid membranes and lumen are different between the two photonic chloroplasts, the two references will also have different unit cells (granum).

Using the Transfer Matrix Method described in section 2.1 of this dissertation, we can calculate the reflectance and slow light-induced absorption enhancement, of photonic chloroplasts under low and high light conditions. Applying data available from the literature

USC UNIVERSIDADE DE SANTIAGO DE COMPOSTELA

[1]Note that, even though Capretti et al. [6] did study this, they ignored the lower wavelengths ($\lambda < 550$ nm), which are critical for this work.

[1, 116, 126], the results calculated are given in figures 2, 3, and 4. As a consequence of the light-dependent morphological expansion of the photonic crystal, the reflectance peak is observed to both redshift by ~ 100 nm, from 450 to 550 nm, and to reduce in strength from 12% to 4% for iridoplasts and to redshift by ~ 80 nm, from 450 to 530 nm, and to reduce in strength from 27% to 22% for bizonoplasts. These conclusions are resilient to the natural disorder found in the photonic system.

In addition, under the high light-induced structural expansion, not only is the light absorption enhancement factor (γ) redshifted but it is also flattened, reducing the slow light effects. To quantify the impact of slow light, we calculate the light absorption enhancement over all wavelengths (γ_{total}). This is given by the ratio between the total energy absorbed by the iridoplast and the non-structured chloroplast. Two improvements are needed in the equation used in the paper[2]. First, we integrated over energy, instead of wavelength. Energy integration is not accurate since the units of the PAR take the photon wavelength into account. This, however, showed no significant difference. Second, since γ is not wavelength independent, we mustn't use it in this calculation. Therefore, the correct equation to calculate the total absorption enhancement is:

$$\gamma_{total} = \frac{\int PAR(\lambda) \cdot A(\lambda)_{\text{iridoplast}} d\lambda}{\int PAR(\lambda) \cdot A(\lambda)_{\text{chloroplast}} d\lambda}. \tag{6.1}$$

For the rest of the discussion of this publication, we will show the results obtained from this equation whilst including the previous results in brackets for comparison. Under low light conditions, i.e. using the PAR below the forest canopy and the low light adjusted photonic chloroplast structure, we find that the photonic structure enhances absorption by 4% (6%), i.e. $\gamma_{total} = 1.04$ (1.06), for iridoplasts and by 1% (1%), i.e. $\gamma_{total} = 1.01$ (1.01), for bizonoplasts when compared to standard chloroplasts. Under high light, i.e. using the PAR over the forest canopy and using the high light adjusted iridoplast structure, the photonic system presents no overall effect for iridoplasts, i.e. $\gamma_{total} = 1.00$ (0.98) and negligible for bizonoplasts, $\gamma_{total} = 0.99$ (0.98), when compared to a high light adjusted standard chloroplast. This demonstrates tunability under different light conditions, particularly for iridoplasts. These values remain unchanged when the disorder is considered.

Finally, we studied the absorption tunability of each of the three chloroplasts studied by using as a reference the chloroplast itself adjusted to high light conditions. We repeat the calculation, on disordered systems, of the total absorption enhancement over all wavelengths for the two different PAR: under and above the canopy. Note that we continue to use the accurate formula, equation 6.1 of the manuscript. Respectively for above (direct sunlight) and below the forest canopy, we find that: for iridoplasts $\gamma_{total} = 1.16$ (1.19) and 1.19 (1.25); for chloroplasts, $\gamma_{total} = 1.14$ (1.15) and 1.15 (1.16); for bizonoplasts $\gamma_{total} = 1.04$ (1.06) and 1.10 (1.14). Comparing with the results obtained in the published work, in brackets, shows that, despite the inaccuracy in equation 2, the conclusions remain the same.

6.1.1 Conclusions and comments

In this paper, we have demonstrated that, assuming photonic chloroplasts undergo similar light-sensitive morphological adjustments to the ones observed in the literature:

[2] I would like to thank Alex Qiu, from the University of Bristol, for being an essential part of finding these mistakes and correcting them.

- Under high light conditions, both iridoplasts and bizonoplasts redshift their characteristic structural colour and slow light-induced absorption enhancement. This enhancement becomes significantly attenuated.
- Iridoplasts show significant tunable overall light absorption enhancement whilst bizonoplasts don't.
- Photonic properties are resilient to biologically realistic disorder.
- All chloroplasts, photonic or not, can tune light absorption, absorbing more when light is scarce; iridoplasts do it better for the PAR available below the forest canopy.

There are, however, a few points worth discussing which weren't included in the paper.

Interestingly, both in high and low light conditions, a very similar absorption enhancement for $\lambda > 680$ nm is observed. Even though this had not been analysed in the publication, this was later investigated separately[3]. To study this, we created a dummy structure with the same number of grana as we've been using. In contrast to the iridoplasts however, the stroma spacing between the different grana is given by a random number between 1 and 200 nm, yielding a non-photonic structure. We calculated the absorption enhancement factor γ for 100 of these structures (due to the random nature of this calculation) and proceeded to average them. The results are observed in figure A.5 of the dissertation. Due to the lack of a photonic structure, this factor is flat for most wavelengths except for $\lambda > 680$ nm. For these wavelengths, the absorption enhancement factor is very similar to what had been observed for the photonic structure. We, therefore, concluded that this is likely caused by an increase in internal diffraction within the expanded system.

In this region, the enhancement in absorption and a higher photon count, suggest that there is potentially a significant amount of energy to be absorbed. However, we have ignored the red wavelength range because they are not included in the "traditional" definition of PAR [29]. However, as previously mentioned, IR photons have been recently suggested to enhance photosynthesis by interacting with higher-energy photons [28]. Interestingly, specialised cyanobacteria have very recently been found to contain chlorophyll-f, responsible for absorbing IR light [264]. These recent advances suggest that photonic chloroplasts could have also developed mechanisms to have red light play an important role in photonic structures as well.

In addition, to find the total light absorption enhancement, (γ_{total}) we are relying on three critical factors: the structure of the system, the refractive index of the thylakoid membranes, and the available PAR. The refractive index used was extracted from measurements on thylakoid membranes from standard chloroplasts and might therefore not be the same as in iridoplasts. For example, the thylakoid membranes of iridoplasts might present a higher concentration of green absorbing pigments, such as carotenoids, which would significantly increase the absorption in this range. In addition, the PAR used, even though it was captured below the forest canopy, might not indicate the actual PAR found under the conditions where photonic photosynthetic organisms are found. Both of these can drastically vary the total light absorption enhancement (γ_{total}) and therefore need further investigation to obtain a complete picture of the photonic properties of these systems.

USC UNIVERSIDADE DE SANTIAGO

[3] In collaboration with Alex Qiu and Ruth Oulten from the University of Bristol.

Importantly, we have so far, considered isolated photosynthetic organisms. However, in the leaves of *Begonias*, below the iridoplasts exists a sea of non-structured chloroplasts, as suggested by figure 6.1 (a). It is therefore expected that iridoplasts, if we include the non-photonic chloroplasts underneath, will present an absorption enhancement similar to bizonoplasts since the overall absorption of the iridoplasts contributes little to the total absorption of the leaf. This is supported by figure 6.1 (b) where we have plotted the enhancement factor γ for an increasing number of non-structured grana below the iridoplast. Here, as we increase the number of grana, the enhancement factor becomes more negligible not only because iridoplasts contribute less to total light absorption, but also because with a large number of grana the wavelengths with enhanced absorption become absorbed regardless of slow light effects. However, because the photonic band gap still plays a role, clearly demonstrated in subfigure (c) by the persisting $\gamma < 1$ region, total light absorbed by the photosynthetic systems containing an iridoplast actually becomes smaller than unity ($\gamma_{total} < 1$), as demonstrated in subfigure (d), yielding the opposite effect to what was initially hypothesised. Compounded with that, confocal images of *Begonia* leaves show that iridoplasts take up at most 12% of the total leaf area [117]. For these reasons, even with the absorption reduction and tunability of the photosynthetic photonic structure, the thesis that these systems evolved to enhance and control light absorption becomes unlikely, even if the total absorption enhancement were to become higher by using a potentially more correct PAR and thylakoid membrane refractive index. Despite this, the enhanced absorption must be directly measured to obtain a full picture of the properties of the system. However, due to the complexity of the biological system, it is not possible to measure this absorption directly in the natural structure. Instead, we create a biomimetic system with similar photonic and absorptive properties.

6.2 Biomimetic iridoplast

As previously discussed in section 1.4, the narrow absorption bands of the thylakoid membranes are key to achieving the near-unit quantum efficiency observed in photosynthesis [265]. This property can be mimicked by natural J-aggregates which provide similar properties [139]. To create an iridoplast biomimetic structure, we must not only produce similar photonic properties but also use pigments with similar absorptive properties. Because of the narrow absorption band of the natural system, we use the J-aggregate TDBC dye to mimic the grana of iridoplasts. We recall that the refractive index of this dye can be modelled by adding a Lorentzian oscillator to the refractive index of the host medium. In fact, using Lorentz oscillators to estimate the refractive index of thylakoid membranes has been preferred, by an author [266], over using the refractive index obtained in reference [109], which has been used in this dissertation.

In the scientific publication "Enhanced Light Absorption in All-Polymer Biomimetic Photonic Structures by Near-Zero-Index Organic Matter", we produced a biomimetic system with similar properties to iridoplasts and studied its photonic properties. The unit cell consists of a homogeneous layer, equivalent to the lumen, and a TDBC-doped layer, equivalent to the grana. The number of unit cells was fixed at 16 to provide strong photonic effects while not high enough absorption that enhancement becomes dampened. Varying the periodicity of the photonic structure by controlling the thickness of the homogeneous layer yields two advantages. Firstly, this is closer to what happens in the natural system since the morphological

USC UNIVERSIDADE DE SANTIAGO DE COMPOSTELA

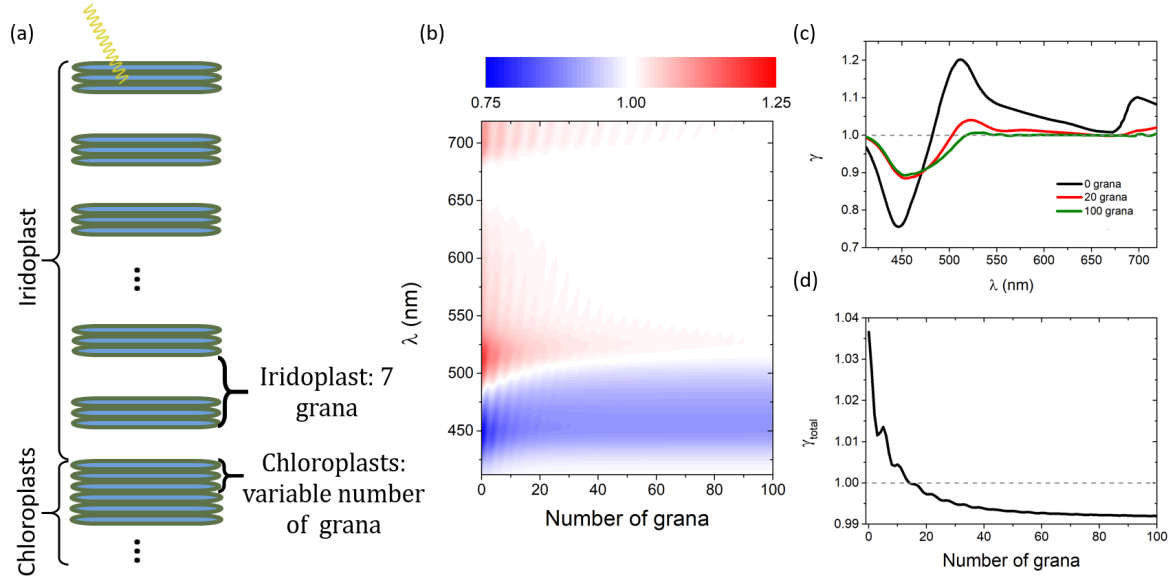


Figure 6.1: **Slow light in the non-isolated system**. (a) Schematic representing the structure considered in these simulations: fixed number of grana in iridoplast and variable non-structured grana below it. (b) Light absorption enhancement factor of system composing of an iridoplast and an increasing number of non-structured grana underneath (x-axis), with morphologies under low light conditions and below the canopy PAR. Note that 100 grana underneath an iridoplast is an underestimate. (c) Cross sections of subfigure (b) for specific number of grana. (d) Total absorption enhancement below the forest canopy, using equation 6.1. The disorder was not considered for any of the plots.

USC UNIVERSIDADE DE SANTIAGO DE COMPOSTELA

changes occur primarily in the homogeneous media, as seen in chapter 3 of this dissertation. Secondly, this is more convenient for the fabrication process and for the absorption enhancement analysis, as discussed in chapter 2.2.

The high concentration of TDBC in the absorptive layer of with PVA delivers highly dispersive real refractive indices, varying between $0.5 < \bar{n}_{TDBC-PVA} < 3.0$ within a small wavelength range, as suggested in the refractive index shown in figure 1 (b). This is much higher than that of thylakoid membranes, where this index was calculated to vary between $1.37 < \bar{n}_{thylakoid} < 1.62$. The TDBC to PVA ratio can be reduced to lower the strength f_0, of the Lorentz equation 1.14 of this dissertation, and hence obtain a refractive index closer to that of the natural system. The reason for using a higher concentration is twofold. First, under this condition, there are new exotic effects, such as the creation of multi-stop bands and the increase in refractive index contrast. Second, the higher absorption from using higher concentration layers in the structure provides more clear experimental measurements. In addition, we need not create an exact replica, just analogous properties to test our hypothesis.

Again using the Transfer Matrix Method based simulations, we theoretically investigated this system. We find that the strong oscillation from doping PVA with TDBC creates a window of PS thicknesses where three photonic band gaps exist for the same structure. Additionally, the strong Lorentz oscillation affects the refractive index away from the resonance such that the TDBC-PVA goes from the low refractive index material, for $\lambda < 550$ nm, to the high refractive index material, for $\lambda > 600$ nm. Consequently, slow light absorption enhancement will also flip photonic band gap edges, depending on where the stop band is. There is also an increased refractive index contrast which inflates absolute reflectance from 40%, for a non-doped system, to over 80%, for a doped system with the same structure. The refractive index of the TDBC-PVA films was confirmed experimentally which showed exceptional agreement with the theoretical predictions for all wavelengths $\lambda > 550$ nm. For wavelengths $\lambda < 550$ nm, there is a small miss-match of ~ 0.05. This makes the refractive index of PVA-TDBC closer to that of PS at lower wavelengths, decreasing the absolute reflectance when the photonic band gap is found at low wavelengths. This decrease, however, is not observed experimentally (figure S4), leading us to think that the refractive index in this range is closer to the theoretical model.

We showed the fabrication of these structures by spin coating, demonstrating accurate control over the periodicity. We experimentally validated the photonic properties, reflectance and slow light-induced absorption enhancement, of these systems by showing an outstanding agreement with simulations (figure 5). Interestingly, the existence of numerous photonic band gaps creates a structure where the stop-bands can merge or split at increasing angles (figure 4). Surprisingly, we observed that the phase matching condition (equation 1.6 from the manuscript), which provides the solutions for the Bragg reflectance, seems to break down under a complex refractive index. Under this situation, a numerical solution offered a better fit, as concluded by comparing figure 1 (d) to figure 5 (b).

Finally, we used the fluorescent properties of the J-aggregate dye to study the impact of the photonic environment on emission. We analysed this interaction in two ways. First, we observed a decrease in the photoluminescence at the central emission wavelength due to the interaction between the emission with the photonic band gap. Second, we noted a decrease in photoluminescence excitation when the incident light wavelength matches the stop band of the structures.

USC UNIVERSIDADE DE SANTIAGO

6.2.1 Conclusions and comments

The initial aim of this work was to create a biomimetic structure of iridoplasts. From here, we extracted several conclusions:

- J-aggregates can be used to dope the organic unit cells to increase the photonic strength and to create a multi-stopband system.
- We demonstrated slow light absorption enhancement in an all-organic system, which also was also analogous to the iridoplast.
- These properties can be tuned by changing the thickness of the non-absorptive layer.

However, further research on these structures is needed to answer fundamental questions, such as how the emission properties are affected by the photonic mode. From an applications perspective, the work points towards several interesting applications, particularly by reducing the TDBC concentration in the absorptive layer, and nanostructuring the system.

The results shown in figure 6 (a) demonstrate that the photonic environment of the structures can directly affect the emission of the system by attenuating this. Because at higher angles the photonic band gap blueshifts, this dampening is expected to blueshift as well. Therefore, the angle-dependent emission of a system excited at a fixed energy could help study the properties of the system by making a clear connection between the photonic environment and the emission of the dye. In fact, the angle-dependent properties of photonic cavities have been observed to attenuate the photoluminescence of TDBC [267].

In this publication, we have used high concentrations of TDBC in our absorptive layers. Therefore, a highly absorptive PhC is achieved. Depending on the application, this might not be desired. Lowering the concentration would decrease the Lorentz strength of the oscillator (equation 1.14 of this dissertation) and consequently the absorption of the films. For that reason, a similar study could be done for structures with lower TDBC concentrations to investigate the properties and potential applications. In addition, lower concentrations would generate refractive indices that more closely match that of the thylakoid membranes.

The biomimetic structure fabricated here presents quasi-infinitely wide dimensions on the plane. In the natural system, the lateral dimensions range between 5 and 10 μm, meaning that there might be lateral confinement of the light waves in the structure. In addition, iridoplasts tend to aggregate in groups, with a distance of 5-10 μm between each other [117]. This short distance between them might create light interactions. This requires further experimental and theoretical analysis. This can be achieved by nanostructuring the dye-doped photonic crystal and it can also be extended to create further photonic properties. Preliminary results in nanostructuring these systems are presented in chapter 7. This study, therefore, opens the door to further development of bio-inspired technologies for light manipulation [78].

Additionally, to obtain a fully biomimetic structure, light-dependent morphological changes are desired. Photosensitive polymers have been widely studied due to the induced reversible changes in chemical and physical properties such as shape, wettability, solubility, optical properties, conductivity, and adhesion [268, 269]. Photosensitivity has been used to induce patterned refractive index changes in systems, producing photonic crystals, such as fibre Bragg gratings [270], high-quality cavities [271], and even 2D and 3D structures [272, 273]. However, in all of these cases, the changes were permanent and non-reversible, constraining the applications. Interestingly, azobenzene-containing polymers can provide a solution since

they are known to reversibly change their topography. Doping Poly(methyl methacrylate) (PMMA) with this compound has been shown to cause an expansion between 10 and 20% under blue light and reversibly contract under UV light exposure [274]. Using this principle, a reversible and controllable optical grating pattern was demonstrated by the same group [275]. In both studies, lasers were used to induce changes in the thickness of the polymeric material. Additionally, this compound is transparent, allowing for the implementation of photo-responsive PhC.

Interestingly, PMMA has been previously used to create multilayered photonic structures [230]. Indeed, spin-coating PAZO (azobenzene-containing polyelectrolyte) and PMMA structures were demonstrated to create high-reflectance Bragg mirrors. Additionally, light exposure was shown to tune the Bragg reflectance by 20 nm [232]. A similar implementation can be translated to the structures presented here, creating a full iridoplast biomimetic structure with light-intensity tunable absorption enhancement. Alternatively, morphological changes could be induced by other external factors, such as swelling by the presence of organic solvents [230, 276], thermo-expansion [277], or electro-sensitive polymers [278].

Finally, the strong dispersion produced by the exciton creates two distinct regimes: Near-Zero Index (NZI), between $550 < \lambda < 585$ nm, and a high index, between $595 < \lambda < 650$ nm. NZI bulk materials provide exotic properties such as super-coupling [279], directive emission control [280], photon tunnelling [281], and extreme nonlinear interactions [282]. Thanks to these, the literature on NZI materials is extensive [283, 284] and TDBC-PVA could be used as a new material for these applications. Surprisingly though, research on high-index dielectric materials, is extremely scarce, despite its importance. Thanks to the increased refractive index contrast these materials provide, the enhancement of the properties of photonic crystals (such as wider band gap) [285], highly efficient low-loss metasurfaces [286] and smaller foot-print photonic integrated circuits [287] can be achieved. Interestingly, Jacob Khurgin has recently stressed this importance and has proposed a "call for action" to create higher refractive index systems based on condensed-matter first principles [288].

Lorentzian oscillator materials, such as TDBC-PVA, are typically used for NZI [284] but never have been so for high index. In this paper, we have shown an index as high as $n = 3.4$, above that of most dielectric materials in the VIS [289]. However, note that, at the wavelengths with the highest index, absorption is significant, rendering the increase ineffective, since transparent materials are usually desired. Despite this, note that an increase is persistent (albeit weaker) for higher wavelengths where absorption is negligible: $n_{PVA} = 1.48$ and $n_{PVA-TDBC} = 1.86$. This increase will be higher for stronger excitations strengths. Therefore, TDBC doping simultaneously yields these two effects. In this chapter, we have observed the advantages of a higher and a lower index, which yielded increased refractive index contrasts. In the next chapter, we'll observe another application from the lower index, which provides metallic-like optical properties and hence support polaritonic states.

The J-aggregate used and fabrication techniques developed allow the replacement of both metals and other inorganic materials used in PhC, creating all-organic photonic structures and demonstrating the feasibility of organic 1D photonics [232]. This produces advantages such as flexibility, lower financial cost and lower environmental impact. In the following chapter, we demonstrate an application of an all-organic structure, using the polaritonic properties of this material and the fabrication techniques developed here.

USC UNIVERSIDADE DE SANTIAGO DE COMPOSTELA

6.3 All organic Tamm state

The strong dipole moment created by the high concentrations of TDBC generates a strong refractive index dispersion, ultimately leading to the formation of a region where the real component of the permittivity becomes negative. Under these conditions, the material presents optically metallic-like properties. This range is also known as the Reststrahlen region [290] and these properties allow the replacement of metals for certain applications, such as in optical antennas [158], polariton sensing [148], and Optical Tamm States (OTS) formation [159]. Tamm states are confined light modes formed at the interface between two highly reflective structures, typically a DBR and a metal [70] but also two DBR [291]. Despite the existence of one single example where researchers use organic material to substitute the metal film in the creation of OTS [159], the system continued relying on inorganic materials to form the DBR. For that reason, the system did not present many of the aforementioned advantages of all-organic photonic structures. Note that, despite many authors naming these states as Tamm plasmon polaritons [292, 293], or just Tamm plasmons [210], we avoid using these two terms since Tamm states neither require a plasmon to exist nor do they correspond to a polaritonic state.

While working on the biomimetic system, many fabrication techniques were developed which allowed expanding our work onto technological applications. We start by creating a fully organic structure which sustains Tamm modes and demonstrates the possibility of tuning this state. This work was published as a paper, entitled "Tunable narrowband Excitonic Optical Tamm States enabled by a metal-free all-organic structure".

For this study, we use an all-polymer DBR and a TDBC-PVA film stacked on top of each other to obtain the two reflective structures needed to form an OTS. Organic photonic crystals are typically avoided for applications, not only because of the fabrication hurdles (particularly the lack of precision) but also due to the small refractive index range they present. Consequently, the refractive index contrast between any two polymers will be small, relative to inorganic options, and the photonic strength will therefore be weak, which is typically a drawback for most applications of photonic structures. In addition, the FWHM of the photonic band (and consequently the highly reflective region) will also be narrower, according to equation 1.8 of the dissertation.

Compounded with the fact that the highly reflective region of TDBC-PVA is constrained to a small wavelength window, means that an overlap between the two high reflectivity regions, and hence an OTS, can only exist at restricted momenta. This is made clear in figure 1 (c) where the high-reflectivity regions of the structures are shown to overlap only for a specific momenta range. Interestingly, this constraint can be seen as an advantage since, by slightly varying the period of the PhC, the momenta range the Tamm mode exists can be as well tuned, as suggested from the figure.

In this paper, we developed a theoretical framework for the existence of OTS in all-organic structures and demonstrated the possibility of tuning in momenta this mode. Using the techniques developed for the biomimetic system, two systems containing the OTS were fabricated. Experimental measurements on the individual substructures (TDBC-PVA films and DBR) and the full systems showed a clear dip in reflectance (figure 2), which is characteristic of OTS. The experimental evidence presented an outstanding agreement with the theoretical predictions. Importantly, this dip is was demonstrated to exist at specific momenta of incidence of light depending on the period of the DBR.

This dip is a consequence of the light confinement at the interface of the structures which ensures strong light-matter interactions. Due to the dispersive nature of TDBC-PVA, confined light becomes, therefore, nearly entirely absorbed. We measured photoluminescence excitation as an indirect way of studying the absorption of the system and observed a nearly 80% photoluminescence enhancement from the OTS. If the conditions did not match the ones necessary to have this state, photoluminescence was similar to a single layer of TDBC-PVA.

6.3.1 Conclusions

With this work, we expand the applications of the J-aggregate by demonstrating the first all-organic OTS sustaining structure. The system presented here introduces advantages in two different dimensions. Firstly, compared to the more commonly used inorganic materials, the organic system allows for flexibility, lower financial cost, and lower environmental impact. Secondly, the narrow momentum band of the Tamm modes provides momentum sensitivity for the structure. Photoluminescence measurements confirmed the presence of the Tamm mode and can be potentially explored in future work. However, the absorption of TDBC-PVA will affect the distance the mode can propagate and hence its utility in a practical application. Studies are needed to investigate how far OTS can propagate at the interface of the J-aggregate. We should also add that OTS present an advantage over plasmons since the mode is independent of polarisation, whilst SPP can exist only under p-polarised light.

It is also worth commenting that, similar to what has been discussed in the previous section, externally induced expansion/contraction of the photonic crystal could provide a highly momenta selective OTS-containing structure. Moreover, from an application perspective, the polaritonic properties of TDBC-PVA open many other doors in diverse topics, in addition to the metal replacements suggested before. For example, they can be used to create cavity exciton-polaritons [294], that traditionally rely on semi-conductors to generate the exciton [295, 296], which have promised to create the next generation of integrated circuits and optoelectronic devices [297–299], population inversion-free lasing [300], and efficient exciton energy transfer systems [301]. The results presented in this publication start cementing the feasibility of using organic materials for photonic and polaritonic applications. In the following chapter, we go one step further by showing the preliminary results of nanostructuring in organic material.

USC UNIVERSIDADE DE SANTIAGO DE COMPOSTELA

USC
UNIVERSIDADE
DE SANTIAGO
DE COMPOSTELA

CHAPTER 7

Nanostructured photonic crystals

This dissertation follows two main research lines. The first develops the study of the photonic properties of iridoplasts. The second expands the fabrication techniques developed in the first line towards novel all-organic photonic structures. In this chapter, we'll briefly introduce two sets of unpublished results. They correspond to the 2D and 3D nanostructuring of photonic systems. In particular, we aim to obtain lateral confinement of the optical properties of the 3D iridoplast biomimetic multilayer by reducing its lateral dimension to the same dimensions as the ones observed in the biological system. By experimentally measuring the photonic properties of this system, we found no evidence of lateral light confinement in the structure. Moreover, we demonstrate the possibility of coupling the Surface Exciton Polariton (SEP) of TDBC to the grating modes, allowing the observation of this polariton at momenta lower than the light line. The substrate used to produce the grating is a flexible polymer, making the full system free-standing.

7.1 Laterally confined iridoplast biomimetic

7.1.1 Introduction

So far, we have taken a 1D approach to theoretically and experimentally study the properties of photonic structures. As a consequence, guided modes are not laterally confined and are therefore equivalent in all in-plane directions. This can be assumed to be true when the lateral size of the PhC is much larger than the working wavelengths and/or than the depth of the crystal. This is not necessarily true for iridoplasts which, since they are confined on all sides, present a structure equivalent to a micropillar [302]. To predict the light confinement caused by this nanostructuring, effective index approximations of the PhC have been shown to present strong agreements to 3D numerical calculations [303]. Under this approximation, the pillar can be seen as a system analogous to a fibre. Therefore, one can intuitively conclude that, as we reduce the lateral size, light incident at an angle below the critical angle between the structure and the surrounding medium (or, analogously, above the numerical aperture of the fibre) will leak away from the structure. In this approximation, despite some efforts [304, 305], an analytical model for the prediction of the confinement behaviour is still lacking.

Lateral confinement of light has been mostly used to either control the quality factor of λ cavities and reduce the volume in micropillar structures [305–309] or to limit Tamm modes to

near normal incidence by making the top metallic reflector into a small disk with a diameter smaller than 10 μm. The latter has been suggested to help control spontaneous emission to normal incidence modes and to reduce the laser threshold [209, 210, 310, 311]. For this reason, the spatial confinement of photonic band gaps is also expected to occur by limiting reflection to normal incidence, even though this has never been observed. Therefore, it is reasonable to hypothesise that iridoplasts might have similar light confinement properties. This could have consequences on the photonic properties such as the enhancement of light absorption by slow light at normal incidence only and the prevention of structural colouration at high angles. A straightforward method to observe light confinement in a Bragg mirror is to measure the angle-dependent reflection since the reflection band is expected to become attenuated at high momenta. Even though it's possible to measure this directly on iridoplasts [1], the rough character of the natural photonic crystal makes the angle-dependent features unclear. For that reason, we use the biomimetic structures fabricated in chapter 4 to develop a full 3D system with similar lateral dimensions.

Photobleaching of dyes occurs under an excessive amount of light and is typically considered a limitation since it represents an irreversible attenuation of fluorescence and absorption, resulting in a change in the optical properties of the material [312–314]. The modification of these properties manifests themselves in the change of the refractive index and this can be taken advantage of to create 2D nanostructures without having to destroy or remove material; examples include gratings [315, 316], nanodisks to concentrate light radiation [317], and integrated optical devices for an increased refractive index contrast [318, 319]. To fabricate a 3D biomimetic iridoplast, we nanostructure the organic multilayers from chapter 4 made of Polystyrene (PS) and TDBC doped PVA, using laser writing techniques to photobleach TDBC around a non-bleached pillar, as demonstrated in figure 7.1. Note that, ideally, this pillar would have circular symmetry, however, this is not possible to achieve with the fabrication method used. The pillar is formed only by the refractive index contrast of the regions instead of morphological changes. Previous studies where the same technique was used on the same J-aggregate dye found that the absorption and emission can be entirely removed with this method, suggesting a total destruction of the excitonic properties. However, a complete picture of the optical properties, such as the refractive index, has not yet been demonstrated [320].

7.1.2 Fabrication and characterisation

A 532 nm green laser from the Witec Alpha300 R confocal Raman microscope is used to photobleach the dye. Using the highest magnification objective lens available in this tool (50x), a spot with ~ 1 μm in diameter is achieved. The piezo-driven scanning stage of this tool allows a ~ 2 μm resolution, providing extremely accurate patterns. Since we aim at destroying the excitonic properties of TDBC by photobleaching the dye, optimum patterning conditions are achieved to allow enough energy to photobleach rapidly whilst not disintegrating away the organic material. These conditions were achieved in three ways. First, the high-energy laser (532 nm) is used instead of the low-energy one (633 nm) so that the energy of the excitation laser line is higher than the energy of the absorption peak which would yield the most efficient photobleaching. Second and third, we found a compromise between the power of the laser and the scanning speed. The speed of the stage was set to 0.1 μm/s and the power of the laser used was selected to 0.2 mW. Excessive laser energy

USC UNIVERSIDADE DE SANTIAGO

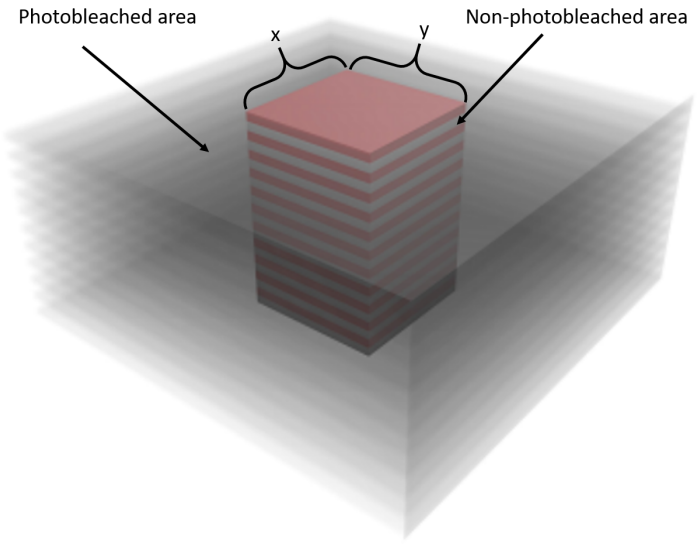


Figure 7.1: **Schematic 3D biomimetic structure**. Red coloured slabs correspond to the TDBC doped PVA and the dark grey correspond to the PS. The transparent area corresponds to the photobleached area. We aim at structuring x and y in dimensions similar to those of iridoplasts: $1 \rightarrow 10$ μm.

will cause unwanted heating in the system which spreads laterally, effectively increasing the photobleached region, despite the small laser spot. The given power of the laser was set taking this effect into account, to make the photobleached area the same as the laser spot area. As a consequence of this, the multilayered sample is not fully bleached by the laser if it passes one single time. For that reason, we repeat the pattern 15 times to ensure a fully bleached sample.

First, we want to evaluate the effectiveness of photobleaching. We define the three distinct refractive indices: for PS, n_{PS}, which is unchanged by the laser, and for TDBC-PVA before and after photobleaching, n_{TDBC} and $n_{bleached\,TDBC}$ respectively. We use the sample Δ_2 from chapter 4 because it presents the photonic gap at $\lambda \sim 480$ nm, similar to the iridoplast. Initially, we photobleach a squared area (not what is represented in figure 7.1) to study the photonic properties of bleached areas. In figure 7.2 (a), we show epi-illumination images of the squared area that has been photobleached a different number of times: 5, 10 and 15; a clear decrease of the coloured spots is observed. The size of the square is 50 μm, large enough to avoid lateral confinement. To evaluate the effectiveness of the bleaching, we measure the reflection properties of the bleached area (red circumference) and compare it to a non-bleached nearby area (black circumference). We use the oil immersion objective lens with 100x magnification, described in section 2.3, and a 400 μm diameter fibre to couple light from the initial lamp. This provided a spot with 16 μm diameter. The oil immersion lens is necessary to measure the following structure and we, therefore, decided to use it here as well for consistency.

Figures 7.2 (b) and (c) show, respectively, the angle-resolved and normal incidence reflectance measurements of the two spots shown in the far right of subfigure (a). In the non-photobleached area measurements, the results are similar to the ones presented in chap-

ter 4, with the exception that angles beyond the light line, represented by the high reflectivity region, are now captured. Moreover, the normal incidence Bragg reflection peak is centred at $\lambda \sim 450$ nm instead of $\lambda \sim 480$ nm, as before, because this measurement was done closer to the edge of the sample which, as we explained in section 2.2, presents a reflection wavelength peak at higher energies. Under these conditions, the photonic properties become similar to sample Δ_1. The dope-free photonic response of this structure is simulated in figure 1 (c) of chapter 4, where a clear Bragg reflectance peak is observed, albeit weaker. However, structural reflectance is not seen in the photobleached area and instead and we observe only Fabry-Perot oscillations. Despite this, full photobleaching has been achieved, supported by the fact that reflectance is ~ 100 % beyond the air light line in the high absorbing region ($580 < \lambda < 600$ nm), contrasting with the non-photobleached spot.

The reasons for the difference between measured and predicted reflectance response remain to be investigated, though we hypothesise two different origins. The first is that, after destroying the excitonic properties of the TDBC, the refractive index of TDBC-PVA ($n_{bleached\,TDBC}$) doesn't become that of pristine PVA, but rather slightly higher, close to the refractive index of PS, making $\Delta n = |n_{bleached\,TDBC} - n_{PS}| \sim 0$. Here, we effectively end up with no periodicity and hence no PhC. The refractive index of bleached TDBC-PVA could not be found because an unpractical amount of time ($\sim$ days) is needed to photobleach a large enough area to make the ellipsometry measurement possible. The second hypothesis is that the power of the laser raises the temperature above the transition point, making the polymers fluid and mixing the PS and TDBC-PVA together. This would, again, remove the periodicity and hence the photonic properties of the structure.

AFM measurements showed no change in the height (figure A.6) between bleached and non-bleached areas and hence the possibility that the laser might have removed the polymers is excluded. For this reason, regardless of what is causing the destruction of the Bragg reflection in the photobleached areas, we are obtaining what we initially aimed at: a technique by which we can nanostructure by refractive index, not morphological, differences.

7.1.3 Laterally confined photonic structure

Despite the consistency in the periodicity among iridoplasts of the same species of plants, their lateral dimensions can differ within a small range. In *Begonias*, some species exhibit iridoplasts with lateral size as high as 10 μm, whilst other species present as low as 3 μm [1]. For that reason, we fabricate two nanostructured systems (A and B) with similar dimensions. The schematic is shown in figure 7.1, and the lateral dimensions are $x_A = 3.5$ μm and $y_A = 5.3$ μm and $x_B = 4.9$ μm and $y_B = 2.2$ μm. Experimental images are seen in figures 7.3 (a) and (b). Considering the photonic properties and the lateral dimensions of the multilayer, these systems represent a fully 3D biomimetic system of iridoplasts.

To assess the light confinement within these systems, angle-resolved reflectance was measured. The conditions here are the same as in the previous sub-section, with the exception that the fibre diameter used was reduced to 25 μm to provide a spot with 1 μm in diameter, allowing for the measurement within the 2D nanostructured system. Figures 7.3 (c) and (d) show these measurements for systems A and B respectively. Note that, the reduced size of the diameter of the fibre results in a significant reduction of light intensity reaching the sensor (by a factor of $(25/400)^2 = 1/256$), lowering the signal-to-noise ratio of the measurement and hence reducing the quality. Both samples exhibit indistinguishable features compared

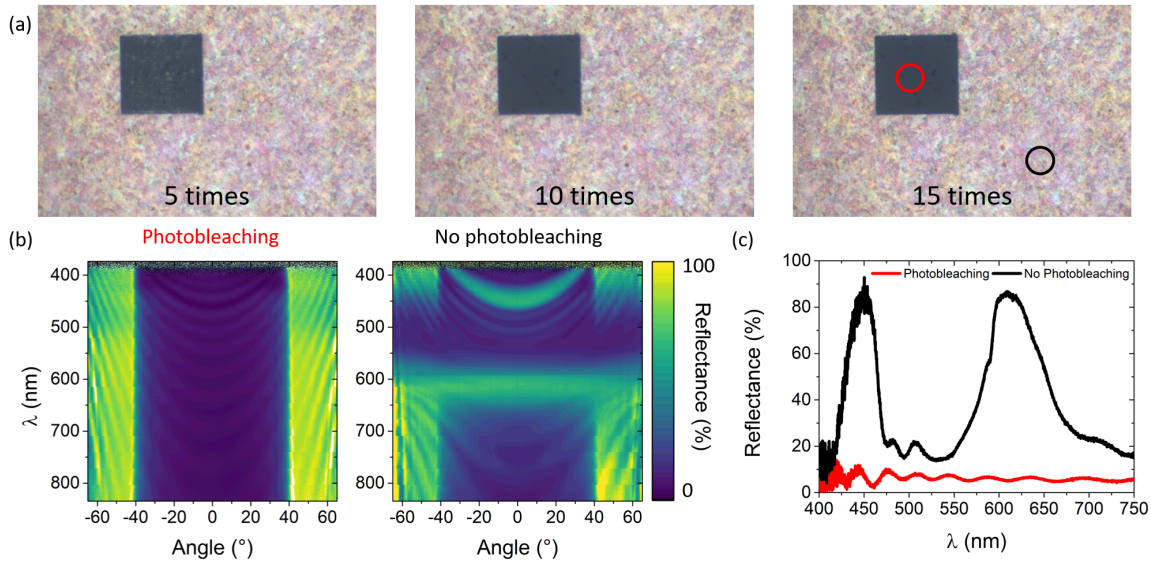


Figure 7.2: **Photobleaching dye doped DBR**. (a) Sample Δ_2 from chapter 4 is photobleached on a squared area with a size of 50 μm. The same area was photobleached 5, 10, and 15 times to ensure full photobleaching. Red and black circles correspond to the areas measured under s-polarised angle-resolved reflectance, shown in (b). (c) Cross-section at normal incidence of the angle-dependent reflectance measurements.

to the non-structured case given in figure 7.2. Structure B presents a slightly weaker Bragg reflection. This is likely a consequence of lateral leakage of the heating created by the laser during the photobleaching process; consequently, there could have been significant bleaching in the region we did not wish to affect. This was more significant for this structure due to the extremely narrow size.

The lack of angle-constrained features suggests that, in reflection, there is no light confinement within these structures. However, this represents only the first experiments of this ongoing work. Three key steps are required to proceed. The first is to make 3D optical simulations of the photonic system using finite method FDTD programs such as Lumerical [321]. From here, we can evaluate the accurate distribution of the electromagnetic field inside the system and infer any effects on the optical properties. Second, the angle-resolved photoluminescence of the system should be measured to evaluate indirectly the effect on the light absorption enhancement [210, 322]. The laser path included in our set-up, shown in figure 2.7, was constructed to perform these measurements, however, considering the size of the spot, we estimate that the integration time for such measurement would be within days. The dye would have been significantly photodamaged long before one measurement could be taken. For this reason, we couldn't perform this measurement. Finally, it is also worth demonstrating confinement to lower angles of the micropillar by continuing to reduce the lateral size since this presents many technological applications. The light confinement can be used for efficient spontaneous emission coupling in 3D cavities [323, 324], vertical-cavity surface-emitting lasing [325–327], or all-optical switching devices [328]. Compared to previous studies, this would be the first time, to the best of our knowledge, that a micropillar was fabricated without the removal of matter. This technique could also be extended to the OTS

USC UNIVERSIDADE DE SANTIAGO DE COMPOSTELA

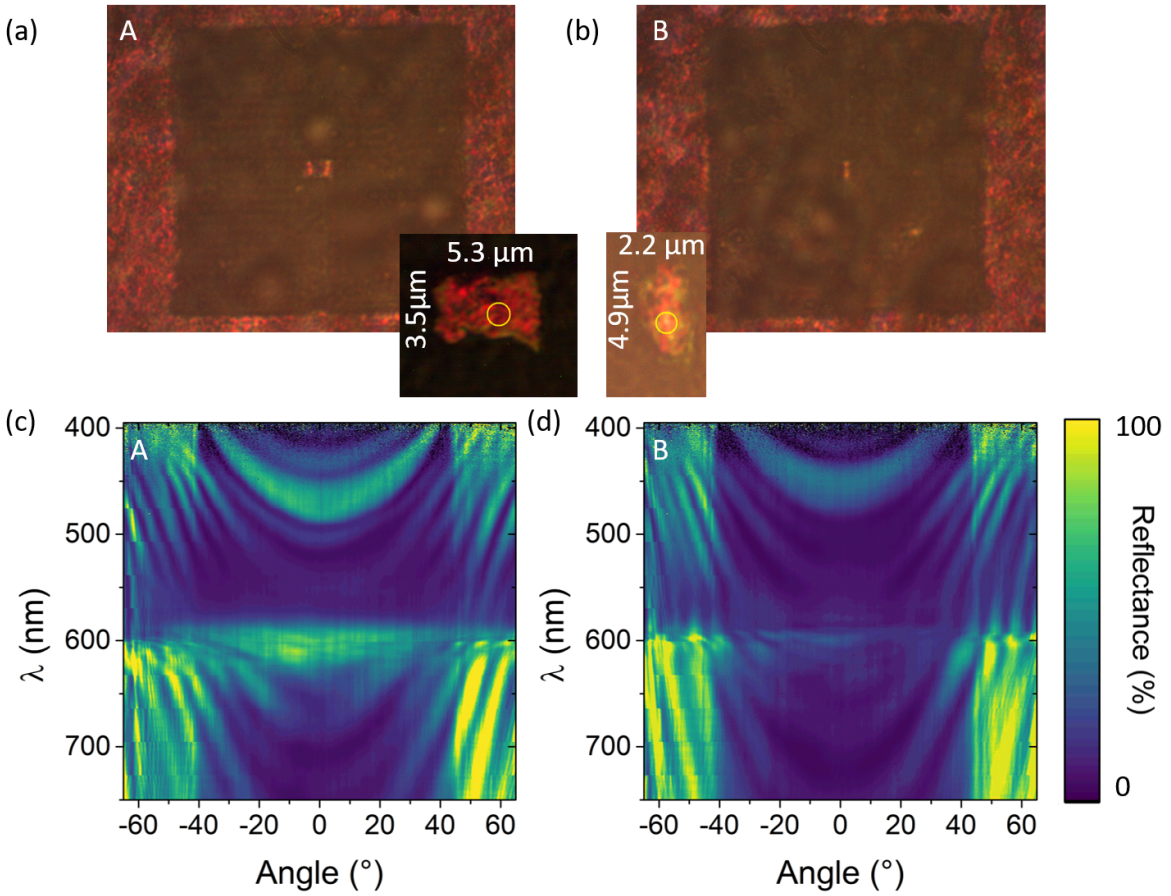


Figure 7.3: **Nanostructured dye-doped DBR**. (a) and (b) are Epi illumination images (40x objective lens) of the two 3D nanostructured systems. Insets show a close-up of the system (100x objective lens) and its dimensions; the yellow circumference represents the area measured. (c) and (d) show the angle-resolved reflectance measurements of the spots.

structures fabricated in chapter 5 to fabricate confined Tamm states [209, 210].

7.2 Wrinkled TDBC-PVA as a grating system to access Surface exciton polaritons

7.2.1 Introduction

In section 1.4, we showed that Surface Plasmon Polariton (SPP) and Surface Exciton Polariton (SEP) exist only beyond the light line, making the use of complex methods to match to higher momenta necessary. These include a prism [184, 185] or an oil immersion lens [187, 188]. Despite the complexity of these techniques, they allow the observation of the polariton on a single film. In contrast, gratings require further structuring of the photonic system but the measurements can be done using an air high numerical aperture objective lens [183, 186]. This is possible thanks to incident light scattering, described in equations 2.17, where incoming light gets scattered along the surface at angles below the critical angle, matching

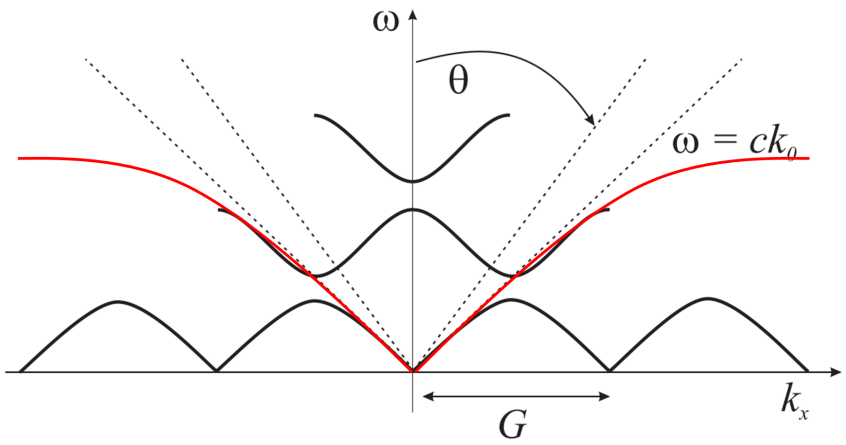


Figure 7.4: **Dispersion relation**. Folding of an SPP propagation curve on a metallic diffraction grating [175]. The red lines correspond to the SPP of a single film with no grating structure.

the same momentum. Consequently, the surface states in the same propagation direction are excited with wavevectors multiple of $\pm G = 2\pi/\Lambda$, with Λ being the periodicity of the grating [329], as shown in figure 7.4. Note that a gap opens where different scattered SPP modes cross. This can be seen as another strong coupling effect, though it is beyond the scope of this work [330]. Despite the extensive literature on the coupling between SPP and the grating modes, particularly in gold [331–333], this has never been observed for the excitonic counterpart: SEP. Interestingly, gold gratings have been used to observe the hybrid strong coupling mode between the SPP of gold and the molecular exciton of TDBC-PVA [198] and transition metal dichalcogenides [334]. Varying the period of the gold grating enables a tuning design parameter to the system [335].

The fabrication of the grating structures, however, requires intricate techniques. For example, some of the most common techniques are laser interference lithography on silicon substrates [336], Mach-Zehnder interferometer to photo-reduce gold ions periodically [337], nanoimprinting [338, 339], reactive-ion etching onto a photoresist on a silica substrate [340], e-beam lithography [341], and Lloyd's mirror interferometer [342]. PDMS substrates have also been used to create gratings, using holographic laser beams, providing flexible, stretchable, and tunable systems [343, 344]. In fact, the elasticity and high thermal and chemical stability of PDMS make it attractive for alternative grating fabrication processes which use less complex machinery than the previous methods. For example, commercial CDs (compact discs) and DVDs (digital video discs) have been used to nanoimprint on PDMS substrates [345]. Interestingly, in 1996, the spontaneous formation of grating-like structures on PDMS was first suggested [346]. In this work, the authors deposited metal films onto a flat PDMS substrate which was at a thermally-induced expanded state. The subsequent cooling of the polymer leads to the contraction of the substrate but not of the metal layer. The tension that the substrate applies on the stiff metal layer makes this top film wrinkle, creating a grating-like structure. This method requires, however, the use of complex tools to deposit the metal layer. For this reason, we can alternatively have the thermally expanded PDMS substrate undergo an oxygen plasma treatment to create a silica-like hard layer on top [347], replacing the metal film [348]. To simplify further the process and provide higher control over the fabrication, the contraction can be induced by releasing a mechanically pre-strained PDMS substrate

[349–351].

Using this fabrication technique, gold deposition on the wrinkled system has been shown to couple the SPP to shorter momenta [352]. Similar wrinkle fabrication methods have been used for several other implementations. Examples include the increase of internal light scattering in solar cells and subsequent higher light capturing efficiency [353], anisotropic surface wetting [354], micro-lenses array formation [355], and metrology for thin film mechanical properties [356]. In this section, we expand the applications of this fabrication technique by developing a methodology where we create TDBC-PVA gratings whicThe strained structure undergoes an h replicate SEP to angles below the ai light line. We start by explaining the fabrication of the system without TDBC-PVA film and demonstrating tunability capability. We proceed by topologically and optically characterising the structure. We then repeat this characterisation for a system with a TDBC-PVA film deposited on top, allowing the observation of the polariton mode below the air-light line.

7.2.2 Fabrication methodology and theoretical background

The fabrication methodology developed in this work is schematised in figure 7.5. For wrinkled PDMS, we divided this into four steps (a to d) and for wrinkled TDBC-PVA, one extra step is added (a to c, e, and f). In the first step (a) we fabricate the PDMS substrate with a consistent thickness. PDMS (Sylgard 18, Dow Corning) with a curing agent, mixed in a 10:1 weight ratio, was deposited onto a Petri dish, followed by cross-linking in an oven for 2 hours at 60°. The substrate is extracted from a rectangular section (10 cm by 2.5 cm) of the Petri dish and is placed on a glass holder for support. The polymeric substrate is strained by $\epsilon = \Delta L/L$, where L is the original length and ΔL is the amount stretched. To fix the strain, the polymer surface is clamped onto microscope slides, demonstrated in subfigure (b). Even though a stretch apparatus provides more accurate applied strains, the use of clamps to physically retain the stretched substrate is necessary to allow spin coating on this system.

The strained structure undergoes an oxygen plasma treatment (Gatan plasma cleaner) (c), creating a silica-like layer (SiO_x) with thickness h which depends on the exposure to the plasma [357]. For consistency, we keep all the parameters of the plasma cleaner constant and use only the exposure time to control the thickness of the layer formed. From here, the strain can be released (d) to create a simple PDMS grating where the diffracted reflected light can be observed by the naked eye. Alternatively, we can take the system to the spin-coater (e) to deposit TDBC-PVA and, once the solvent has evaporated, release it (f) to obtain the TDBC-PVA grating. Note that, despite the high hydrophobicity of PDMS [358], the silica-like surface of the substrate becomes hydrophilic as a by-product of the oxygen plasma, allowing the adherence between the substrate and the organic film.

The wrinkle formation of a hard thin layer on a soft material is created by the destruction of the planarity of the film under the buckling instability that relieves the strain of the compressed layer. For this reason, wrinkles are created along the direction of the strain. Therefore, wrinkles can be formed in more than one direction at the same time along the plane and, for example, square patterns can be created. However, we will only be focusing on a uni-dimensional sample [350]. Using linear buckling theory, the analytical solutions for the amplitude (A) and periodicity (Λ) of the wrinkles can be derived [359]:

USC UNIVERSIDADE DE SANTIAGO DE COMPOSTELA

$$\Lambda = 2\pi h \left(\frac{E_f}{3E_s} \right)^{\frac{1}{3}} \tag{7.1}$$

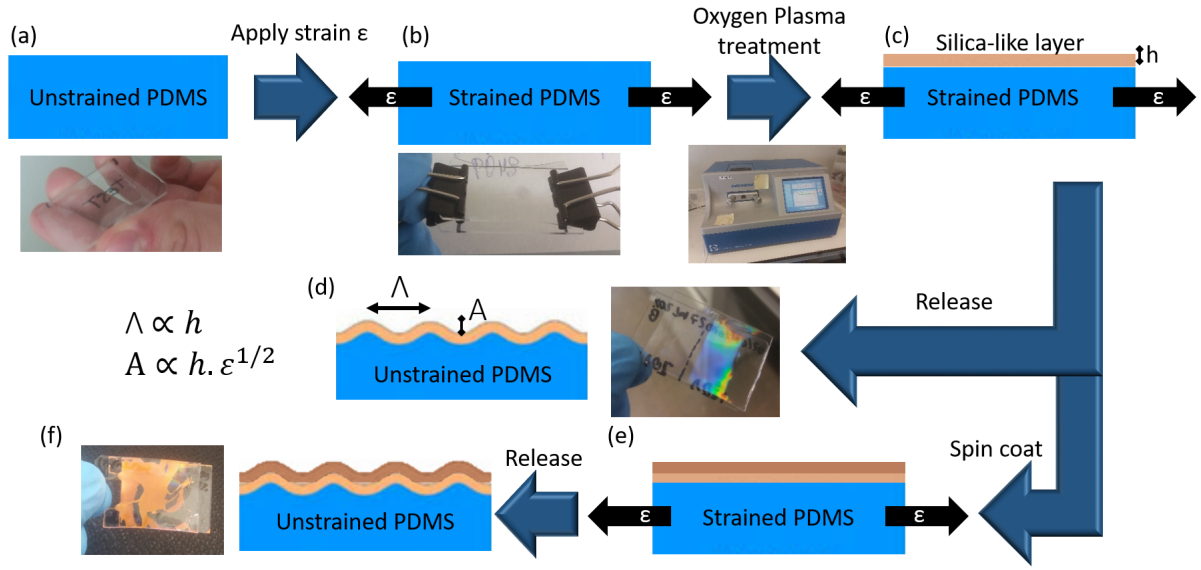


Figure 7.5: **TDBC-PVA grating fabrication methodology**. (a) Initial PDMS substrate, (b) straining it by ϵ and clamping, (c) oxygen plasma treatment. We can either release it (d) or spin coat TDBC-PVA (e) and then release it (f).

$$A = h\left(\frac{\epsilon - \epsilon_c}{\epsilon_c}\right)^{\frac{1}{2}}. \tag{7.2}$$

Here, E_f and E_s are the strain modulus of the film and the substrate respectively, and ϵ_c is the critical strain necessary to observe wrinkle formation. From all of these parameters, we can only control the thickness (h) and the strain applied on the substrate (ϵ). Ideally, we want to control the structure's periodicity whilst maintaining the amplitude of the system as high as possible. For this reason, we try to increase the strain to the maximum. Even though strains as high as 50% have been obtained on PDMS [360–362], higher strains will present more frequent defects. In this study, 20% was concluded to present an ideal compromise between optical properties and defects. Note that, despite the period being theoretically independent of the strain, increasing the strain on the samples has been found to decrease the period of the wrinkles [351]. Additionally, the thickness of the stiff layer is impractical to find. For that reason, much like spin-coating, we rely on an empirical method to control the period of wrinkles. We do this by varying the exposure time and measuring the resulting spacing between the peaks of the structure.

As a starting point, we analyse TDBC-PVA-free samples (following path (d) in figure 7.5) to investigate the feasibility of the methodology. We begin by calibrating the periodicity with plasma exposure on TDBC-PVA-free substrates. We use images taken with the optical microscope of the confocal Raman (SENTERRA) to perform a Fast Fourier Transform analysis and obtain the periodicity, as shown in figure 7.6 (a). In this example, the sample was exposed for 40 seconds in the oxygen plasma chamber, yielding a period $\Lambda = 850 \pm 20$ nm. AFM measurements of the wrinkles (subfigure (b)), confirm the periodicity of the samples and measure the amplitude to be $A = 170$ nm. From the cross-section, we see that the sample is extremely smooth. For smaller periods (at 5 seconds), this amplitude is nearly halved to $A = 100 \pm 10$ nm. For comparison, figure A.7 shows the example of a similar sample but strained 30 % instead of 20% where the wrinkles are clearly damaged. This was a frequent

occurrence for samples under strains $\epsilon > 0.2$.

To understand if the system produced could be capable of coupling the polariton, we analyse its optical properties by measuring the angle-dependent reflectance with the 40x objective lens. Figure 7.6 shows this measurement for the aforementioned sample. The optical behaviour is expectedly similar to the one shown in figure 2.10. Since the period of the wrinkles is larger, the diffraction becomes redshifted, allowing the observation of the second order more clearly within the VIS. Moreover, since the refractive index of the grating material does not present a strong contrast with air ($n_{PDMS} \sim n_{silica} \sim 1.5$), the system does not have a strong reflectance (maximum $\sim 3\%$). Consequently, the features are not as clear and the measurement isn't as clean (low signal-to-noise ratio). The reflectance observed near normal incidence is caused by the internal back reflection of the objective lens used[1]. In addition, since the substrate is flexible, the sample isn't perfectly flat, creating asymmetries in the measurement. Despite these, the optical response of the system is clear and we, therefore, expect it to be able to couple to the polariton if similar conditions can be reached in the excitonic system.

Having shown the feasibility of the fabrication methodology, we demonstrate the possibility of tuning the period (Λ). We calibrated the periods for exposure times of 5, 10, 20, 40, 60, and 120 seconds, shown in the box chart figure 7.6 (d). In this plot, each point corresponds to a distinct image taken, similar to subfigure (a). Each sample fabricated was measured on three different spots. The consistency of the periodicity between the different samples under similar conditions is outstanding, allowing for accurate and precise tuning of the period, similar to what has been previously achieved in the literature [362].

7.2.3 Results

The deposition of the TDBC-PVA on the strained PDMS substrate is done by spin coating. The aqueous solution is similar to the one presented before: a 3:1 mixture of 6.0% wt. of PVA (Aldrich PVA Mw = 85000–124000) and 2% wt. of TDBC. This solution was diluted with water at a 1:1 volume ratio to yield a smaller thickness so that it could wrinkle more easily. The spin coater speed was fixed at 2000 RPMs since, at higher speeds, the centrifugal force would remove the clamps of the system. Under these deposition conditions, we obtain a film capable of sustaining a SEP on a flat substrate, demonstrated in figure A.1. Therefore, we can expect that, if we are able to wrinkle this layer, we can have SEP coupled to lower momenta. To tune the polariton coupling, we spin-coated under these conditions over strained PDMS substrates with different oxygen plasma exposure times: 5, 20, and 40 seconds.

Despite numerous attempts for the different conditions, there was only one sample where the TDBC-PVA wrinkled with the compression of the substrate, at an exposure time of 40 seconds. The optical image of the sample, figure 7.7 (a), demonstrates a uniform structure. The area measured (yellow circumference) was selected to match the region where the colour is the greenest; we hypothesise that this corresponds to the strongest aggregation and, consequently, the strongest coupling strength (f_0, from equation 1.14). An AFM measurement of the sample, shown in subfigure (b), confirms that TDBC-PVA has been wrinkled with a period of $\Lambda = 960 \pm 20$ nm and gives an amplitude of $A \sim 100 \pm 15$ nm. The proximity of the period to the calibration and the amplitude obtained without this excitonic layer suggests that the

USC UNIVERSIDADE DE SANTIAGO DE COMPOSTELA

[1] This back reflection is the same as the one observed in figure 2.10. Since the reflectance of the sample is much smaller here, this effect is much more pronounced.

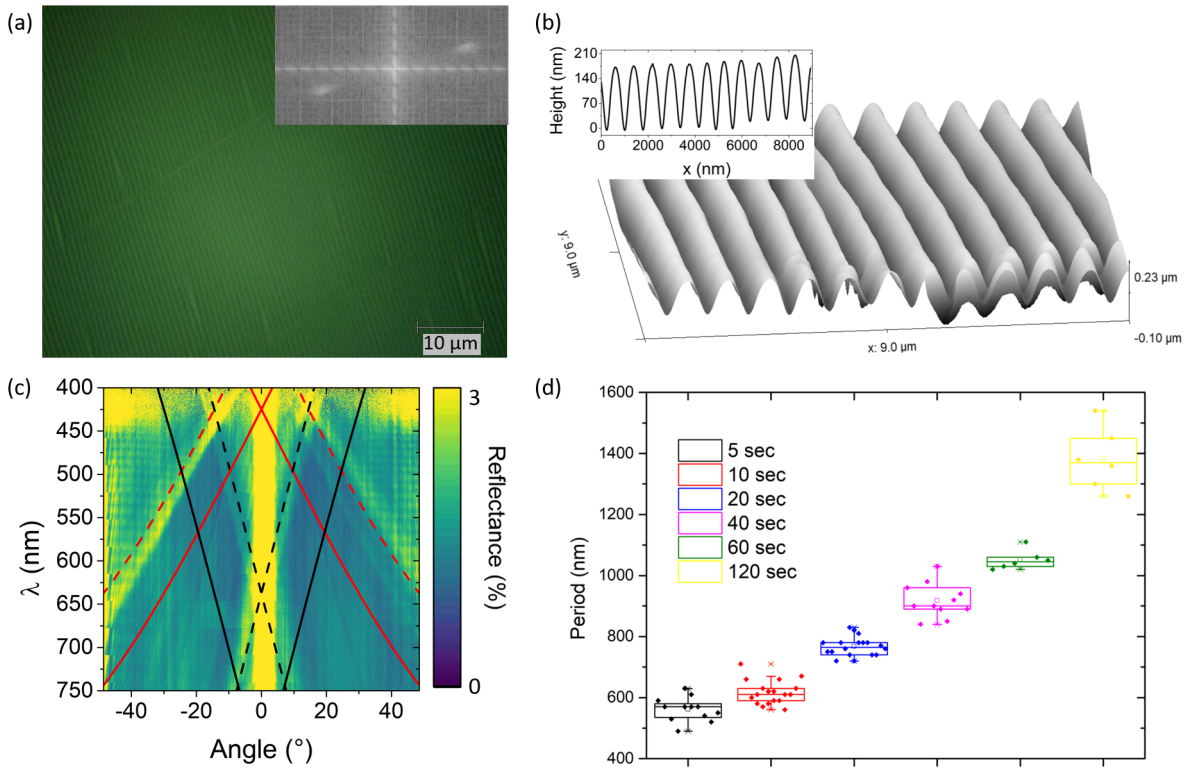


Figure 7.6: **Wrinkled PDMS analysis**. (a) Optical microscope image of wrinkled PDMS; inset is the Fast Fourier Transform of that image. (b) AFM measurements of the same sample. Inset represents the cross section. (c) Angle resolved reflectance measurement of the same sample. Exit (solid) and reentry (dashed) of light in the objective lens is seen for the first two orders of diffraction (black is the first and red is the second), according to equations 2.17 and 2.18. (d) Calibration of the periodicity of the wrinkles under different oxygen plasma exposure times. Horizontal line represents the median, white square represents the mean, and boxes contain between the 25 to the 75 percentile.

USC
UNIVERSIDADE DE SANTIAGO DE COMPOSTELA

effect of TDBC-PVA is negligible compared to the effect of the silica-like layer. However, one should note that the sample is much rougher than before (inset of subfigure (b), a characteristic of TDBC-PVA. Similar topological measurements were observed throughout the sample, not only at specific spots, demonstrating an outstanding consistency in this sample.

Subfigure (c) shows the angle-dependent reflectance of the structure for s- and p-polarised light. Note that we have switched from wavelength (λ) vs angle space to energy (E) vs momenta (k) space because polaritons are typically described in the latter space. Both polarisations present results similar to a single thin film, shown in figure 2 (a) from chapter 5, as expected from the negligible reflection of PDMS and the silica-like grating structure. For this reason, we mostly observe the high reflectance associated with the metallic-like region. A feature is noted in the reflectance dip at p-polarisation within the metallic-like region of TDBC-PVA at $k \sim 4.5$ μm. This dip fits the predicted polariton grating diffraction represented by the black dotted lines. For a more clear observation of this dip, we plot a cross-section for $E = 2.12$ eV ($\lambda = 585$ nm) across momenta, in subfigure (d). The two polarisations present similar reflections with the exception of the reflectance dip near the polariton. With these observations, we conclude that the SEP has coupled to the grating and has been excited to lower angles.

For comparison, figure A.8 shows one example for each oxygen plasma exposure time condition. The optical microscope images clearly show an irregular grating contrasting with what is observed in figure 7.7 (a). The AFM measurement shows irregular spacing between peaks and several bifurcations. Consequently, the SEP is not observed for any of the samples. Importantly, in areas of these samples where TDBC-PVA didn't spread (note that in figure 7.5 (f) some areas of the sample do not have TDBC-PVA), the structure presented similar wrinkles to the ones found on TDBC-PVA-free samples (see figure A.9 for a measurement in an area with no TDBC-PVA of a sample that has been spin-coated by it). This shows that the problem is with the TDBC-PVA film and not the underlying layers. The reason why, despite fabricating the samples in a consistent way, only one produced a grating structure remains unknown. It is expected that at lower oxygen plasma times the TDBC-PVA film doesn't adhere as easily due to not only the smaller period but also the smaller amplitude. The speed of unstretching the substrate plays an important role, which was accounted for. Other methods were unsuccessfully tried, such as the spin coating on an unstretched sample and further diluting the solution to create thinner films which might wrinkle more easily.

Nonetheless, we have demonstrated that SEP can be translated towards lower momenta from coupling to gratings. However, improvements are needed to fabricate this system consistently. Many measurements are required to understand how to achieve this. For example, we need to perform a more extensive study of the amplitude and periodicity under different time exposures with and without TDBC-PVA. Importantly, we need to understand why is it that the polariton only seems to appear in the aforementioned green areas. We hypothesise that these areas have either a bigger TDBC to PVA ratio or allow for more efficient aggregation of the J-aggregate. To obtain a better adherence of the TDBC-PVA film to the substrate, we can try to increase the ratio of PVA, since this polymer has better processability. However, this would make the polariton weaker and it could be found to be counter-productive. Alternatively, a different host polymer could be investigated. When successful, this fabrication technique will allow for both the straightforward monitorization of exciton-polaritons and, since no complicated or expensive machinery is needed, the low-cost and environmentally friendly fabrication of the structure.

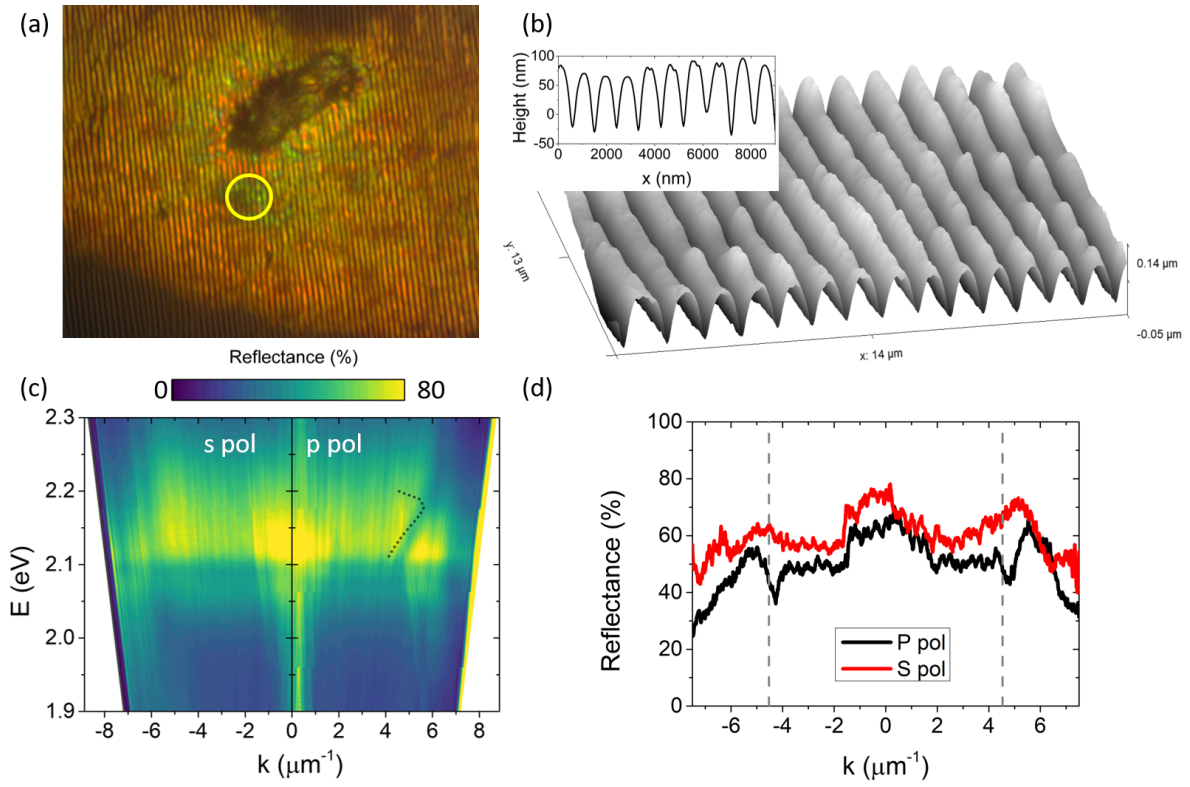


Figure 7.7: **Wrinkled TDBC-PVA analysis**. (a) Optical microscope image of wrinkled PDMS. Yellow circumference represents the area measured. (b) AFM measurements of the same sample. The inset represents the cross-section. (c) Momenta-resolved reflectance measurement of the sample at p- and s- polarisation. The dotted black line corresponds to the first-order polariton diffraction. (d) Cross-section of subfigure (c) at $E = 2.12$ eV.

USC
UNIVERSIDADE DE SANTIAGO DE COMPOSTELA

USC
UNIVERSIDADE
DE SANTIAGO
DE COMPOSTELA

Part IV

Conclusion

USC
UNIVERSIDADE
DE SANTIAGO
DE COMPOSTELA

USC
UNIVERSIDADE
DE SANTIAGO
DE COMPOSTELA

CHAPTER 8

Conclusion and future work

We began this dissertation by studying the photonic photosynthetic organisms known as iridoplasts. Their DBR-like structure provides this system with a bright blue reflection. Many biological advantages were initially hypothesised, such as producing a cue for pollinators [108], a photo-protective role, and an anti-herbivore effect [121]. However, since the photonic properties of this system have been experimentally and theoretically investigated in 2016 [1], the prevailing hypothesis has been that iridoplasts have evolved to enhance light absorption by slow light [111, 115, 117]. We theoretically investigated these properties and we found that iridoplasts absorb up to 4% more light than a standard chloroplast with the same volume of absorptive material and that, under high light conditions, this enhancement is negligible and the structural colour is redshifted via morphological changes. However, we concluded that, because of the negligible contribution to the total absorption of the leaf, slow light-induced absorption enhancement seems to be a highly unlikely biological function, despite the enhancement predicted on the individual system. In fact, we noted that, when considering the chloroplasts found underneath iridoplasts, the contribution to total absorption actually becomes slightly detrimental. Moreover, iridoplasts present the characteristic blue structural colour when they're under low light conditions where, in the natural environment, blue wavelengths are almost non-existent. When blue light is available to produce structural colour, we are found under higher light conditions (above the forest canopy) and the structure responds by expanding, resulting in the redshift of the structural colour.

In short, iridoplasts can reflect blue light when there's none to be reflected and they don't reflect blue light when these wavelengths are available. In addition, slow light-induced absorption enhancement likely doesn't play a significant role when considering the absorption of the whole leaf. Therefore, neither of the two properties seem to produce significant effects. These conclusions are equivalent to bizonoplasts. Even though the work presented here contradicts the past research on the biological functions of iridoplasts, it doesn't necessarily exclude either the hypothesis of structural colouration-induced visual cues or light absorption enhancement. Despite the absence of significant amounts of blue light in the light conditions at which iridoplasts reflect these wavelengths (i.e. under the forest canopy), there might still be enough to create a distinctive colour for certain animals. In spite of a previous study investigating the PAR under the forest canopy [29], it might not be representative of the PAR under the natural habitat of *Begonias* and other photosynthetic photonic-containing plant species. Even under high light, the green structural colour of iridoplasts and bizonoplast might play a role similar to green iridoplasts, which are typically disregarded from the discussion because they are assumed to have a different biological function. Moreover, we

USC UNIVERSIDADE DE SANTIAGO DE COMPOSTELA

show only that absorption enhancement is not occurring in leaves by the 1D processes that have so far been the focus of research, particularly slow light. Therefore, we suggest here that future research should instead focus on a 3D approach to this problem, despite the non-conclusive preliminary results shown here. Indeed, Capretti et al. [6] demonstrated that the lateral morphology of chloroplasts is key to absorption. One could also speculate that iridoplasts have different functions from non-structured chloroplasts and that the extra light absorbed by the isolated system is needed.

To continue the investigation of photonic photosynthetic systems, we produced biomimetic structures. We showed that the strength of the photonic properties of organic multilayered structures can be enhanced by doping parts of the structure with a J-aggregate molecular dye. For example, we showed that doping a system, without changing the structure, could double the absolute reflectance from 40% to 80% and originate multi-photonic band gaps. This is a consequence of the higher refractive index contrast induced by the strong resonance of the J-aggregate dye. In addition, by controlling the photonic environment, we showed tunable light absorption enhancement.

Using the techniques developed and explained in this work, we created more all-organic photonic systems. All-organic Tamm states structures were demonstrated to be theoretically and experimentally possible. The narrow high reflectivity bands of the organic materials used provide a mode highly localised in momenta, allowing for tunability in the system. In addition, we demonstrated that photobleaching can be used to define the lateral dimensions of the organic multilayers by changing the refractive index of the surrounding environment instead of removing material. Finally, we created processable systems for surface polariton coupling. These systems consist of wrinkled polymer substrates, creating a grating structure, with the excitonic dye on top. The fabrication method requires improvement.

The development of organic photonic structures presents important advances toward large area, low financial cost, low environmental impact systems [237, 363–365] and the development of, for example, efficient coloured solar cells [366]. In this work, we have provided evidence that fully-organic systems can provide similar properties compared to their inorganic counterparts, despite the lower structural uniformity of the structure. Higher control over the morphology of the structures, including specific thicknesses and disorder, can be achieved with further development of fabrication techniques by, for example, automating the multilayer fabrication process [227, 367]. Additionally, the J-aggregate dye used in this work could be used to develop artificial photosynthetic devices with efficient energy transport based on the prolonged lifetime of excitons [301, 368–371].

USC UNIVERSIDADE DE SANTIAGO DE COMPOSTELA

Bibliography

[1] M. Jacobs, M. Lopez-Garcia, O. Phrathep, T. Lawson, R. Oulton, H. M. Whitney, *et al.*, "Photonic multilayer structure of begonia chloroplasts enhances photosynthetic efficiency," *Nature plants*, vol. 2, no. 11, pp. 1–6, 2016.

[2] R. E. Blankenship, *Molecular mechanisms of photosynthesis*. John Wiley & Sons, 2021.

[3] R. Croce, R. Van Grondelle, H. Van Amerongen, and I. Van Stokkum, *Light harvesting in photosynthesis*. CRC press, 2018.

[4] H. Van Amerongen, R. Van Grondelle, *et al.*, *Photosynthetic excitons*. World Scientific, 2000.

[5] R. E. Blankenship, "Early evolution of photosynthesis," *Plant physiology*, vol. 154, no. 2, pp. 434–438, 2010.

[6] A. Capretti, A. Ringsmuth, J. Van Velzen, A. Rosnik, R. Croce, and T. Gregorkiewicz, "Nanophotonics of higher-plant photosynthetic membranes," *Light: Science & Applications*, vol. 8, no. 1, pp. 1–13, 2019.

[7] S. Järvi, P. J. Gollan, and E.-M. Aro, "Understanding the roles of the thylakoid lumen in photosynthesis regulation," *Frontiers in plant science*, vol. 4, p. 434, 2013.

[8] D. J. Nield, "Schematic model of the major protein complexes involved in photosynthesis." http://jonnield.com/en/psIIimages/oxygenicphotosynthmodel.html. Accessed on 2022-06-08.

[9] R. Croce and H. van Amerongen, "Light harvesting in oxygenic photosynthesis: Structural biology meets spectroscopy," *Science*, vol. 369, no. 6506, p. eaay2058, 2020.

[10] A. Pandit and R. Frese, "Artificial leaves: towards bio-inspired solar energy converters," in *Comprehensive Renewable Energy*, Elsevier, 2012.

[11] J. A. Bassham and M. Calvin, "The path of carbon in photosynthesis," in *Die CO2-Assimilation/The Assimilation of Carbon Dioxide*, pp. 884–922, Springer, 1960.

[12] T. Förster, "Zwischenmolekulare energiewanderung und fluoreszenz," *Annalen der physik*, vol. 437, no. 1-2, pp. 55–75, 1948.

[13] M. Şener, J. Strümpfer, J. Hsin, D. Chandler, S. Scheuring, C. N. Hunter, and K. Schulten, "Förster energy transfer theory as reflected in the structures of photosynthetic light-harvesting systems," *ChemPhysChem*, vol. 12, no. 3, pp. 518–531, 2011.

USC

[14] T. Mirkovic, E. E. Ostroumov, J. M. Anna, R. Van Grondelle, and G. D. Scholes, "Light absorption and energy transfer in the antenna complexes of photosynthetic organisms," *Chemical reviews*, vol. 117, no. 2, pp. 249–293, 2017.

[15] G. D. Scholes, "Quantum-coherent electronic energy transfer: Did nature think of it first?," *The Journal of Physical Chemistry Letters*, vol. 1, no. 1, pp. 2–8, 2010.

[16] G. S. Engel, T. R. Calhoun, E. L. Read, T.-K. Ahn, T. Mančal, Y.-C. Cheng, R. E. Blankenship, and G. R. Fleming, "Evidence for wavelike energy transfer through quantum coherence in photosynthetic systems," *Nature*, vol. 446, no. 7137, pp. 782–786, 2007.

[17] G. Panitchayangkoon, D. Hayes, K. A. Fransted, J. R. Caram, E. Harel, J. Wen, R. E. Blankenship, and G. S. Engel, "Long-lived quantum coherence in photosynthetic complexes at physiological temperature," *Proceedings of the National Academy of Sciences*, vol. 107, no. 29, pp. 12766–12770, 2010.

[18] E. Collini, C. Y. Wong, K. E. Wilk, P. M. Curmi, P. Brumer, and G. D. Scholes, "Coherently wired light-harvesting in photosynthetic marine algae at ambient temperature," *Nature*, vol. 463, no. 7281, pp. 644–647, 2010.

[19] A. Ishizaki and G. R. Fleming, "Quantum superpositions in photosynthetic light harvesting: delocalization and entanglement," *New Journal of Physics*, vol. 12, no. 5, p. 055004, 2010.

[20] D. Coles, L. C. Flatten, T. Sydney, E. Hounslow, S. K. Saikin, A. Aspuru-Guzik, V. Vedral, J. K.-H. Tang, R. A. Taylor, J. M. Smith, *et al.*, "A nanophotonic structure containing living photosynthetic bacteria," *Small*, vol. 13, no. 38, p. 1701777, 2017.

[21] R. Hildner, D. Brinks, J. B. Nieder, R. J. Cogdell, and N. F. van Hulst, "Quantum coherent energy transfer over varying pathways in single light-harvesting complexes," *Science*, vol. 340, no. 6139, pp. 1448–1451, 2013.

[22] F.-F. Kong, X.-J. Tian, Y. Zhang, Y. Zhang, G. Chen, Y.-J. Yu, S.-H. Jing, H.-Y. Gao, Y. Luo, J.-L. Yang, *et al.*, "Wavelike electronic energy transfer in donor–acceptor molecular systems through quantum coherence," *Nature Nanotechnology*, pp. 1–8, 2022.

[23] H.-G. Duan, V. I. Prokhorenko, R. J. Cogdell, K. Ashraf, A. L. Stevens, M. Thorwart, and R. D. Miller, "Nature does not rely on long-lived electronic quantum coherence for photosynthetic energy transfer," *Proceedings of the National Academy of Sciences*, vol. 114, no. 32, pp. 8493–8498, 2017.

[24] C. L. Cortes, W. Sun, and Z. Jacob, "Fundamental efficiency bound for quantum coherent energy transfer in nanophotonics," *Optics Express*, vol. 30, no. 19, pp. 34725–34739, 2022.

[25] G. D. Scholes, G. R. Fleming, A. Olaya-Castro, and R. Van Grondelle, "Lessons from nature about solar light harvesting," *Nature chemistry*, vol. 3, no. 10, pp. 763–774, 2011.

[26] M. F. Hohmann-Marriott, R. E. Blankenship, *et al.*, "Evolution of photosynthesis," *Annual review of plant biology*, vol. 62, no. 1, pp. 515–548, 2011.

USC UNIVERSIDADE DE SANTIAGO DE COMPOSTELA

[27] G. A. Armstrong and J. E. Hearst, "Genetics and molecular biology of carotenoid pigment biosynthesis," *The FASEB journal*, vol. 10, no. 2, pp. 228–237, 1996.

[28] S. Zhen and B. Bugbee, "Far-red photons have equivalent efficiency to traditional photosynthetic photons: Implications for redefining photosynthetically active radiation," *Plant, cell & environment*, vol. 43, no. 5, pp. 1259–1272, 2020.

[29] J. A. Endler, "The color of light in forests and its implications," *Ecological monographs*, vol. 63, no. 1, pp. 1–27, 1993.

[30] J. M. Anderson, W. Chow, and D. Goodchild, "Thylakoid membrane organisation in sun/shade acclimation," *Functional Plant Biology*, vol. 15, no. 2, pp. 11–26, 1988.

[31] J.-D. Rochaix *et al.*, "Regulation and dynamics of the light-harvesting system," *Annu Rev Plant Biol*, vol. 65, no. 1, pp. 287–309, 2014.

[32] R. Croce and H. Van Amerongen, "Natural strategies for photosynthetic light harvesting," *Nature chemical biology*, vol. 10, no. 7, pp. 492–501, 2014.

[33] X. Meng, L. Liu, and X. Chen, "Bacterial photosynthesis: state-of-the-art in light-driven carbon fixation in engineered bacteria," *Current Opinion in Microbiology*, vol. 69, p. 102174, 2022.

[34] E. Yablonovitch, "Inhibited spontaneous emission in solid-state physics and electronics," *Physical review letters*, vol. 58, no. 20, p. 2059, 1987.

[35] S. John, "Strong localization of photons in certain disordered dielectric superlattices," *Physical review letters*, vol. 58, no. 23, p. 2486, 1987.

[36] J. D. Joannopoulos, P. R. Villeneuve, and S. Fan, "Photonic crystals: putting a new twist on light," *Nature*, vol. 386, no. 6621, pp. 143–149, 1997.

[37] J. D. Joannopoulos, S. G. Johnson, J. N. Winn, and R. D. Meade, "Molding the flow of light," *Princeton Univ. Press, Princeton, NJ [ua]*, 2008.

[38] C. M. Soukoulis, *Photonic crystals and light localization in the 21st century*, vol. 563. Springer Science & Business Media, 2012.

[39] S. Noda and T. Baba, *Roadmap on photonic crystals*, vol. 1. Springer Science & Business Media, 2003.

[40] W. H. Bragg and W. L. Bragg, "The reflection of x-rays by crystals," *Proceedings of the Royal Society of London. Series A, Containing Papers of a Mathematical and Physical Character*, vol. 88, no. 605, pp. 428–438, 1913.

[41] P. Yeh, *Optical Waves in Layered Media*. John Wiley and Sons, 1988.

[42] R. W. Boyd, D. J. Gauthier, and A. L. Gaeta, "Applications of slow light in telecommunications," *Optics and Photonics News*, vol. 17, no. 4, pp. 18–23, 2006.

USC UNIVERSIDADE DE SANTIAGO DE COMPOSTELA

[43] Y. Okawachi, M. S. Bigelow, J. E. Sharping, Z. Zhu, A. Schweinsberg, D. J. Gauthier, R. W. Boyd, and A. L. Gaeta, "Tunable all-optical delays via brillouin slow light in an optical fiber," *Physical review letters*, vol. 94, no. 15, p. 153902, 2005.

[44] Z. Shi, R. W. Boyd, R. M. Camacho, P. K. Vudyasetu, and J. C. Howell, "Slow-light fourier transform interferometer," *Physical Review Letters*, vol. 99, no. 24, p. 240801, 2007.

[45] M. Shahriar, G. Pati, R. Tripathi, V. Gopal, M. Messall, and K. Salit, "Ultrahigh enhancement in absolute and relative rotation sensing using fast and slow light," *Physical review A*, vol. 75, no. 5, p. 053807, 2007.

[46] R. W. Boyd, "Slow and fast light: fundamentals and applications," *Journal of Modern Optics*, vol. 56, no. 18-19, pp. 1908–1915, 2009.

[47] R. W. Boyd and P. Narum, "Slow-and fast-light: fundamental limitations," *Journal of Modern Optics*, vol. 54, no. 16-17, pp. 2403–2411, 2007.

[48] L. V. Hau, S. E. Harris, Z. Dutton, and C. H. Behroozi, "Light speed reduction to 17 metres per second in an ultracold atomic gas," *Nature*, vol. 397, no. 6720, pp. 594–598, 1999.

[49] M. S. Bigelow, N. N. Lepeshkin, and R. W. Boyd, "Observation of ultraslow light propagation in a ruby crystal at room temperature," *Physical review letters*, vol. 90, no. 11, p. 113903, 2003.

[50] T. Baba, "Slow light in photonic crystals," *Nature photonics*, vol. 2, no. 8, pp. 465–473, 2008.

[51] B. Qiu, Y. Lin, E. S. Arinze, A. Chiu, L. Li, and S. M. Thon, "Photonic band engineering in absorbing media for spectrally selective optoelectronic films," *Optics Express*, vol. 26, no. 21, pp. 26933–26945, 2018.

[52] N. A. Mortensen and S. Xiao, "Slow-light enhancement of beer-lambert-bouguer absorption," *Applied Physics Letters*, vol. 90, no. 14, p. 141108, 2007.

[53] J. Pedersen, S. Xiao, and N. A. Mortensen, "Slow-light enhanced absorption for biochemical sensing applications: potential of low-contrast lossy materials," *arXiv preprint arXiv:0802.0558*, 2008.

[54] J. Liu, H. Zhao, M. Wu, B. Van der Schueren, Y. Li, O. Deparis, J. Ye, G. A. Ozin, T. Hasan, and B.-L. Su, "Slow photons for photocatalysis and photovoltaics," *Advanced Materials*, vol. 29, no. 17, p. 1605349, 2017.

[55] S. Nishimura, N. Abrams, B. A. Lewis, L. I. Halaoui, T. E. Mallouk, K. D. Benkstein, J. Van de Lagemaat, and A. J. Frank, "Standing wave enhancement of red absorbance and photocurrent in dye-sensitized titanium dioxide photoelectrodes coupled to photonic crystals," *Journal of the American Chemical Society*, vol. 125, no. 20, pp. 6306–6310, 2003.

[56] G. D. Scholes and G. Rumbles, "Excitons in nanoscale systems," *Materials For Sustainable Energy: A Collection of Peer-Reviewed Research and Review Articles from Nature Publishing Group*, pp. 12–25, 2011.

USC

[57] S. K. Rajendran, M. Wei, H. Ohadi, A. Ruseckas, G. A. Turnbull, and I. D. Samuel, "Low threshold polariton lasing from a solution-processed organic semiconductor in a planar microcavity," *Advanced Optical Materials*, vol. 7, no. 12, p. 1801791, 2019.

[58] A. Tarraf, J. Daleiden, S. Irmer, D. Prasai, and H. Hillmer, "Stress investigation of pecvd dielectric layers for advanced optical mems," *Journal of Micromechanics and Microengineering*, vol. 14, no. 3, p. 317, 2003.

[59] M. Horák, K. Bukvišová, V. Švarc, J. Jaskowiec, V. Křápek, and T. Šikola, "Comparative study of plasmonic antennas fabricated by electron beam and focused ion beam lithography," *Scientific Reports*, vol. 8, no. 1, pp. 1–8, 2018.

[60] S. F. Liew and H. Cao, "Optical properties of 1d photonic crystals with correlated and uncorrelated disorder," *Journal of Optics*, vol. 12, no. 2, p. 024011, 2010.

[61] S. Hughes, L. Ramunno, J. F. Young, and J. Sipe, "Extrinsic optical scattering loss in photonic crystal waveguides: role of fabrication disorder and photon group velocity," *Physical review letters*, vol. 94, no. 3, p. 033903, 2005.

[62] K. Szendrei, P. Ganter, O. Sànchez-Sobrado, R. Eger, A. Kuhn, and B. V. Lotsch, "Touchless optical finger motion tracking based on 2d nanosheets with giant moisture responsiveness," *Advanced Materials*, vol. 27, no. 41, pp. 6341–6348, 2015.

[63] W. L. Barnes, A. Dereux, and T. W. Ebbesen, "Surface plasmon subwavelength optics," *nature*, vol. 424, no. 6950, pp. 824–830, 2003.

[64] G. M. Paterno, L. Moscardi, S. Donini, D. Ariodanti, I. Kriegel, M. Zani, E. Parisini, F. Scotognella, and G. Lanzani, "Hybrid one-dimensional plasmonic–photonic crystals for optical detection of bacterial contaminants," *The Journal of Physical Chemistry Letters*, vol. 10, no. 17, pp. 4980–4986, 2019.

[65] C. Santori, D. Fattal, J. Vučković, G. S. Solomon, and Y. Yamamoto, "Indistinguishable photons from a single-photon device," *nature*, vol. 419, no. 6907, pp. 594–597, 2002.

[66] F. Michelotti, B. Sciacca, L. Dominici, M. Quaglio, E. Descrovi, F. Giorgis, and F. Geobaldo, "Fast optical vapour sensing by bloch surface waves on porous silicon membranes," *Physical Chemistry Chemical Physics*, vol. 12, no. 2, pp. 502–506, 2010.

[67] M.-I. Georgaki, A. Botsialas, P. Argitis, N. Papanikolaou, P. Oikonomou, I. Raptis, J. Rysz, A. Budkowski, and M. Chatzichristidi, "1-d polymeric photonic crystals as spectroscopic zero-power humidity sensors," *Microelectronic engineering*, vol. 115, pp. 55–60, 2014.

[68] S. M. Melle, A. T. Alavie, S. Karr, T. Coroy, K. Liu, and R. M. Measures, "A bragg grating-tuned fiber laser strain sensor system," *IEEE Photonics Technology Letters*, vol. 5, no. 2, pp. 263–266, 1993.

[69] Y. Fang and M. Sun, "Nanoplasmonic waveguides: towards applications in integrated nanophotonic circuits," *Light: Science & Applications*, vol. 4, no. 6, pp. e294–e294, 2015.

USC UNIVERSIDADE DE SANTIAGO DE

[70] P. Yeh, A. Yariv, and A. Y. Cho, "Optical surface waves in periodic layered media," *Applied Physics Letters*, vol. 32, no. 2, pp. 104–105, 1978.

[71] P. Yeh, A. Yariv, and C.-S. Hong, "Electromagnetic propagation in periodic stratified media. i. general theory," *JOSA*, vol. 67, no. 4, pp. 423–438, 1977.

[72] J. Chen, J. Shi, D. Decanini, E. Cambril, Y. Chen, and A.-M. Haghiri-Gosnet, "Gold nanohole arrays for biochemical sensing fabricated by soft uv nanoimprint lithography," *Microelectronic Engineering*, vol. 86, no. 4-6, pp. 632–635, 2009.

[73] K. Nishiguchi, K. Sueyoshi, H. Hisamoto, and T. Endo, "Fabrication of gold-deposited plasmonic crystal based on nanoimprint lithography for label-free biosensing application," *Japanese Journal of Applied Physics*, vol. 55, no. 8S3, p. 08RE02, 2016.

[74] A. Klinkova, R. M. Choueiri, and E. Kumacheva, "Self-assembled plasmonic nanostructures," *Chemical Society Reviews*, vol. 43, no. 11, pp. 3976–3991, 2014.

[75] A. Yadav, N. Yadav, V. Agrawal, S. P. Polyutov, A. S. Tsipotan, S. V. Karpov, V. V. Slabko, V. S. Yadav, Y. Wu, H. Zheng, *et al.*, "State-of-art plasmonic photonic crystals based on self-assembled nanostructures," *Journal of Materials Chemistry C*, vol. 9, no. 10, pp. 3368–3383, 2021.

[76] K. Thorkelsson, P. Bai, and T. Xu, "Self-assembly and applications of anisotropic nanomaterials: A review," *Nano Today*, vol. 10, no. 1, pp. 48–66, 2015.

[77] E. S. Goerlitzer, R. N. Klupp Taylor, and N. Vogel, "Bioinspired photonic pigments from colloidal self-assembly," *Advanced Materials*, vol. 30, no. 28, p. 1706654, 2018.

[78] H. Zhou, J. Xu, X. Liu, H. Zhang, D. Wang, Z. Chen, D. Zhang, and T. Fan, "Bioinspired photonic materials: Prototypes and structural effect designs for applications in solar energy manipulation," *Advanced Functional Materials*, vol. 28, no. 24, p. 1705309, 2018.

[79] L. P. Biro and J.-P. Vigneron, "Photonic nanoarchitectures in butterflies and beetles: valuable sources for bioinspiration," *Laser & Photonics Reviews*, vol. 5, no. 1, pp. 27–51, 2011.

[80] J. Ge and Y. Yin, "Responsive photonic crystals," *Angewandte Chemie International Edition*, vol. 50, no. 7, pp. 1492–1522, 2011.

[81] P. Wu, J. Wang, and L. Jiang, "Bio-inspired photonic crystal patterns," *Materials Horizons*, vol. 7, no. 2, pp. 338–365, 2020.

[82] G. Kamita, B. Frka-Petesic, A. Allard, M. Dargaud, K. King, A. G. Dumanli, and S. Vignolini, "Biocompatible and sustainable optical strain sensors for large-area applications," *Advanced Optical Materials*, vol. 4, no. 12, pp. 1950–1954, 2016.

[83] L. Shang, W. Zhang, K. Xu, and Y. Zhao, "Bio-inspired intelligent structural color materials," *Materials Horizons*, vol. 6, no. 5, pp. 945–958, 2019.

USC UNIVERSIDADE DE SANTIAGO

[84] W. P. Wardley, J. W. Goessling, and M. Lopez-Garcia, "Plasmonic crystals with highly ordered lattice geometries using continuous metal films on diatom bio-silica as both scaffolds and sources of tuneability," *arXiv preprint arXiv:2108.01602*, 2021.

[85] R. Hooke, *Micrographia: or some physiological descriptions of minute bodies made by magnifying glasses, with observations and inquiries thereupon.* Courier Corporation, 2003.

[86] I. Newton, *Opticks, or, a treatise of the reflections, refractions, inflections & colours of light.* Courier Corporation, 1979.

[87] T. Young, "Experimental demonstration of the general law of the interference of light," *Philosophical Transactions of the Royal society of London*, vol. 94, no. 1804, p. 1, 1804.

[88] F. E. Beddard, *Animal coloration: an account of the principal facts and theories relating to the colours and markings of animals.* London, S. Sonnenschein & Company, 1892.

[89] T. F. Anderson and A. G. Richards Jr, "An electron microscope study of some structural colors of insects," *Journal of applied Physics*, vol. 13, no. 12, pp. 748–758, 1942.

[90] P. Vukusic and J. R. Sambles, "Photonic structures in biology," *Nature*, vol. 424, no. 6950, pp. 852–855, 2003.

[91] A. R. Parker and N. Martini, "Structural colour in animals—simple to complex optics," *Optics & Laser Technology*, vol. 38, no. 4-6, pp. 315–322, 2006.

[92] A. Loyau, D. Gomez, B. Moureau, M. Théry, N. S. Hart, M. S. Jalme, A. T. Bennett, and G. Sorci, "Iridescent structurally based coloration of eyespots correlates with mating success in the peacock," *Behavioral Ecology*, vol. 18, no. 6, pp. 1123–1131, 2007.

[93] S. Niu, B. Li, Z. Mu, M. Yang, J. Zhang, Z. Han, and L. Ren, "Excellent structure-based multifunction of morpho butterfly wings: A review," *Journal of Bionic Engineering*, vol. 12, no. 2, pp. 170–189, 2015.

[94] C. J. Chandler, B. D. Wilts, S. Vignolini, J. Brodie, U. Steiner, P. J. Rudall, B. J. Glover, T. Gregory, and R. H. Walker, "Structural colour in chondrus crispus," *Scientific reports*, vol. 5, no. 1, pp. 1–10, 2015.

[95] S. Vignolini, P. J. Rudall, A. V. Rowland, A. Reed, E. Moyroud, R. B. Faden, J. J. Baumberg, B. J. Glover, and U. Steiner, "Pointillist structural color in pollia fruit," *Proceedings of the National Academy of Sciences*, vol. 109, no. 39, pp. 15712–15715, 2012.

[96] A. L. Holt, S. Vahidinia, Y. L. Gagnon, D. E. Morse, and A. M. Sweeney, "Photosymbiotic giant clams are transformers of solar flux," *Journal of the Royal Society Interface*, vol. 11, no. 101, p. 20140678, 2014.

[97] M. Lopez-Garcia, N. Masters, H. E. O'Brien, J. Lennon, G. Atkinson, M. J. Cryan, R. Oulton, and H. M. Whitney, "Light-induced dynamic structural color by intracellular 3d photonic crystals in brown algae," *Science advances*, vol. 4, no. 4, p. eaan8917, 2018.

[98] B. Pettifor, L. M. Rasmusson, and J. M. Hall-Spencer, "Dynamic structural colour increases photosynthetic performance in the alga ericaria selaginoides," *Applied Phycology*, vol. 2, no. 1, pp. 31–40, 2021.

USC UNIVERSIDADE DE SANTIAGO DE COMPOSTELA

[99] J. W. Goessling, W. P. Wardley, and M. Lopez-Garcia, "Highly reproducible, bio-based slab photonic crystals grown by diatoms," *Advanced Science*, vol. 7, no. 10, p. 1903726, 2020.

[100] J. W. Goessling, A. A. S. González, V. S. P. Raj, M. P. Ashworth, S. R. Manning, and M. Lopez-Garcia, "Biosilica slab photonic crystals as an alternative to cleanroom nanofabrication?," *Faraday Discussions*, vol. 223, pp. 261–277, 2020.

[101] J. M. Medina, J. A. Díaz, and P. Vukusic, "Classification of peacock feather reflectance using principal component analysis similarity factors from multispectral imaging data," *Optics express*, vol. 23, no. 8, pp. 10198–10212, 2015.

[102] R. A. Potyrailo, R. K. Bonam, J. G. Hartley, T. A. Starkey, P. Vukusic, M. Vasudev, T. Bunning, R. R. Naik, Z. Tang, M. A. Palacios, *et al.*, "Towards outperforming conventional sensor arrays with fabricated individual photonic vapour sensors inspired by morpho butterflies," *Nature communications*, vol. 6, no. 1, pp. 1–12, 2015.

[103] D. W. Lee and J. B. Lowry, "Physical basis and ecological significance of iridescence in blue plants," *Nature*, vol. 254, no. 5495, pp. 50–51, 1975.

[104] C. Hébant and D. W. Lee, "Ultrastructural basis and developmental control of blue iridescence in selaginella leaves," *American Journal of Botany*, vol. 71, no. 2, pp. 216–219, 1984.

[105] K. R. Thomas, M. Kolle, H. M. Whitney, B. J. Glover, and U. Steiner, "Function of blue iridescence in tropical understorey plants," *Journal of the Royal Society Interface*, vol. 7, no. 53, pp. 1699–1707, 2010.

[106] A. Nasrulhaq-Boyce and J. Duckett, "Dimorphic epidermal cell chloroplasts in the mesophyll-less leaves of an extreme–shade tropical fern, teratophyllum rotundifoliatum (r. bonap.) holtt.: a light and electron microscope study," *New Phytologist*, vol. 119, no. 3, pp. 433–444, 1991.

[107] R. M. Graham, D. W. Lee, and K. Norstog, "Physical and ultrastructural basis of blue leaf iridescence in two neotropical ferns," *American Journal of Botany*, vol. 80, no. 2, pp. 198–203, 1993.

[108] K. S. Gould and D. W. Lee, "Physical and ultrastructural basis of blue leaf iridescence in four malaysian understory plants," *American Journal of Botany*, vol. 83, no. 1, pp. 45–50, 1996.

[109] G. Paillotin, W. Leibl, J. Gapiński, J. Breton, and A. Dobek, "Light gradients in spherical photosynthetic vesicles," *Biophysical journal*, vol. 75, no. 1, pp. 124–133, 1998.

[110] P. S. Pankin, A. V. Shabanov, D. N. Maksimov, S. V. Nabol, D. S. Buzin, A. I. Krasnov, G. A. Romanenko, V. S. Sutormin, V. A. Gunyakov, F. V. Zelenov, *et al.*, "Asymmetric resonant light absorption in a chloroplast microstructure," *JOSA B*, vol. 40, no. 1, pp. 87–93, 2023.

USC UNIVERSIDADE DE SANTIAGO DE COMPOSTELA

[111] N. J. Masters, M. Lopez-Garcia, R. Oulton, and H. M. Whitney, "Characterization of chloroplast iridescence in selaginella erythropus," *Journal of the Royal Society Interface*, vol. 15, no. 148, p. 20180559, 2018.

[112] C.-R. Sheue, V. Sarafis, R. Kiew, H.-Y. Liu, A. Salino, L.-L. Kuo-Huang, Y.-P. Yang, C.-C. Tsai, C.-H. Lin, J. W. Yong, *et al.*, "Bizonoplast, a unique chloroplast in the epidermal cells of microphylls in the shade plant selaginella erythropus (selaginellaceae)," *American Journal of Botany*, vol. 94, no. 12, pp. 1922–1929, 2007.

[113] C.-R. Sheue, J.-W. Liu, J.-F. Ho, A.-W. Yao, Y.-H. Wu, S. Das, C.-C. Tsai, H.-A. Chu, M. S. Ku, and P. Chesson, "A variation on chloroplast development: the bizonoplast and photosynthetic efficiency in the deep-shade plant selaginella erythropus," *American journal of botany*, vol. 102, no. 4, pp. 500–511, 2015.

[114] R. Ghaffar, M. Weidinger, B. Mähnert, M. Schagerl, and I. Lichtscheidl, "Adaptive responses of mature giant chloroplasts in the deep-shade lycopod selaginella erythropus to prolonged light and dark periods," *Plant, Cell & Environment*, vol. 41, no. 8, pp. 1791–1805, 2018.

[115] O.-P. Phrathep *et al.*, *Biodiversity and physiology of Begonia iridoplasts.* PhD thesis, University of Bristol, 2020.

[116] S.-H. Pao, P.-Y. Tsai, C.-I. Peng, P.-J. Chen, C.-C. Tsai, E.-C. Yang, M.-C. Shih, J. Chen, J.-Y. Yang, P. Chesson, *et al.*, "Lamelloplasts and minichloroplasts in begoniaceae: iridescence and photosynthetic functioning," *Journal of plant research*, vol. 131, no. 4, pp. 655–670, 2018.

[117] H. Perryman, *Iridoplasts as a photonic structure.* PhD thesis, University of Bristol, 2022.

[118] H. M. Whitney, M. Kolle, P. Andrew, L. Chittka, U. Steiner, and B. J. Glover, "Floral iridescence, produced by diffractive optics, acts as a cue for animal pollinators," *Science*, vol. 323, no. 5910, pp. 130–133, 2009.

[119] D. Clarke, H. Whitney, G. Sutton, and D. Robert, "Detection and learning of floral electric fields by bumblebees," *Science*, vol. 340, no. 6128, pp. 66–69, 2013.

[120] D. A. Lawson, H. M. Whitney, and S. A. Rands, "Colour as a backup for scent in the presence of olfactory noise: testing the efficacy backup hypothesis using bumblebees (bombus terrestris)," *Royal Society Open Science*, vol. 4, no. 11, p. 170996, 2017.

[121] B. J. Glover and H. M. Whitney, "Structural colour and iridescence in plants: the poorly studied relations of pigment colour," *Annals of botany*, vol. 105, no. 4, pp. 505–511, 2010.

[122] A. V. Shabanov, M. A. Korshunov, and E. R. Bukhanov, "Features of the amplification of the electromagnetic field and the density of states of photonic crystal structures in plants," *Computer Optics*, vol. 43, no. 2, pp. 231–237, 2019.

[123] X. Zhou, Y. Zhang, H. Ding, J. Liao, Q. Li, and Z. Gu, "Begonia-inspired slow photon effect of a photonic crystal for augmenting algae photosynthesis," *ACS Nano*, 2022.

USC UNIVERSIDADE DE SANTIAGO DE COMPOSTELA

[124] V. U. Chukhutsina, A. R. Holzwarth, and R. Croce, "Time-resolved fluorescence measurements on leaves: principles and recent developments," *Photosynthesis Research*, vol. 140, no. 3, pp. 355–369, 2019.

[125] E. H. Murchie and T. Lawson, "Chlorophyll fluorescence analysis: a guide to good practice and understanding some new applications," *Journal of experimental botany*, vol. 64, no. 13, pp. 3983–3998, 2013.

[126] H. Kirchhoff, C. Hall, M. Wood, M. Herbstová, O. Tsabari, R. Nevo, D. Charuvi, E. Shimoni, and Z. Reich, "Dynamic control of protein diffusion within the granal thylakoid lumen," *Proceedings of the National Academy of Sciences*, vol. 108, no. 50, pp. 20248–20253, 2011.

[127] W. H. Wood, C. MacGregor-Chatwin, S. F. Barnett, G. E. Mayneord, X. Huang, J. K. Hobbs, C. N. Hunter, and M. P. Johnson, "Dynamic thylakoid stacking regulates the balance between linear and cyclic photosynthetic electron transfer," *Nature plants*, vol. 4, no. 2, pp. 116–127, 2018.

[128] C. Ünlü, B. Drop, R. Croce, and H. van Amerongen, "State transitions in chlamydomonas reinhardtii strongly modulate the functional size of photosystem ii but not of photosystem i," *Proceedings of the National Academy of Sciences*, vol. 111, no. 9, pp. 3460–3465, 2014.

[129] V. U. Chukhutsina, C. Büchel, and H. Van Amerongen, "Disentangling two non-photochemical quenching processes in cyclotella meneghiniana by spectrally-resolved picosecond fluorescence at 77 k," *Biochimica et Biophysica Acta (BBA)-Bioenergetics*, vol. 1837, no. 6, pp. 899–907, 2014.

[130] E. E. Jelley, "Spectral absorption and fluorescence of dyes in the molecular state," *Nature*, vol. 138, no. 3502, pp. 1009–1010, 1936.

[131] G. Scheibe, "Über die veränderlichkeit der absorptionsspektren in lösungen und die nebenvalenzen als ihre ursache," *Angewandte Chemie*, vol. 50, no. 11, pp. 212–219, 1937.

[132] U. Rösch, S. Yao, R. Wortmann, and F. Würthner, "Fluorescent h-aggregates of merocyanine dyes," *Angewandte Chemie*, vol. 118, no. 42, pp. 7184–7188, 2006.

[133] J. L. Bricks, Y. L. Slominskii, I. D. Panas, and A. P. Demchenko, "Fluorescent j-aggregates of cyanine dyes: basic research and applications review," *Methods and applications in fluorescence*, vol. 6, no. 1, p. 012001, 2017.

[134] S. Kirstein and S. Daehne, "J-aggregates of amphiphilic cyanine dyes: Self-organization of artificial light harvesting complexes," *International Journal of Photoenergy*, vol. 2006, 2006.

[135] F. Würthner, T. E. Kaiser, and C. R. Saha-Möller, "J-aggregates: from serendipitous discovery to supramolecular engineering of functional dye materials," *Angewandte Chemie International Edition*, vol. 50, no. 15, pp. 3376–3410, 2011.

USC UNIVERSIDADE DE SANTIAGO DE COMPOSTELA

[136] T. Miyatake and H. Tamiaki, "Self-aggregates of natural chlorophylls and their synthetic analogues in aqueous media for making light-harvesting systems," *Coordination Chemistry Reviews*, vol. 254, no. 21-22, pp. 2593–2602, 2010.

[137] S. Sengupta and F. Wurthner, "Chlorophyll j-aggregates: From bioinspired dye stacks to nanotubes, liquid crystals, and biosupramolecular electronics," *Accounts of chemical research*, vol. 46, no. 11, pp. 2498–2512, 2013.

[138] T. Brixner, R. Hildner, J. Köhler, C. Lambert, and F. Würthner, "Exciton transport in molecular aggregates–from natural antennas to synthetic chromophore systems," *Advanced Energy Materials*, vol. 7, no. 16, p. 1700236, 2017.

[139] S. K. Saikin, A. Eisfeld, S. Valleau, and A. Aspuru-Guzik, "Photonics meets excitonics: natural and artificial molecular aggregates," *Nanophotonics*, vol. 2, no. 1, pp. 21–38, 2013.

[140] H. Kano and T. Kobayashi, "Time-resolved fluorescence and absorption spectroscopies of porphyrin j-aggregates," *The Journal of chemical physics*, vol. 116, no. 1, pp. 184–195, 2002.

[141] T. E. Kaiser, H. Wang, V. Stepanenko, and F. Würthner, "Supramolecular construction of fluorescent j-aggregates based on hydrogen-bonded perylene dyes," *Angewandte Chemie*, vol. 119, no. 29, pp. 5637–5640, 2007.

[142] V. Huber, M. Katterle, M. Lysetska, and F. Würthner, "Reversible self-organization of semisynthetic zinc chlorins into well-defined rod antennae," *Angewandte Chemie International Edition*, vol. 44, no. 20, pp. 3147–3151, 2005.

[143] C. G. Williams, "Xxvi.—researches on chinoline and its homologues," *Earth and Environmental Science Transactions of the Royal Society of Edinburgh*, vol. 21, no. 3, pp. 377–401, 1857.

[144] K. Misawa, H. Ono, K. Minoshima, and T. Kobayashi, "New fabrication method for highly oriented j aggregates dispersed in polymer films," *Applied physics letters*, vol. 63, no. 5, pp. 577–579, 1993.

[145] S. T. Holder, C. Estévez-Varela, I. Pastoriza-Santos, M. Lopez-Garcia, R. Oulton, and S. Núñez-Sánchez, "Bio-inspired polymers with polaritonic properties from visible to infrared: a material playground to mimic purple bacteria light-harvesting resonators," *arXiv preprint arXiv:2210.02315*, 2022.

[146] P. V. Pisklova, I. Y. Ropakova, I. I. Bespalova, S. L. Yefimova, and A. V. Sorokin, "Interaction between molecular aggregates placed into thin layered films," *Molecular Crystals and Liquid Crystals*, pp. 1–12, 2022.

[147] J. Knoester, "Optical properties of molecular aggregates," in *Organic Nanostructures: Science and Applications*, pp. 149–186, IOS Press, 2002.

[148] M. J. Gentile, S. Núñez-Sánchez, and W. L. Barnes, "Optical field-enhancement and subwavelength field-confinement using excitonic nanostructures," *Nano Letters*, vol. 14, no. 5, pp. 2339–2344, 2014.

USC UNIVERSIDADE DE SANTIAGO DE COMPOSTELA

[149] S. Kundu and A. Patra, "Nanoscale strategies for light harvesting," *Chemical reviews*, vol. 117, no. 2, pp. 712–757, 2017.

[150] Q. Song, S. Goia, J. Yang, S. C. Hall, M. Staniforth, V. G. Stavros, and S. Perrier, "Efficient artificial light-harvesting system based on supramolecular peptide nanotubes in water," *Journal of the American Chemical Society*, vol. 143, no. 1, pp. 382–389, 2020.

[151] R. Ziessel and A. Harriman, "Artificial light-harvesting antennae: electronic energy transfer by way of molecular funnels," *Chemical Communications*, vol. 47, no. 2, pp. 611–631, 2011.

[152] C. V. Kumar and M. R. Duff Jr, "Dna-based supramolecular artificial light harvesting complexes," *Journal of the American Chemical Society*, vol. 131, no. 44, pp. 16024–16026, 2009.

[153] R. d. L. Kronig, "On the theory of dispersion of x-rays," *Josa*, vol. 12, no. 6, pp. 547–557, 1926.

[154] H. A. Kramers, "La diffusion de la lumiere par les atomes," in *Atti Cong. Intern. Fisica (Transactions of Volta Centenary Congress) Como*, vol. 2, pp. 545–557, 1927.

[155] B. G. Anex and W. T. Simpson, "Metallic reflection from molecular crystals," *Reviews of Modern Physics*, vol. 32, no. 2, p. 466, 1960.

[156] B. A. Gregg, "Excitonic solar cells," 2003.

[157] S. M. Menke and R. J. Holmes, "Exciton diffusion in organic photovoltaic cells," *Energy & Environmental Science*, vol. 7, no. 2, pp. 499–512, 2014.

[158] E. S. Kang, S. Kk, I. Jeon, J. Kim, S. Chen, K.-H. Kim, K.-H. Kim, H. S. Lee, F. Westerlund, and M. P. Jonsson, "Organic anisotropic excitonic optical nanoantennas," *Advanced Science*, p. 2201907, 2022.

[159] S. Nunez-Sanchez, M. Lopez-Garcia, M. M. Murshidy, A. G. Abdel-Hady, M. Serry, A. M. Adawi, J. G. Rarity, R. Oulton, and W. L. Barnes, "Excitonic optical tamm states: A step toward a full molecular–dielectric photonic integration," *ACS Photonics*, vol. 3, no. 5, pp. 743–748, 2016.

[160] M. Fox, "Optical properties of solids," 2002.

[161] D. K. Gramotnev and S. I. Bozhevolnyi, "Plasmonics beyond the diffraction limit," *Nature photonics*, vol. 4, no. 2, pp. 83–91, 2010.

[162] J. Homola, S. S. Yee, and G. Gauglitz, "Surface plasmon resonance sensors," *Sensors and actuators B: Chemical*, vol. 54, no. 1-2, pp. 3–15, 1999.

[163] H. Yu, Y. Peng, Y. Yang, and Z.-Y. Li, "Plasmon-enhanced light–matter interactions and applications," *npj Computational Materials*, vol. 5, no. 1, pp. 1–14, 2019.

[164] T. W. Ebbesen, C. Genet, and S. I. Bozhevolnyi, "Surface-plasmon circuitry," *Physics Today*, vol. 61, no. 5, p. 44, 2008.

USC UNIVERSIDADE DE SANTIAGO DE COMPOSTELA

[165] C. Haffner, W. Heni, Y. Fedoryshyn, J. Niegemann, A. Melikyan, D. L. Elder, B. Baeuerle, Y. Salamin, A. Josten, U. Koch, *et al.*, "All-plasmonic mach–zehnder modulator enabling optical high-speed communication at the microscale," *Nature Photonics*, vol. 9, no. 8, pp. 525–528, 2015.

[166] M. Ayata, Y. Fedoryshyn, W. Heni, B. Baeuerle, A. Josten, M. Zahner, U. Koch, Y. Salamin, C. Hoessbacher, C. Haffner, *et al.*, "High-speed plasmonic modulator in a single metal layer," *Science*, vol. 358, no. 6363, pp. 630–632, 2017.

[167] A. G. Curto, G. Volpe, T. H. Taminiau, M. P. Kreuzer, R. Quidant, and N. F. van Hulst, "Unidirectional emission of a quantum dot coupled to a nanoantenna," *Science*, vol. 329, no. 5994, pp. 930–933, 2010.

[168] P. Berini, "Surface plasmon photodetectors and their applications," *Laser & Photonics Reviews*, vol. 8, no. 2, pp. 197–220, 2014.

[169] J.-A. Huang, Y.-Q. Zhao, X.-J. Zhang, L.-F. He, T.-L. Wong, Y.-S. Chui, W.-J. Zhang, and S.-T. Lee, "Ordered ag/si nanowires array: wide-range surface-enhanced raman spectroscopy for reproducible biomolecule detection," *Nano letters*, vol. 13, no. 11, pp. 5039–5045, 2013.

[170] Y. He, S. Su, T. Xu, Y. Zhong, J. A. Zapien, J. Li, C. Fan, and S.-T. Lee, "Silicon nanowires-based highly-efficient sers-active platform for ultrasensitive dna detection," *Nano Today*, vol. 6, no. 2, pp. 122–130, 2011.

[171] H. H. Nguyen, J. Park, S. Kang, and M. Kim, "Surface plasmon resonance: a versatile technique for biosensor applications," *Sensors*, vol. 15, no. 5, pp. 10481–10510, 2015.

[172] H. Liao, C. L. Nehl, and J. H. Hafner, "Biomedical applications of plasmon resonant metal nanoparticles," *Nanomedicine*, vol. 1, no. 2, 2006.

[173] P. Englebienne, A. Van Hoonacker, and M. Verhas, "Surface plasmon resonance: principles, methods and applications in biomedical sciences," *Spectroscopy*, vol. 17, no. 2-3, pp. 255–273, 2003.

[174] F. J. Garcia-Vidal, A. I. Fernández-Domínguez, L. Martin-Moreno, H. C. Zhang, W. Tang, R. Peng, and T. J. Cui, "Spoof surface plasmon photonics," *Reviews of Modern Physics*, vol. 94, no. 2, p. 025004, 2022.

[175] P. Törmä and W. L. Barnes, "Strong coupling between surface plasmon polaritons and emitters: a review," *Reports on Progress in Physics*, vol. 78, no. 1, p. 013901, 2014.

[176] S. A. Maier *et al.*, *Plasmonics: fundamentals and applications*, vol. 1. Springer, 2007.

[177] I. Kriegel, F. Scotognella, and L. Manna, "Plasmonic doped semiconductor nanocrystals: Properties, fabrication, applications and perspectives," *Physics Reports*, vol. 674, pp. 1–52, 2017.

[178] F. J. Garcia de Abajo, "Graphene plasmonics: challenges and opportunities," *Acs Photonics*, vol. 1, no. 3, pp. 135–152, 2014.

USC UNIVERSIDADE DE SANTIAGO

[179] A. N. Grigorenko, M. Polini, and K. Novoselov, "Graphene plasmonics," *Nature photonics*, vol. 6, no. 11, pp. 749–758, 2012.

[180] I. Kriegel, C. Jiang, J. Rodríguez-Fernández, R. D. Schaller, D. V. Talapin, E. Da Como, and J. Feldmann, "Tuning the excitonic and plasmonic properties of copper chalcogenide nanocrystals," *Journal of the American Chemical Society*, vol. 134, no. 3, pp. 1583–1590, 2012.

[181] S. I. Bozhevolnyi, "Plasmonic nano-guides and circuits," in *Plasmonics and Metamaterials*, p. MWD3, Optica Publishing Group, 2008.

[182] M. R. Luo, *Encyclopedia of color science and technology*, vol. 392. Springer Reference, 2016.

[183] H. Raether, "Surface plasmons on gratings," *Surface plasmons on smooth and rough surfaces and on gratings*, pp. 91–116, 1988.

[184] T. Turbadar, "Complete absorption of light by thin metal films," *Proceedings of the Physical Society (1958-1967)*, vol. 73, no. 1, p. 40, 1959.

[185] E. Kretschmann and H. Raether, "Radiative decay of non radiative surface plasmons excited by light," *Zeitschrift für Naturforschung A*, vol. 23, no. 12, pp. 2135–2136, 1968.

[186] J. Renger, R. Quidant, N. van Hulst, S. Palomba, and L. Novotny, "Free-space excitation of propagating surface plasmon polaritons by nonlinear four-wave mixing," *Physical review letters*, vol. 103, no. 26, p. 266802, 2009.

[187] A. Bouhelier and G. Wiederrecht, "Excitation of broadband surface plasmon polaritons: Plasmonic continuum spectroscopy," *Physical Review B*, vol. 71, no. 19, p. 195406, 2005.

[188] A. Bouhelier and G. Wiederrecht, "Surface plasmon rainbow jets," *Optics letters*, vol. 30, no. 8, pp. 884–886, 2005.

[189] D. Basov, A. Asenjo-Garcia, P. J. Schuck, X. Zhu, and A. Rubio, "Polariton panorama," *Nanophotonics*, vol. 10, no. 1, pp. 549–577, 2021.

[190] G. Zengin, M. Wersäll, S. Nilsson, T. J. Antosiewicz, M. Käll, and T. Shegai, "Realizing strong light-matter interactions between single-nanoparticle plasmons and molecular excitons at ambient conditions," *Physical review letters*, vol. 114, no. 15, p. 157401, 2015.

[191] J. Dintinger, S. Klein, F. Bustos, W. L. Barnes, and T. Ebbesen, "Strong coupling between surface plasmon-polaritons and organic molecules in subwavelength hole arrays," *Physical Review B*, vol. 71, no. 3, p. 035424, 2005.

[192] X. Bi, Z. Li, C. Zhang, Q. You, Y. Li, Y. Wang, and P. Wang, "Strong coupling of ag@ au hollow nanocube/j-aggregate heterostructures by absorption spectra," *The Journal of Physical Chemistry C*, 2022.

[193] F. Wu, J. Guo, Y. Huang, K. Liang, L. Jin, J. Li, X. Deng, R. Jiao, Y. Liu, J. Zhang, *et al.*, "Plexcitonic optical chirality: Strong exciton–plasmon coupling in chiral j-aggregate-metal nanoparticle complexes," *ACS nano*, vol. 15, no. 2, pp. 2292–2300, 2020.

[194] N. Li, Z. Han, Y. Huang, K. Liang, X. Wang, F. Wu, X. Qi, Y. Shang, L. Yu, and B. Ding, "Strong plasmon–exciton coupling in bimetallic nanorings and nanocuboids," *Journal of Materials Chemistry C*, vol. 8, no. 23, pp. 7672–7678, 2020.

[195] D. Melnikau, A. A. Govyadinov, A. Sánchez-Iglesias, M. Grzelczak, I. R. Nabiev, L. M. Liz-Marzan, and Y. P. Rakovich, "Double rabi splitting in a strongly coupled system of core–shell au@ ag nanorods and j-aggregates of multiple fluorophores," *The Journal of Physical Chemistry Letters*, vol. 10, no. 20, pp. 6137–6143, 2019.

[196] M. Wersall, J. Cuadra, T. J. Antosiewicz, S. Balci, and T. Shegai, "Observation of mode splitting in photoluminescence of individual plasmonic nanoparticles strongly coupled to molecular excitons," *Nano letters*, vol. 17, no. 1, pp. 551–558, 2017.

[197] R. Liu, Z.-K. Zhou, Y.-C. Yu, T. Zhang, H. Wang, G. Liu, Y. Wei, H. Chen, and X.-H. Wang, "Strong light-matter interactions in single open plasmonic nanocavities at the quantum optics limit," *Physical review letters*, vol. 118, no. 23, p. 237401, 2017.

[198] P. Vasa, R. Pomraenke, G. Cirmi, E. De Re, W. Wang, S. Schwieger, D. Leipold, E. Runge, G. Cerullo, and C. Lienau, "Ultrafast manipulation of strong coupling in metal-molecular aggregate hybrid nanostructures," *Acs Nano*, vol. 4, no. 12, pp. 7559–7565, 2010.

[199] P. Vasa, W. Wang, R. Pomraenke, M. Lammers, M. Maiuri, C. Manzoni, G. Cerullo, and C. Lienau, "Real-time observation of ultrafast rabi oscillations between excitons and plasmons in metal nanostructures with j-aggregates," *Nature Photonics*, vol. 7, no. 2, pp. 128–132, 2013.

[200] Y. Kim, A. Barulin, S. Kim, L. P. Lee, and I. Kim, "Recent advances in quantum nanophotonics: plexcitonic and vibro-polaritonic strong coupling and its biomedical and chemical applications," *Nanophotonics*, 2022.

[201] Z. He, F. Li, P. Zuo, C. Xu, W. He, J. He, Y. Zhou, Q. Zhang, K. Chen, H. Huang, *et al.*, "Strong coupling in a hybrid system of silver nanoparticles and j-aggregates at room temperature," *The Journal of Physical Chemistry C*, vol. 126, no. 40, pp. 17141–17151, 2022.

[202] W. J. Tan, P. A. Thomas, I. J. Luxmoore, and W. L. Barnes, "Single vs double anti-crossing in the strong coupling between surface plasmons and molecular excitons," *The Journal of Chemical Physics*, vol. 154, no. 2, p. 024704, 2021.

[203] A. V. Ruban and M. P. Johnson, "Dynamics of higher plant photosystem cross-section associated with state transitions," *Photosynthesis Research*, vol. 99, no. 3, pp. 173–183, 2009.

[204] M. Burresi, L. Cortese, L. Pattelli, M. Kolle, P. Vukusic, D. S. Wiersma, U. Steiner, and S. Vignolini, "Bright-white beetle scales optimise multiple scattering of light," *Scientific reports*, vol. 4, no. 1, pp. 1–8, 2014.

[205] E. Moyroud, T. Wenzel, R. Middleton, P. J. Rudall, H. Banks, A. Reed, G. Mellers, P. Killoran, M. M. Westwood, U. Steiner, *et al.*, "Disorder in convergent floral nanostructures enhances signalling to bees," *Nature*, vol. 550, no. 7677, pp. 469–474, 2017.

USC UNIVERSITY OF SOUTHERN CALIFORNIA DIGITAL LIBRARY

[206] S. R. Mouchet, S. Luke, L. T. McDonald, and P. Vukusic, "Optical costs and benefits of disorder in biological photonic crystals," *Faraday Discussions*, vol. 223, pp. 9–48, 2020.

[207] A. B. Stephenson, M. Xiao, V. Hwang, L. Qu, P. A. Odorisio, M. Burke, K. Task, T. Deisenroth, S. Barkley, R. H. Darji, *et al.*, "Predicting the structural colors of films of disordered photonic balls," *arXiv preprint arXiv:2207.03033*, 2022.

[208] K. Norrman, A. Ghanbari-Siahkali, and N. Larsen, "6 studies of spin-coated polymer films," *Annual Reports Section" C"(Physical Chemistry)*, vol. 101, pp. 174–201, 2005.

[209] O. Gazzano, S. M. De Vasconcellos, K. Gauthron, C. Symonds, J. Bloch, P. Voisin, J. Bellessa, A. Lemaître, and P. Senellart, "Evidence for confined tamm plasmon modes under metallic microdisks and application to the control of spontaneous optical emission," *Physical review letters*, vol. 107, no. 24, p. 247402, 2011.

[210] C. Symonds, G. Lheureux, J. P. Hugonin, J. J. Greffet, J. Laverdant, G. Brucoli, A. Lemaitre, P. Senellart, and J. Bellessa, "Confined tamm plasmon lasers," *Nano letters*, vol. 13, no. 7, pp. 3179–3184, 2013.

[211] W. T. Thomson, "Transmission of elastic waves through a stratified solid medium," *Journal of applied Physics*, vol. 21, no. 2, pp. 89–93, 1950.

[212] T. G. Mackay and A. Lakhtakia, "The transfer-matrix method in electromagnetics and optics," *Synthesis lectures on electromagnetics*, vol. 1, no. 1, pp. 1–126, 2020.

[213] F. Aziz and A. F. Ismail, "Spray coating methods for polymer solar cells fabrication: A review," *Materials Science in Semiconductor Processing*, vol. 39, pp. 416–425, 2015.

[214] S. J. Weinstein and K. J. Ruschak, "Coating flows," *Annual Review of Fluid Mechanics*, vol. 36, p. 29, 2004.

[215] C. J. Brinker, "Dip coating," in *Chemical Solution Deposition of Functional Oxide Thin Films*, pp. 233–261, Springer, 2013.

[216] A. G. Emslie, F. T. Bonner, and L. G. Peck, "Flow of a viscous liquid on a rotating disk," *Journal of Applied Physics*, vol. 29, no. 5, pp. 858–862, 1958.

[217] R. Das and A. Chanda, "Fabrication and properties of spin-coated polymer films," in *Nano-size Polymers*, pp. 283–306, Springer, 2016.

[218] D. Meyerhofer, "Characteristics of resist films produced by spinning," *Journal of Applied Physics*, vol. 49, no. 7, pp. 3993–3997, 1978.

[219] N. Sahu, B. Parija, and S. Panigrahi, "Fundamental understanding and modeling of spin coating process: A review," *Indian Journal of Physics*, vol. 83, no. 4, pp. 493–502, 2009.

[220] M. Tyona, "A theoritical study on spin coating technique," *Advances in materials Research*, vol. 2, no. 4, p. 195, 2013.

[221] D. Bornside, C. Macosko, and L. Scriven, "Spin coating: One-dimensional model," *Journal of Applied Physics*, vol. 66, no. 11, pp. 5185–5193, 1989.

USC UNIVERSIDADE DE SANTIAGO DE COMPOSTELA

[222] C. Lawrence, "The mechanics of spin coating of polymer films," *The Physics of fluids*, vol. 31, no. 10, pp. 2786–2795, 1988.

[223] B. Washo, "Rheology and modeling of the spin coating process," *IBM Journal of Research and Development*, vol. 21, no. 2, pp. 190–198, 1977.

[224] D. Bornside, C. Macosko, and L. Scriven, "Modeling of spin coating.," *Journal of imaging technology*, vol. 13, no. 4, pp. 122–130, 1987.

[225] J. Griffin, H. Hassan, and E. Spooner, "Spin coating: Complete guide to theory and techniques." https://www.ossila.com/en-eu/pages/spin-coating. Accessed on 2022-07-01.

[226] H. Fujiwara, *Spectroscopic ellipsometry: principles and applications*. John Wiley & Sons, 2007.

[227] M. Kimura, K. Okahara, and T. Miyamoto, "Tunable multilayer-film distributed-bragg-reflector filter," *Journal of Applied Physics*, vol. 50, no. 3, pp. 1222–1225, 1979.

[228] A. Alvarez, J. Tito, M. Vaello, P. Velasquez, R. Mallavia, M. Sanchez-Lopez, and S. F. de Avila, "Polymeric multilayers for integration into photonic devices," *Thin Solid Films*, vol. 433, no. 1-2, pp. 277–280, 2003.

[229] J. Bailey and J. S. Sharp, "Thin film polymer photonics: Spin cast distributed bragg reflectors and chirped polymer structures," *The European Physical Journal E*, vol. 33, no. 1, pp. 41–49, 2010.

[230] W. Mönch, J. Dehnert, E. Jaufmann, and H. Zappe, "Flory-huggins swelling of polymer bragg mirrors," *Applied physics letters*, vol. 89, no. 16, p. 164104, 2006.

[231] G. Iasilli, R. Francischello, P. Lova, S. Silvano, A. Surace, G. Pesce, M. Alloisio, M. Patrini, M. Shimizu, D. Comoretto, *et al.*, "Luminescent solar concentrators: Boosted optical efficiency by polymer dielectric mirrors," *Materials chemistry frontiers*, vol. 3, no. 3, pp. 429–436, 2019.

[232] L. M. Goldenberg, V. Lisinetskii, and S. Schrader, "Fast and simple fabrication of organic bragg mirrors—application to plastic microchip lasers," *Laser Physics Letters*, vol. 10, no. 5, p. 055808, 2013.

[233] G. Kamita, M. Kolle, F. Huang, J. J. Baumberg, and U. Steiner, "Multilayer mirrored bubbles with spatially-chirped and elastically-tuneable optical bandgaps," *Optics express*, vol. 20, no. 6, pp. 6421–6428, 2012.

[234] X. Lai, J. Peng, Q. Cheng, A. P. Tomsia, G. Zhao, L. Liu, G. Zou, Y. Song, L. Jiang, and M. Li, "Bioinspired color switchable photonic crystal silicone elastomer kirigami," *Angewandte Chemie*, vol. 133, no. 26, pp. 14428–14433, 2021.

[235] F. Scotognella, A. Monguzzi, F. Meinardi, and R. Tubino, "Dfb laser action in a flexible fully plastic multilayer," *Physical Chemistry Chemical Physics*, vol. 12, no. 2, pp. 337–340, 2009.

USC UNIVERSIDAD DE SANTIAGO

[236] M. Kolle, B. Zheng, N. Gibbons, J. J. Baumberg, and U. Steiner, "Stretch-tuneable dielectric mirrors and optical microcavities," *Optics express*, vol. 18, no. 5, pp. 4356–4364, 2010.

[237] B. H. Miller, H. Liu, and M. Kolle, "Scalable optical manufacture of dynamic structural colour in stretchable materials," *Nature Materials*, pp. 1–5, 2022.

[238] A. Inoue, T. Komikado, K. Kinoshita, J. Hayashi, and S. Umegaki, "Deformable mirror for mechanical q-switching of laser-diode-pumped microchip laser," *Japanese Journal of Applied Physics*, vol. 46, no. 11L, p. L1016, 2007.

[239] R. Zhang, Q. Wang, and X. Zheng, "Flexible mechanochromic photonic crystals: routes to visual sensors and their mechanical properties," *Journal of Materials Chemistry C*, vol. 6, no. 13, pp. 3182–3199, 2018.

[240] P. Lova, G. Manfredi, and D. Comoretto, "Advances in functional solution processed planar 1d photonic crystals," *Advanced Optical Materials*, vol. 6, no. 24, p. 1800730, 2018.

[241] M. Malekovic, M. Urann, U. Steiner, B. D. Wilts, and M. Kolle, "Soft photonic fibers for colorimetric solvent vapor sensing," *Advanced Optical Materials*, vol. 8, no. 13, p. 2000165, 2020.

[242] M. Portnoi, T. J. Macdonald, C. Sol, T. S. Robbins, T. Li, J. Schläfer, S. Guldin, I. P. Parkin, and I. Papakonstantinou, "All-silicone-based distributed bragg reflectors for efficient flexible luminescent solar concentrators," *Nano Energy*, vol. 70, p. 104507, 2020.

[243] M. E. Calvo, L. González-García, J. Parra-Barranco, A. Barranco, A. Jiménez-Solano, A. R. González-Elipe, and H. Míguez, "Flexible distributed bragg reflectors from nanocolumnar templates," *Advanced Optical Materials*, vol. 3, no. 2, pp. 171–175, 2015.

[244] Y. Li, M. E. Calvo, and H. Míguez, "Integration of photonic crystals into flexible dye solar cells: a route toward bendable and adaptable optoelectronic devices displaying structural color and enhanced efficiency," *Advanced Optical Materials*, vol. 4, no. 3, pp. 464–471, 2016.

[245] M. E. Calvo and H. Míguez, "Flexible, adhesive, and biocompatible bragg mirrors based on polydimethylsiloxane infiltrated nanoparticle multilayers," *Chemistry of Materials*, vol. 22, no. 13, pp. 3909–3915, 2010.

[246] H. R. M. Garcia and M. E. C. Roggiani, "Method for obtaining a flexible bragg mirror and bragg mirror obtained using said method," Jan. 26 2012. US Patent App. 13/192,652.

[247] T. Sai, M. Saba, E. R. Dufresne, U. Steiner, and B. D. Wilts, "Designing refractive index fluids using the kramers–kronig relations," *Faraday Discussions*, vol. 223, pp. 136–144, 2020.

[248] M. Yasir, T. Sai, A. Sicher, F. Scheffold, U. Steiner, B. D. Wilts, and E. R. Dufresne, "Enhancing the refractive index of polymers with a plant-based pigment," *Small*, vol. 17, no. 44, p. 2103061, 2021.

USC UNIVERSIDAD DE SANTIAGO DE COMPOSTELA

[249] P. Vukusic and D. Stavenga, "Physical methods for investigating structural colours in biological systems," *Journal of the Royal Society Interface*, vol. 6, no. suppl_2, pp. S133–S148, 2009.

[250] J. W. Goessling, Y. Su, C. Maibohm, M. Ellegaard, and M. Kühl, "Differences in the optical properties of valve and girdle band in a centric diatom," *Journal of the Royal Society Interface Focus*, vol. 9, no. 1, p. 20180031, 2019.

[251] H. Noh, S. F. Liew, V. Saranathan, S. G. Mochrie, R. O. Prum, E. R. Dufresne, and H. Cao, "How noniridescent colors are generated by quasi-ordered structures of bird feathers," *Advanced Materials*, vol. 22, no. 26-27, pp. 2871–2880, 2010.

[252] D. Stavenga, H. Leertouwer, P. Pirih, and M. Wehling, "Imaging scatterometry of butterfly wing scales," *Optics Express*, vol. 17, no. 1, pp. 193–202, 2009.

[253] H. Gersen, T. Karle, R. Engelen, W. Bogaerts, J. P. Korterik, N. Van Hulst, T. Krauss, and L. Kuipers, "Direct observation of bloch harmonics and negative phase velocity in photonic crystal waveguides," *Physical review letters*, vol. 94, no. 12, p. 123901, 2005.

[254] R. J. Engelen, Y. Sugimoto, H. Gersen, N. Ikeda, K. Asakawa, and L. K. Kuipers, "Ultrafast evolution of photonic eigenstates in k-space," *Nature Physics*, vol. 3, no. 6, pp. 401–405, 2007.

[255] Y. Zhang, M. Zhao, J. Wang, W. Liu, B. Wang, S. Hu, G. Lu, A. Chen, J. Cui, W. Zhang, *et al.*, "Momentum-space imaging spectroscopy for the study of nanophotonic materials," *Science Bulletin*, vol. 66, no. 8, pp. 824–838, 2021.

[256] C. Lai, N. Kim, S. Utsunomiya, G. Roumpos, H. Deng, M. Fraser, T. Byrnes, P. Recher, N. Kumada, T. Fujisawa, *et al.*, "Coherent zero-state and π-state in an exciton–polariton condensate array," *Nature*, vol. 450, no. 7169, pp. 529–532, 2007.

[257] M. A. Lieb, J. M. Zavislan, and L. Novotny, "Single-molecule orientations determined by direct emission pattern imaging," *JOSA B*, vol. 21, no. 6, pp. 1210–1215, 2004.

[258] W. P. Wardley, J. W. Goessling, and M. Lopez-Garcia, "Measuring photonics in photosynthesis: Combined micro-fourier image spectroscopy and pulse amplitude modulated chlorophyll fluorimetry at the micrometre-scale," *Biomimetics*, vol. 7, no. 3, p. 107, 2022.

[259] E. Hecht, *Optics*. Pearson Education India, 2012.

[260] V. N. Mahajan, *Fundamentals of geometrical optics*, vol. 1. SPIE Press, 2014.

[261] S.-U. Hwang and Y.-G. Lee, "Simulation of an oil immersion objective lens: a simplified ray-optics model considering abbe's sine condition," *Optics express*, vol. 16, no. 26, pp. 21170–21183, 2008.

[262] L. Dai, I. Gregor, I. von der Hocht, T. Ruckstuhl, and J. Enderlein, "Measuring large numerical apertures by imaging the angular distribution of radiation of fluorescing molecules," *Optics express*, vol. 13, no. 23, pp. 9409–9414, 2005.

USC UNIVERSIDADE DE

[263] S. American, "How does a spectrograph work?." https://www.scientificamerican.com/article/ancient-stars-how-does-spectrograph-work/#. Accessed on 2022-09-26.

[264] V. Mascoli, A. F. Bhatti, L. Bersanini, H. van Amerongen, and R. Croce, "The antenna of far-red absorbing cyanobacteria increases both absorption and quantum efficiency of photosystem ii," *Nature communications*, vol. 13, no. 1, pp. 1–8, 2022.

[265] T. B. Arp, J. Kistner-Morris, V. Aji, R. J. Cogdell, R. van Grondelle, and N. M. Gabor, "Quieting a noisy antenna reproduces photosynthetic light-harvesting spectra," *Science*, vol. 368, no. 6498, pp. 1490–1495, 2020.

[266] A. Qiu, H. Perryman, O.-P. Phrathep, H. Whitney, and R. Oulton, "Active nanophotonic structure in iridoplasts of begonias," in *Active Photonic Platforms XII*, vol. 11461, p. 114610F, SPIE, 2020.

[267] K. S. Menghrajani, A. B. Vasista, W. J. Tan, and W. L. Barnes, "Molecular strong coupling: an exploration employing open, half-and full planar cavities," *arXiv preprint arXiv:2211.08300*, 2022.

[268] X. Xiong, A. del Campo, and J. Cui, "Photoresponsive polymers," in *Smart polymers and their applications*, pp. 87–153, Elsevier, 2019.

[269] M. Irie, "Photoresponsive polymers," in *New polymer materials*, pp. 27–67, Springer, 1990.

[270] A. Othonos, "Fiber bragg gratings," *Review of scientific instruments*, vol. 68, no. 12, pp. 4309–4341, 1997.

[271] S. Tomljenovic-Hanic, M. Steel, C. M. de Sterke, and D. J. Moss, "High-q cavities in photosensitive photonic crystals," *Optics Letters*, vol. 32, no. 5, pp. 542–544, 2007.

[272] L. Wu, Y. Zhong, C. T. Chan, K. S. Wong, and G. P. Wang, "Fabrication of large area two-and three-dimensional polymer photonic crystals using single refracting prism holographic lithography," *Applied Physics Letters*, vol. 86, no. 24, p. 241102, 2005.

[273] I. Divliansky, T. S. Mayer, K. S. Holliday, and V. H. Crespi, "Fabrication of three-dimensional polymer photonic crystal structures using single diffraction element interference lithography," *Applied Physics Letters*, vol. 82, no. 11, pp. 1667–1669, 2003.

[274] A. Kopyshev, C. J. Galvin, R. R. Patil, J. Genzer, N. Lomadze, D. Feldmann, J. Zakrevski, and S. Santer, "Light-induced reversible change of roughness and thickness of photosensitive polymer brushes," *ACS Applied Materials & Interfaces*, vol. 8, no. 29, pp. 19175–19184, 2016.

[275] J. Jelken and S. Santer, "Light induced reversible structuring of photosensitive polymer films," *RSC advances*, vol. 9, no. 35, pp. 20295–20305, 2019.

[276] P. Lova, G. Manfredi, L. Boarino, A. Comite, M. Laus, M. Patrini, F. Marabelli, C. Soci, and D. Comoretto, "Polymer distributed bragg reflectors for vapor sensing," *Acs Photonics*, vol. 2, no. 4, pp. 537–543, 2015.

USC UNIVERSIDADE DE SANTIAGO DE COMPOSTELA

[277] K. E. Carroll, C. Zhang, D. J. Webb, K. Kalli, A. Argyros, and M. C. Large, "Thermal response of bragg gratings in pmma microstructured optical fibers," *Optics express*, vol. 15, no. 14, pp. 8844–8850, 2007.

[278] M. Schmidt, M. Eich, U. Huebner, and R. Boucher, "Electro-optically tunable photonic crystals," *Applied Physics Letters*, vol. 87, no. 12, p. 121110, 2005.

[279] I. Liberal and N. Engheta, "Nonradiating and radiating modes excited by quantum emitters in open epsilon-near-zero cavities," *Science advances*, vol. 2, no. 10, p. e1600987, 2016.

[280] S. Enoch, G. Tayeb, P. Sabouroux, N. Guérin, and P. Vincent, "A metamaterial for directive emission," *Physical review letters*, vol. 89, no. 21, p. 213902, 2002.

[281] M. Silveirinha and N. Engheta, "Tunneling of electromagnetic energy through subwavelength channels and bends using ε-near-zero materials," *Physical review letters*, vol. 97, no. 15, p. 157403, 2006.

[282] M. Z. Alam, I. De Leon, and R. W. Boyd, "Large optical nonlinearity of indium tin oxide in its epsilon-near-zero region," *Science*, vol. 352, no. 6287, pp. 795–797, 2016.

[283] I. Liberal and N. Engheta, "Near-zero refractive index photonics," *Nature Photonics*, vol. 11, no. 3, pp. 149–158, 2017.

[284] N. Kinsey, C. DeVault, A. Boltasseva, and V. M. Shalaev, "Near-zero-index materials for photonics," *Nature Reviews Materials*, vol. 4, no. 12, pp. 742–760, 2019.

[285] F. Naccarato, F. Ricci, J. Suntivich, G. Hautier, L. Wirtz, and G.-M. Rignanese, "Searching for materials with high refractive index and wide band gap: A first-principles high-throughput study," *Physical Review Materials*, vol. 3, no. 4, p. 044602, 2019.

[286] R. C. Devlin, M. Khorasaninejad, W. T. Chen, J. Oh, and F. Capasso, "Broadband high-efficiency dielectric metasurfaces for the visible spectrum," *Proceedings of the National Academy of Sciences*, vol. 113, no. 38, pp. 10473–10478, 2016.

[287] R. Nagarajan, C. H. Joyner, R. P. Schneider, J. S. Bostak, T. Butrie, A. G. Dentai, V. G. Dominic, P. W. Evans, M. Kato, M. Kauffman, *et al.*, "Large-scale photonic integrated circuits," *IEEE Journal of Selected Topics in Quantum Electronics*, vol. 11, no. 1, pp. 50–65, 2005.

[288] J. B. Khurgin, "Expanding the photonic palette: Exploring high index materials," *ACS Photonics*, vol. 9, no. 3, pp. 743–751, 2022.

[289] H. Shim, Z. Kuang, and O. D. Miller, "Optical materials for maximal nanophotonic response," *Optical Materials Express*, vol. 10, no. 7, pp. 1561–1585, 2020.

[290] E. H. Korte and A. Röseler, "Infrared reststrahlen revisited: commonly disregarded optical details related to n< 1," *Analytical and bioanalytical chemistry*, vol. 382, no. 8, pp. 1987–1992, 2005.

USC UNIVERSIDADE DE SANTIAGO

[291] A. Kavokin, I. Shelykh, and G. Malpuech, "Lossless interface modes at the boundary between two periodic dielectric structures," *Physical Review B*, vol. 72, no. 23, p. 233102, 2005.

[292] C. Kar, S. Jena, D. V. Udupa, and K. D. Rao, "Tamm plasmon polariton in planar structures: A brief overview and applications," *arXiv preprint arXiv:2211.05095*, 2022.

[293] M. Sasin, R. Seisyan, M. Kalitteevski, S. Brand, R. Abram, J. Chamberlain, A. Y. Egorov, A. Vasil'Ev, V. Mikhrin, and A. Kavokin, "Tamm plasmon polaritons: Slow and spatially compact light," *Applied physics letters*, vol. 92, no. 25, p. 251112, 2008.

[294] K. E. McGhee, R. Jayaprakash, K. Georgiou, S. L. Burg, and D. G. Lidzey, "Polariton condensation in a microcavity using a highly-stable molecular dye," *Journal of Materials Chemistry C*, vol. 10, no. 11, pp. 4187–4195, 2022.

[295] J. Kasprzak, M. Richard, S. Kundermann, A. Baas, P. Jeambrun, J. M. J. Keeling, F. Marchetti, M. Szymańska, R. André, J. Staehli, *et al.*, "Bose–einstein condensation of exciton polaritons," *Nature*, vol. 443, no. 7110, pp. 409–414, 2006.

[296] T. Byrnes, N. Y. Kim, and Y. Yamamoto, "Exciton–polariton condensates," *Nature Physics*, vol. 10, no. 11, pp. 803–813, 2014.

[297] S. Tsintzos, N. Pelekanos, G. Konstantinidis, Z. Hatzopoulos, and P. Savvidis, "A gaas polariton light-emitting diode operating near room temperature," *Nature*, vol. 453, no. 7193, pp. 372–375, 2008.

[298] C. Schneider, K. Winkler, M. D. Fraser, M. Kamp, Y. Yamamoto, E. Ostrovskaya, and S. Höfling, "Exciton-polariton trapping and potential landscape engineering," *Reports on Progress in Physics*, vol. 80, no. 1, p. 016503, 2016.

[299] T. Liew, A. Kavokin, T. Ostatnickỳ, M. Kaliteevski, I. Shelykh, and R. Abram, "Exciton-polariton integrated circuits," *Physical review B*, vol. 82, no. 3, p. 033302, 2010.

[300] D. Bajoni, "Polariton lasers. hybrid light–matter lasers without inversion," *Journal of Physics D: Applied Physics*, vol. 45, no. 31, p. 313001, 2012.

[301] B. Liu, X. Huang, S. Hou, D. Fan, and S. R. Forrest, "Photocurrent generation following long-range propagation of organic exciton–polaritons," *Optica*, vol. 9, no. 9, pp. 1029–1036, 2022.

[302] J. Gerard, D. Barrier, J. Marzin, R. Kuszelewicz, L. Manin, E. Costard, V. Thierry-Mieg, and T. Rivera, "Quantum boxes as active probes for photonic microstructures: The pillar microcavity case," *Applied Physics Letters*, vol. 69, no. 4, pp. 449–451, 1996.

[303] G. R. Hadley, "Effective index model for vertical-cavity surface-emitting lasers," *Optics Letters*, vol. 20, no. 13, pp. 1483–1485, 1995.

[304] M. Adams, B. Cemlyn, I. Henning, M. Parker, E. Harbord, and R. Oulton, "Model for confined tamm plasmon devices," *JOSA B*, vol. 36, no. 1, pp. 125–130, 2019.

USC UNIVERSIDADE DE SANTIAGO DE COMPOSTELA

[305] G. Lecamp, P. Lalanne, J. P. Hugonin, and J.-M. Gerard, "Energy transfer through laterally confined bragg mirrors and its impact on pillar microcavities," *IEEE journal of quantum electronics*, vol. 41, no. 10, pp. 1323–1329, 2005.

[306] N. Gregersen, P. Kaer, and J. Mørk, "Modeling and design of high-efficiency single-photon sources," *IEEE Journal of selected topics in quantum electronics*, vol. 19, no. 5, pp. 1–16, 2013.

[307] N. Gregersen, S. Reitzenstein, C. Kistner, M. Strauss, C. Schneider, S. Höfling, L. Worschech, A. Forchel, T. R. Nielsen, J. Mørk, *et al.*, "Numerical and experimental study of the q factor of high-q micropillar cavities," *IEEE Journal of Quantum Electronics*, vol. 46, no. 10, pp. 1470–1483, 2010.

[308] S. Reitzenstein, N. Gregersen, C. Kistner, M. Strauss, C. Schneider, L. Pan, T. R. Nielsen, S. Höfling, J. Mørk, and A. Forchel, "Oscillatory variations in the q factors of high quality micropillar cavities," *Applied Physics Letters*, vol. 94, no. 6, p. 061108, 2009.

[309] Y. Yamamoto, S. Machida, and G. Björk, "Microcavity semiconductor laser with enhanced spontaneous emission," *Physical Review A*, vol. 44, no. 1, p. 657, 1991.

[310] G. Lheureux, S. Azzini, C. Symonds, P. Senellart, A. Lemaître, C. Sauvan, J.-P. Hugonin, J.-J. Greffet, and J. Bellessa, "Polarization-controlled confined tamm plasmon lasers," *ACS photonics*, vol. 2, no. 7, pp. 842–848, 2015.

[311] C. Symonds, S. Azzini, G. Lheureux, A. Piednoir, J.-M. Benoit, A. Lemaitre, P. Senellart, and J. Bellessa, "High quality factor confined tamm modes," *Scientific Reports*, vol. 7, no. 1, pp. 1–7, 2017.

[312] B. H. Cumpston and K. F. Jensen, "Photo-oxidation of polymers used in electroluminescent devices," *Synthetic Metals*, vol. 73, no. 3, pp. 195–199, 1995.

[313] T. Ha and P. Tinnefeld, "Photophysics of fluorescence probes for single molecule biophysics and super-resolution imaging," *Annual review of physical chemistry*, vol. 63, p. 595, 2012.

[314] A. Diaspro, G. Chirico, C. Usai, P. Ramoino, and J. Dobrucki, "Photobleaching," in *Handbook of biological confocal microscopy*, pp. 690–702, Springer, 2006.

[315] A. Gassenq, K. Chevrier, A. Bard, J.-M. Benoit, C. Symonds, and J. Bellessa, "Selective grating obtained by dye microstructuration based on local photobleaching using a laser writer," *Applied optics*, vol. 59, no. 19, pp. 5697–5701, 2020.

[316] K. Chevrier, J.-M. Benoit, C. Symonds, S. Saikin, J. Yuen-Zhou, and J. Bellessa, "Anisotropy and controllable band structure in suprawavelength polaritonic metasurfaces," *Physical Review Letters*, vol. 122, no. 17, p. 173902, 2019.

[317] A. Cacciola, C. Triolo, O. Di Stefano, A. Genco, M. Mazzeo, R. Saija, S. Patanè, and S. Savasta, "Subdiffraction light concentration by j-aggregate nanostructures," *ACS Photonics*, vol. 2, no. 7, pp. 971–979, 2015.

USC UNIVERSIDAD DE SANTIAGO DE

[318] A. Gassenq, K. Chevrier, A. Bard, J.-M. Benoit, C. Symonds, and J. Bellessa, "Study of dye local photo-bleaching obtained by uv lithography for photonics applications," in *2021 Conference on Lasers and Electro-Optics Europe & European Quantum Electronics Conference (CLEO/Europe-EQEC)*, pp. 1–1, IEEE, 2021.

[319] S. Bonfadini, T. Nicolini, F. Storti, N. Stingelin, G. Lanzani, and L. Criante, "Femtosecond laser-induced refractive index patterning in inorganic/organic hybrid films," *Advanced Photonics Research*, p. 2100257, 2022.

[320] A. Gassenq, Y. Pipon, G. Montagnac, O. Boisron, V. Martinez, A. Bard, J.-m. Benoit, C. Symonds, and J. Bellessa, "Raman investigation of local photo-bleaching in tdbc dye layer for photonics applications," *Journal of Raman Spectroscopy*, vol. 53, no. 4, pp. 755–761, 2022.

[321] "Fdtd lumerical." https://www.lumerical.com/. Accessed on 2022-07-22.

[322] A. B. Vasista, K. S. Menghrajani, and W. L. Barnes, "Polariton assisted photoemission from a layered molecular material: role of vibrational states and molecular absorption," *Nanoscale*, vol. 13, no. 34, pp. 14497–14505, 2021.

[323] T. Baba, T. Hamano, F. Koyama, and K. Iga, "Spontaneous emission factor of a microcavity dbr surface-emitting laser," *IEEE Journal of Quantum Electronics*, vol. 27, no. 6, pp. 1347–1358, 1991.

[324] J.-M. Gérard, B. Sermage, B. Gayral, B. Legrand, E. Costard, and V. Thierry-Mieg, "Enhanced spontaneous emission by quantum boxes in a monolithic optical microcavity," *Physical review letters*, vol. 81, no. 5, p. 1110, 1998.

[325] J. Jewell, A. Scherer, S. McCall, Y.-H. Lee, S. Walker, J. Harbison, and L. Florez, "Low threshold electrically-pumped vertical-cavity surface-emitting micro-lasers," *Optics News*, vol. 15, no. 12, pp. 10–11, 1989.

[326] R. Michalzik, "Vcsel fundamentals," in *VCSELs*, pp. 19–75, Springer, 2013.

[327] J. L. Jewell, J. Harbison, A. Scherer, Y.-H. Lee, and L. Florez, "Vertical-cavity surface-emitting lasers: design, growth, fabrication, characterization," *IEEE Journal of Quantum Electronics*, vol. 27, no. 6, pp. 1332–1346, 1991.

[328] J. Jewell, S. McCall, A. Scherer, H. Houh, N. Whitaker, A. Gossard, and J. English, "Transverse modes, waveguide dispersion, and 30 ps recovery in submicron gaas/alas microresonators," *Applied physics letters*, vol. 55, no. 1, pp. 22–24, 1989.

[329] M. Seo and M. Lee, "Surface plasmon resonance and coloration in stainless steel with a 2d periodic texture," *Applied Physics A*, vol. 125, no. 9, pp. 1–9, 2019.

[330] W. L. Barnes, T. Preist, S. Kitson, and J. Sambles, "Physical origin of photonic energy gaps in the propagation of surface plasmons on gratings," *Physical Review B*, vol. 54, no. 9, p. 6227, 1996.

USC UNIVERSIDADE DE SANTIAGO DE COMPOSTELA

[331] W. Barnes, T. Preist, S. Kitson, J. Sambles, N. Cotter, and D. Nash, "Photonic gaps in the dispersion of surface plasmons on gratings," *Physical Review B*, vol. 51, no. 16, p. 11164, 1995.

[332] S. Park, G. Lee, S. H. Song, C. H. Oh, and P. S. Kim, "Resonant coupling of surface plasmons to radiation modes by use of dielectric gratings," *Optics letters*, vol. 28, no. 20, pp. 1870–1872, 2003.

[333] H. L. Offerhaus, B. Van Den Bergen, M. Escalante, F. B. Segerink, J. P. Korterik, and N. Van Hulst, "Creating focused plasmons by noncollinear phasematching on functional gratings," *Nano letters*, vol. 5, no. 11, pp. 2144–2148, 2005.

[334] H. Zhang, B. Abhiraman, Q. Zhang, J. Miao, K. Jo, S. Roccasecca, M. W. Knight, A. R. Davoyan, and D. Jariwala, "Hybrid exciton-plasmon-polaritons in van der waals semiconductor gratings," *Nature communications*, vol. 11, no. 1, pp. 1–9, 2020.

[335] M. S. Rider, R. Arul, J. J. Baumberg, and W. L. Barnes, "Theory of strong coupling between molecules and surface plasmons on a grating," *arXiv preprint arXiv:2205.12745*, 2022.

[336] Q. Wang, Y. Zheng, C. Yu, X. Chen, E. Wang, S. Long, H. Zhu, S. Gao, and J. Cao, "Fabrication of silver-silicon gratings for surface plasmon excitation using nanosecond laser interference lithography," *Plasmonics*, vol. 15, no. 6, pp. 1639–1644, 2020.

[337] E. Nadal, N. Barros, H. Glénat, J. Laverdant, D. Schmool, and H. Kachkachi, "Plasmon-enhanced diffraction in nanoparticle gratings fabricated by in situ photo-reduction of gold chloride doped polymer thin films by laser interference patterning," *Journal of Materials Chemistry C*, vol. 5, no. 14, pp. 3553–3560, 2017.

[338] C. Lertvachirapaiboon, R. Yamazaki, P. Pienpinijtham, A. Baba, S. Ekgasit, C. Thammacharoen, K. Shinbo, K. Kato, and F. Kaneko, "Solution-based fabrication of gold grating film for use as a surface plasmon resonance sensor chip," *Sensors and Actuators B: Chemical*, vol. 173, pp. 316–321, 2012.

[339] K. Nakamoto, R. Kurita, and O. Niwa, "Electrochemical surface plasmon resonance measurement based on gold nanohole array fabricated by nanoimprinting technique," *Analytical chemistry*, vol. 84, no. 7, pp. 3187–3191, 2012.

[340] G. Turnbull, P. Andrew, M. Jory, W. L. Barnes, and I. Samuel, "Relationship between photonic band structure and emission characteristics of a polymer distributed feedback laser," *Physical Review B*, vol. 64, no. 12, p. 125122, 2001.

[341] Z. Hirboodvash, M. Khodami, N. R. Fong, E. Lisicka-Skrzek, A. Olivieri, H. Northfield, R. N. Tait, and P. Berini, "Grating couplers fabricated by e-beam lithography for long-range surface plasmon waveguides embedded in a fluoropolymer," *Applied optics*, vol. 58, no. 11, pp. 2994–3002, 2019.

[342] M. Mazloumi, Y. Bdour, C. Escobedo, and R. G. Sabat, "Biomimetic macroscopic hierarchical moire gratings," *Applied Optics*, vol. 61, no. 18, pp. 5428–5434, 2022.

USC UNIVERSIDADE DE SANTIAGO DE COMPOSTELA

[343] S. Olcum, A. Kocabas, G. Ertas, A. Atalar, and A. Aydinli, "Tunable surface plasmon resonance on an elastomeric substrate," *Optics express*, vol. 17, no. 10, pp. 8542–8547, 2009.

[344] R. Lin, Y. Qi, D. Kou, W. Ma, and S. Zhang, "Bio-inspired wrinkled photonic elastomer with superior controllable and mechanically stable structure for multi-mode color display," *Advanced Functional Materials*, p. 2207691, 2022.

[345] C. Tian, H.-P. Ji, C.-Y. Zong, and C.-H. Lu, "Controlled fabrication of hierarchically microstructured surfaces via surface wrinkling combined with template replication," *Chinese Chemical Letters*, vol. 26, no. 1, pp. 15–20, 2015.

[346] N. Bowden, S. Brittain, A. G. Evans, J. W. Hutchinson, and G. M. Whitesides, "Spontaneous formation of ordered structures in thin films of metals supported on an elastomeric polymer," *nature*, vol. 393, no. 6681, pp. 146–149, 1998.

[347] K.-S. Koh, J. Chin, J. Chia, and C.-L. Chiang, "Quantitative studies on pdms-pdms interface bonding with piranha solution and its swelling effect," *Micromachines*, vol. 3, no. 2, pp. 427–441, 2012.

[348] N. Bowden, W. T. Huck, K. E. Paul, and G. M. Whitesides, "The controlled formation of ordered, sinusoidal structures by plasma oxidation of an elastomeric polymer," *Applied physics letters*, vol. 75, no. 17, pp. 2557–2559, 1999.

[349] J. Y. Chung, A. J. Nolte, and C. M. Stafford, "Surface wrinkling: a versatile platform for measuring thin-film properties," *Advanced materials*, vol. 23, no. 3, pp. 349–368, 2011.

[350] A. Schweikart and A. Fery, "Controlled wrinkling as a novel method for the fabrication of patterned surfaces," *Microchimica Acta*, vol. 165, no. 3, pp. 249–263, 2009.

[351] S. Yang, K. Khare, and P.-C. Lin, "Harnessing surface wrinkle patterns in soft matter," *Advanced Functional Materials*, vol. 20, no. 16, pp. 2550–2564, 2010.

[352] M. Barelli, D. Repetto, and F. B. de Mongeot, "Infrared plasmonics via self-organized anisotropic wrinkling of au/pdms nanoarrays," *ACS Applied Polymer Materials*, vol. 1, no. 6, pp. 1334–1340, 2019.

[353] J. B. Kim, P. Kim, N. C. Pégard, S. J. Oh, C. R. Kagan, J. W. Fleischer, H. A. Stone, and Y.-L. Loo, "Wrinkles and deep folds as photonic structures in photovoltaics," *Nature Photonics*, vol. 6, no. 5, pp. 327–332, 2012.

[354] J. Y. Chung, J. P. Youngblood, and C. M. Stafford, "Anisotropic wetting on tunable micro-wrinkled surfaces," *Soft Matter*, vol. 3, no. 9, pp. 1163–1169, 2007.

[355] D. Chandra, S. Yang, and P.-C. Lin, "Strain responsive concave and convex microlens arrays," *Applied Physics Letters*, vol. 91, no. 25, p. 251912, 2007.

[356] C. M. Stafford, C. Harrison, K. L. Beers, A. Karim, E. J. Amis, M. R. VanLandingham, H.-C. Kim, W. Volksen, R. D. Miller, and E. E. Simonyi, "A buckling-based metrology for measuring the elastic moduli of polymeric thin films," *Nature materials*, vol. 3, no. 8, pp. 545–550, 2004.

USC UNIVERSIDADE DE SANTIAGO DE COMPOSTELA

[357] C. Mirley and J. Koberstein, "A room temperature method for the preparation of ultrathin siox films from langmuir-blodgett layers," *Langmuir*, vol. 11, no. 4, pp. 1049–1052, 1995.

[358] D. Bodas and C. Khan-Malek, "Hydrophilization and hydrophobic recovery of pdms by oxygen plasma and chemical treatment—an sem investigation," *Sensors and actuators B: chemical*, vol. 123, no. 1, pp. 368–373, 2007.

[359] M. A. Biot, "Bending of an infinite beam on an elastic foundation," *Journal of Applied Mathematics and Mechanics*, vol. 2, no. 3, pp. 165–184, 1922.

[360] J. Genzer and K. Efimenko, "Creating long-lived superhydrophobic polymer surfaces through mechanically assembled monolayers," *Science*, vol. 290, no. 5499, pp. 2130–2133, 2000.

[361] K. Efimenko and J. Genzer, "How to prepare tunable planar molecular chemical gradients," *Advanced Materials*, vol. 13, no. 20, pp. 1560–1563, 2001.

[362] A. Tan, L. Pellegrino, Z. Ahmad, and J. T. Cabral, "Tunable structural color with gradient and multiaxial polydimethylsiloxane wrinkling," *Advanced Optical Materials*, p. 2200964, 2022.

[363] W. Qiao, W. Huang, Y. Liu, X. Li, L.-S. Chen, and J.-X. Tang, "Toward scalable flexible nanomanufacturing for photonic structures and devices," *Advanced Materials*, vol. 28, no. 47, pp. 10353–10380, 2016.

[364] T. Hellweg, "Towards large-scale photonic crystals with tuneable bandgaps," *Angewandte Chemie International Edition*, vol. 48, no. 37, pp. 6777–6778, 2009.

[365] Y. Yue and J. P. Gong, "Tunable one-dimensional photonic crystals from soft materials," *Journal of Photochemistry and Photobiology C: Photochemistry Reviews*, vol. 23, pp. 45–67, 2015.

[366] Z. Li, S. Li, and T. Ma, "Theoretic guide for using photonic glasses as colored covers for solar energy harvesting," *arXiv preprint arXiv:2209.05026*, 2022.

[367] N. J. Dawson, Y. Lu, Z. Lowther, J. Abell, N. D. Christianson, A. W. Weiser, and G. Aquino, "Low-cost automated spin coater and thermal annealer for additive prototyping of multilayer bragg reflectors," *arXiv preprint arXiv:2210.13220*, 2022.

[368] S. Hou and S. R. Forrest, "Artificial photosynthetic devices utilizing polariton antennas," Aug. 25 2022. US Patent App. 17/666,664.

[369] D. Sanvitto and S. Kéna-Cohen, "The road towards polaritonic devices," *Nature materials*, vol. 15, no. 10, pp. 1061–1073, 2016.

[370] M. Russo, K. Georgiou, A. Genco, S. De Liberato, G. Cerullo, D. G. Lidzey, A. Othonos, M. Maiuri, and T. Virgili, "Direct evidence of ultrafast energy delocalization in a strongly coupled organic microcavity probed by two-dimensional electronic spectroscopy," in *International Conference on Ultrafast Phenomena*, pp. M2A–7, Optica Publishing Group, 2022.

USC UNIVERSIDADE DE SANTIAGO DE COMPOSTELA

[371] F. Wu, D. Finkelstein-Shapiro, M. Wang, I. Rosenkampff, A. Yartsev, T. Pascher, T. C. Nguyen-Phan, R. Cogdell, K. Börjesson, and T. Pullerits, "Optical cavity-mediated exciton dynamics in photosynthetic light harvesting 2 complexes," *Nature Communications*, vol. 13, no. 1, pp. 1–7, 2022.

USC UNIVERSIDADE DE SANTIAGO DE COMPOSTELA

APPENDIX A

Supplementary

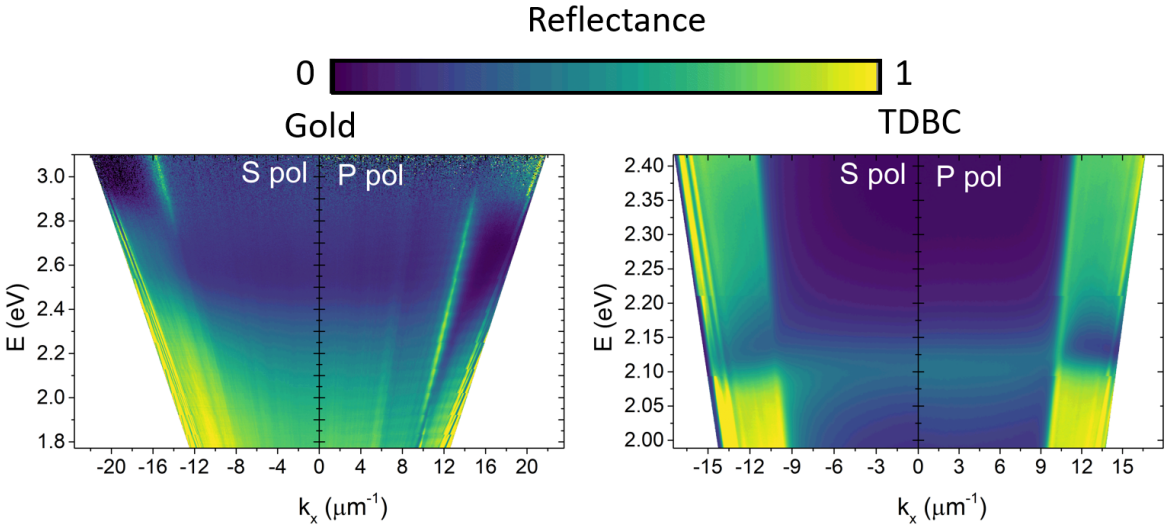


Figure A.1: **Polariton observed in reflectance**. Experimentally measured angle dependent reflectance of a thin film of gold (left) and TDBC-PVA (right) using the oil immersion lens technique described in section 2.3 under the different polarisations. The gold film is 25 nm thick. The organic solution used is a 3:1 mixture of 6.0% wt. of PVA (Aldrich PVA Mw = 85000–124000) with 2% wt. of TDBC. This solution was diluted with water at a 1:1 volume ratio. It was then spin-coated at 2000 RPM onto a thin coverslip. Expected 80 nm thickness.

USC
UNIVERSIDADE DE SANTIAGO DE COMPOSTELA

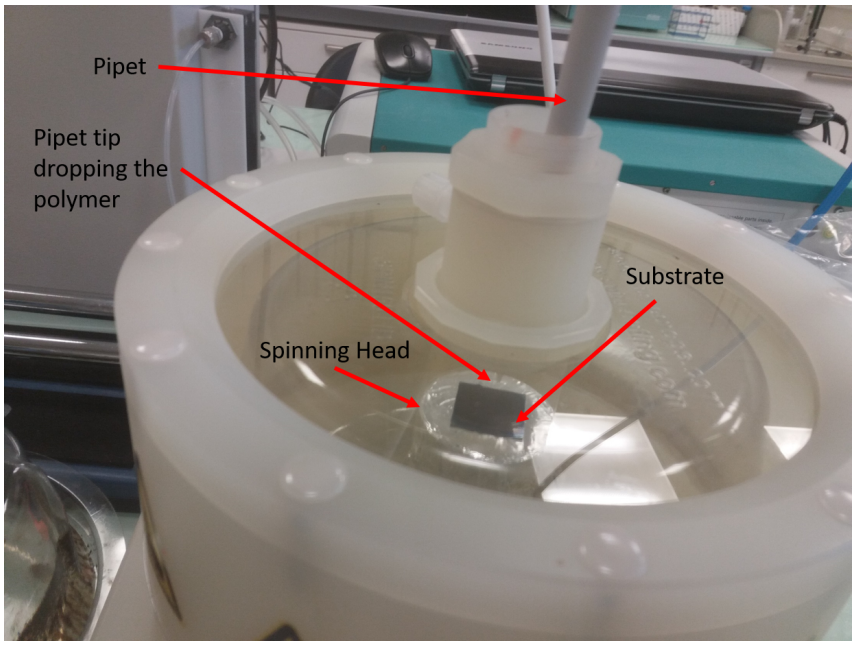


Figure A.2: **Fabrication set-up**. The spin coater used to fabricate all organic multilayered samples.

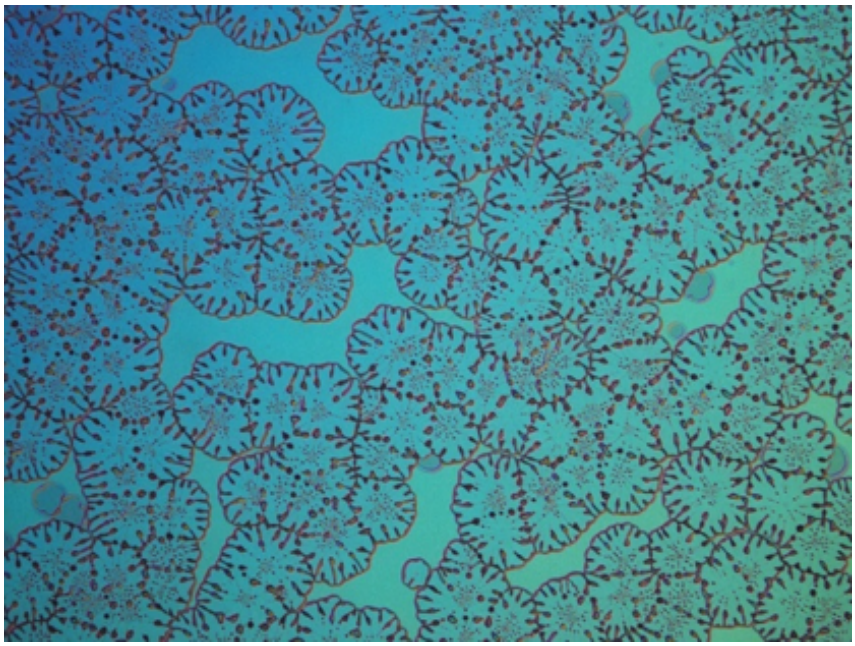


Figure A.3: **Sample damage**. Optical microscope view of a PVA monolayer after being left under the hot plate right after being spin-coated. The star-shaped figures are caused by the fast boiling of the solvent.

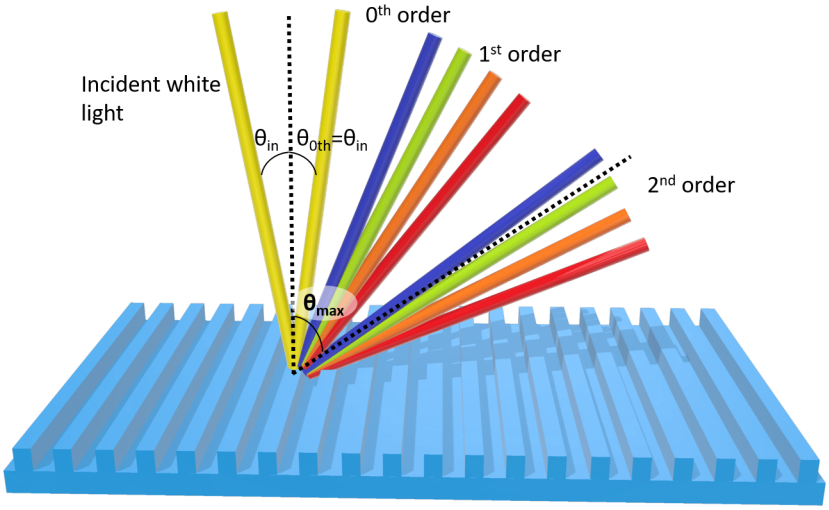


Figure A.4: **Optical grating**. Light incident on an optical grating gets diffracted into several orders. With the exception of the 0^{th} order, longer wavelengths become diffracted at higher angles. The detected light reflected from this structure will depend on the maximum angle of capture of the lens.

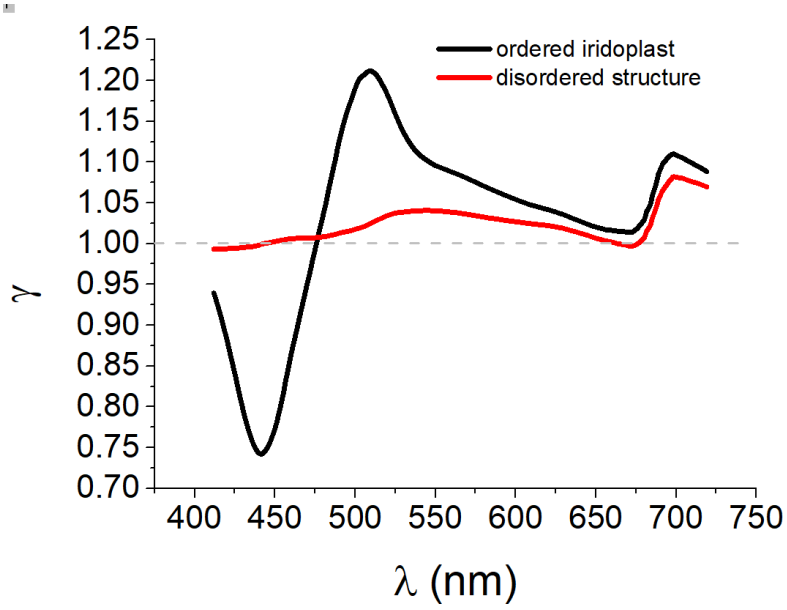


Figure A.5: **Random stroma spacing**. Absorption enhancement factor γ of chloroplasts with the same number of grana as iridoplasts but where each stroma spacing is given a random value between 1 and 200 nm. Averaged over 100 different structures.

USC DE SANTIAGO DE COMPOSTELA

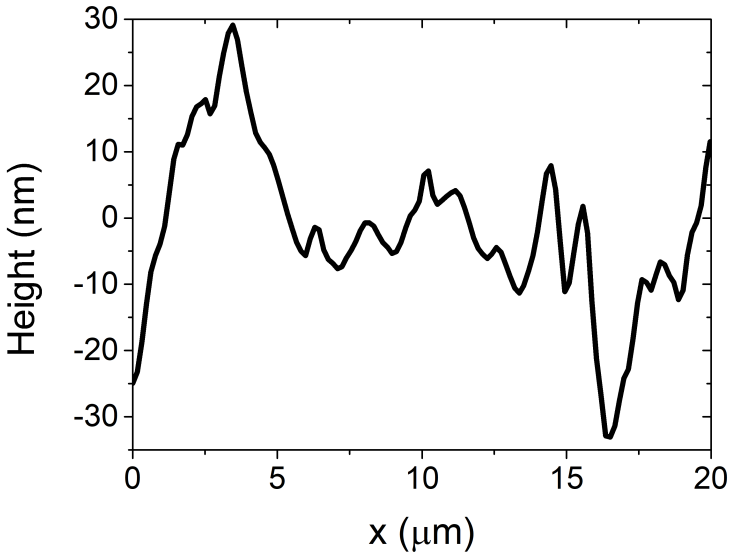


Figure A.6: **Topographical measurement between bleached and non-bleached regions**. They were done using an AFM. The fact that no step is observed in this measurement, shows that no change is observed in the topography between a bleached and a non-bleached region. The non-flat surface is a consequence of the low processability of TDBC.

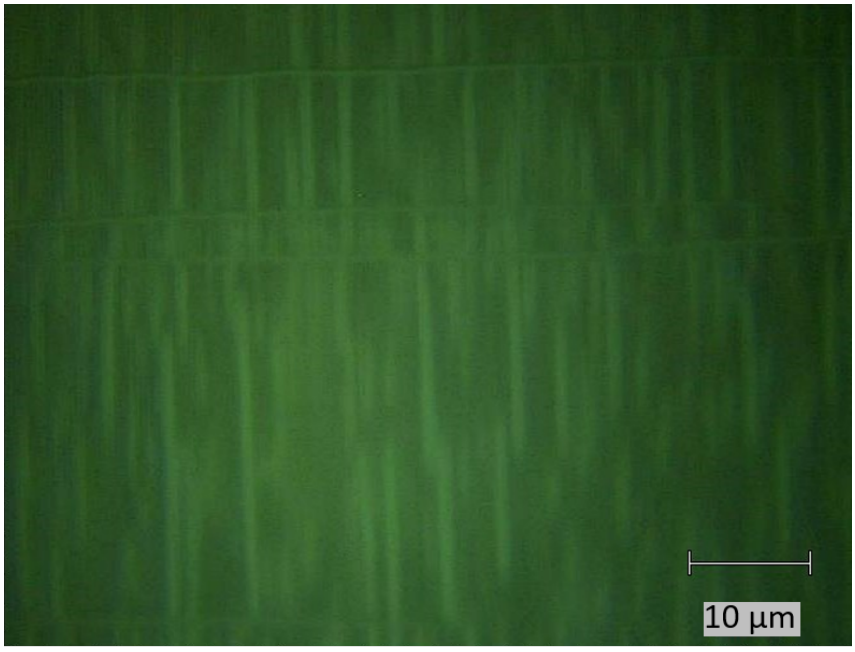


Figure A.7: **Low quality gratings**. Example of a PDMS grating sample under a strain of $\epsilon = 0.3$ where the wrinkles present considerable defects.

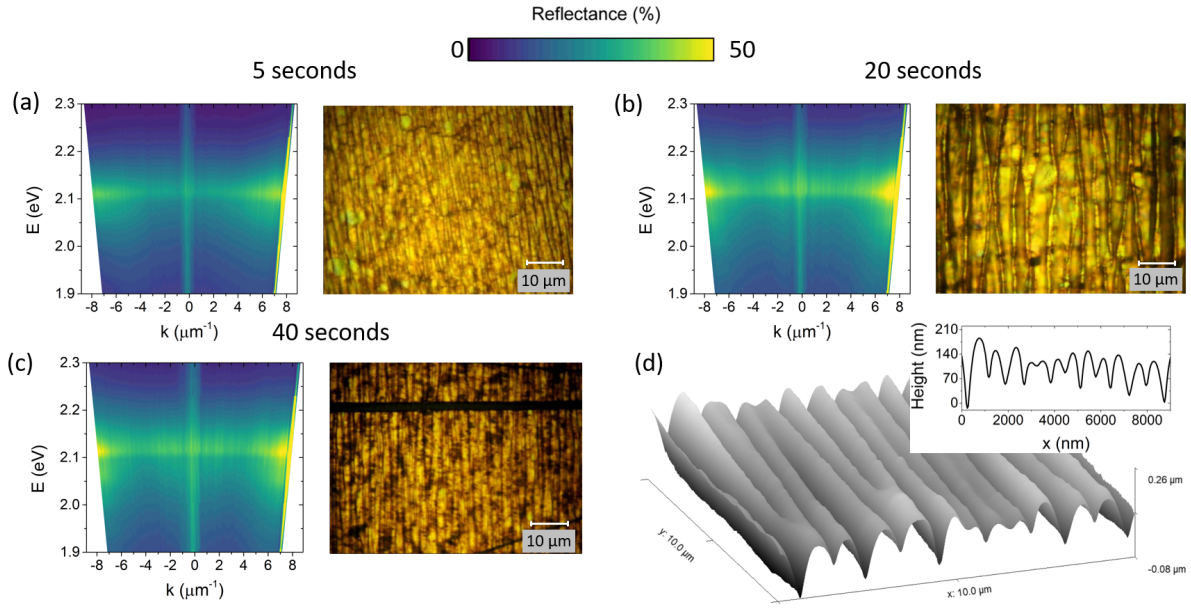


Figure A.8: **TDBC-PVA low quality gratings**. P polarised angle-dependent reflectance and optical microscope image of TDBC-PVA gratings under different oxygen plasma exposure times: (a) 5, (b) 20, and (c) 40 seconds. These are examples where the TDBC-PVA didn't wrinkle as desired. (d) AFM of a sample of TDBC-PVA on a 40 second oxygen plasma exposure. The inset is a cross-section of the measurement.

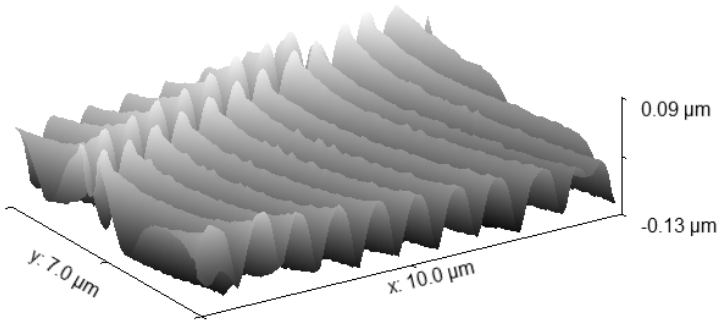


Figure A.9: **AFM of the sample in figure A.8 (d)**. This measurement was done in a part of the sample where TDBC-PVA did not spread. The topography is similar to a sample with no TDBC-PVA.

USC UNIVERSIDADE DE SANTIAGO DE COMPOSTELA

USC
UNIVERSIDADE
DE SANTIAGO
DE COMPOSTELA





Photonic crystals are nanostructured systems which manipulate and confine light at the nanoscale. However, significant hurdles in their fabrication remain, delaying the progress toward large-scale commercial applications. Interestingly, nature has been developing these structures for aeons in animals, insects and even plants. In this dissertation, we start by studying the natural photonic structure known as iridoplasts, a specialised iridescent photosynthetic system. We show that this biological organism could be using its photonic properties to mould the absorption of light. We fabricate soft matter photonic structures inspired by iridoplasts. The materials and fabrication methods used could help overcome some of the hurdles of the commonly used fabrication techniques for photonic crystals.